



HAL
open science

Influence of baryonic physics in simulations of disc galaxies

Anaëlle Hallé

► **To cite this version:**

Anaëlle Hallé. Influence of baryonic physics in simulations of disc galaxies. Cosmology and Extra-Galactic Astrophysics [astro-ph.CO]. Université Pierre et Marie Curie - Paris VI, 2013. English. NNT: . tel-00924468

HAL Id: tel-00924468

<https://theses.hal.science/tel-00924468>

Submitted on 6 Jan 2014

HAL is a multi-disciplinary open access archive for the deposit and dissemination of scientific research documents, whether they are published or not. The documents may come from teaching and research institutions in France or abroad, or from public or private research centers.

L'archive ouverte pluridisciplinaire **HAL**, est destinée au dépôt et à la diffusion de documents scientifiques de niveau recherche, publiés ou non, émanant des établissements d'enseignement et de recherche français ou étrangers, des laboratoires publics ou privés.

THÈSE DE DOCTORAT DE
L'UNIVERSITÉ PIERRE ET MARIE CURIE

Spécialité :
Astronomie et Astrophysique

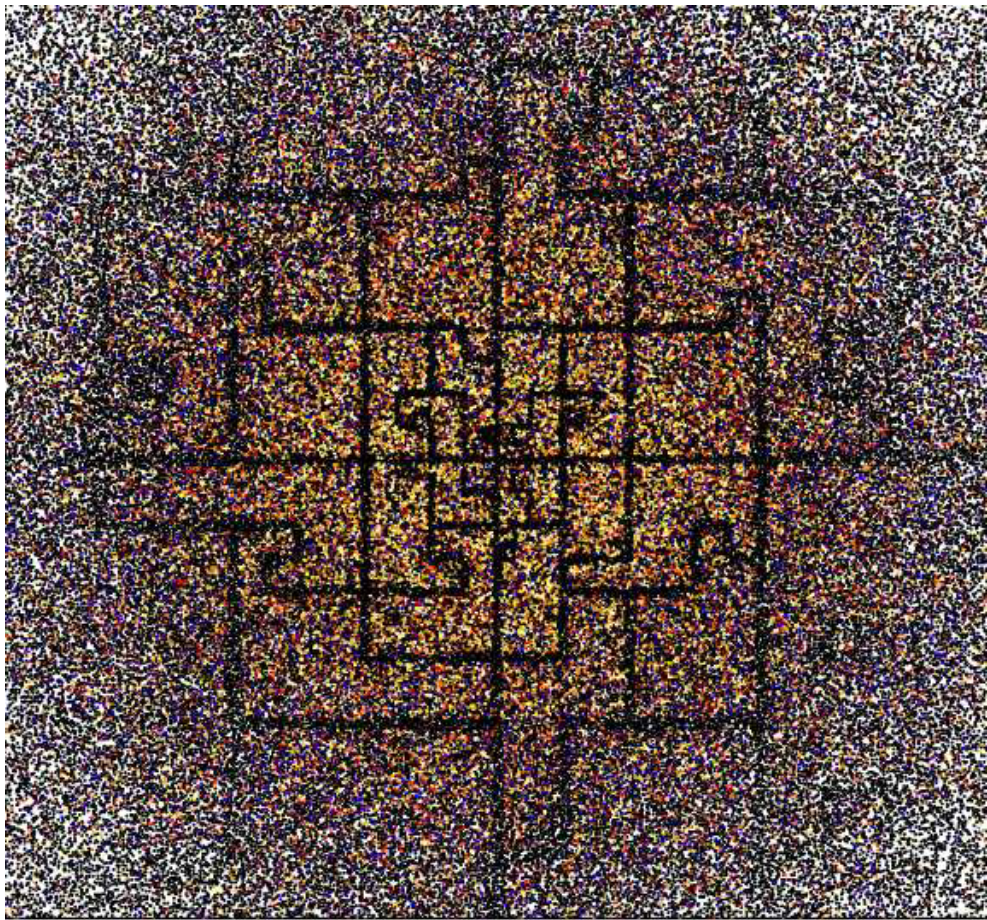
Présentée par
Anaëlle HALLÉ

pour obtenir le grade de
DOCTEUR DE L'UNIVERSITÉ PIERRE ET MARIE CURIE

**Influence de la physique baryonique
dans les simulations de galaxies
spirales**

Thèse soutenue le 23 mai 2013 devant le jury composé de

Benoît SÉMELIN	Président du jury
Ian BONNELL	Rapporteur
Romain TEYSSIER	Rapporteur
Frédéric BOURNAUD	Examineur
Paola DI MATTEO	Examinatrice
Daniel PFENNIGER	Examineur
Françoise COMBES	Directrice de thèse, membre invité



Abstract

The modelling of baryonic physics in numerical simulations of disc galaxies allows to study the evolution of the different components, the physical state of the gas and the star formation.

The present work aims at investigating in particular the role of the cold and dense molecular phase, which could play a role of gas reservoir in the outer galaxy discs, with low star formation efficiency.

After a presentation of galaxies with a focus on spiral galaxies, their interstellar medium and dynamical evolution, we review the current state of hydrodynamical numerical simulations and the implementation of baryonic physics. We then present the simulations we performed. These include cooling to low temperatures, and a molecular hydrogen component. We especially test the impact of the presence of molecular hydrogen in simulations with several feedback efficiencies, and find that the molecular hydrogen allows in all cases some slow stellar formation to occur in the outer disc, with an effect on the vertical structure of the disc that is sensitive to the feedback efficiency. Molecular hydrogen is therefore able to play the role of gas reservoir in external parts of spiral galaxies, which accrete gas from cosmic filaments all along their lives.

Résumé

Notre travail se concentre sur le rôle de la phase moléculaire froide et dense dans l'évolution des galaxies spirales. Cette phase peut jouer le rôle de réservoir de gaz à faible taux de formation stellaire dans les parties externes des disques.

Après une présentation générale des propriétés des galaxies, en particulier des galaxies spirales, leur milieu interstellaire et leur évolution dynamique, nous passons en revue les simulations numériques hydrodynamiques contemporaines et l'implémentation de la physique baryonique. Nous présentons ensuite la série de simulations que nous avons effectuées. Ces simulations incluent du refroidissement jusqu'à basse température, en prenant notamment en compte de l'hydrogène moléculaire. Nous testons en particulier l'influence de l'hydrogène moléculaire dans des simulations avec différentes efficacités de rétroactions énergétique stellaire, et obtenons que le dihydrogène permet dans tous les cas une faible formation d'étoiles dans les parties externes des disques. Les disques gazeux ont de plus tendance à s'épaissir à grands rayons du fait de la rétroaction stellaire renforcée par la présence de dihydrogène.

L'hydrogène moléculaire peut donc jouer le rôle de réservoir de matière baryonique dans les parties externes des galaxies spirales qui accrètent du gaz par les filaments cosmiques tout au long de leur vie.

Résumé détaillé

Les simulations numériques permettent de tester des hypothèses sur la physique non linéaire en jeu dans la formation et l'évolution des galaxies. Grâce au développement des possibilités de calcul numérique et l'élaboration d'algorithmes efficaces pour traiter la gravitation et l'hydrodynamique, il est possible de simuler de mieux en mieux l'évolution des galaxies. Les limitations en résolution spatiale et massique nécessitent cependant d'utiliser des méthodes dites "sous-grille" pour traiter les détails de la physique du gaz. Le caractère phénoménologique de ces méthodes est accentué par les incertitudes concernant notamment la physique de la formation des étoiles et l'impact de cette formation d'étoiles sur le gaz environnant.

Dans ce travail, nous nous intéressons particulièrement à l'impact de l'inclusion d'hydrogène moléculaire et du refroidissement du gaz subséquent sur l'évolution de galaxies spirales. Nous utilisons un code de type TreeSPH qui traite les composantes stellaires, gazeuses, et la matière noire comme des particules.

L'hydrogène moléculaire se forme surtout sur la poussière interstellaire dès lors qu'une faible quantité de grains de poussière est présente, et est dissocié par le rayonnement ultra-violet, notamment celui issu des jeunes étoiles massives. Il peut être protégé de ce rayonnement soit par l'effet de "bouclier" de la poussière qui absorbe le rayonnement, soit par sa propre protection, les molécules de dihydrogène de certaines régions pouvant absorber suffisamment de rayonnement pour que se maintienne de l'hydrogène moléculaire dans d'autres régions, comme à l'intérieur d'un nuage dense de gaz. La présence d'hydrogène moléculaire dépend donc de la quantité de poussière présente et de la possibilité du gaz de se protéger lui-même du rayonnement ultra-violet. Nous utilisons une recette semi-analytique pour déterminer la fraction d'hydrogène moléculaire en fonction des caractéristiques de la densité du gaz, de la métallicité et du flux ultra-violet ambiant. Ce flux est estimé par la sommation des contributions des étoiles jeunes formées au cours de la simulation.

Le gaz refroidi peut se condenser et former des étoiles, ce qui agit en retour sur le gaz, en particulier par les explosions de supernovae. Nous prenons en compte le refroidissement lié à l'hydrogène, l'hélium et certains métaux au-delà de 10 000 K par l'intermédiaire de taux de refroidissement tabulés en fonction de la température et de la métallicité. En-dessous de 10 000 K, nous prenons en compte le refroidissement lié à certains métaux contenus dans le milieu interstellaire car ils sont rejetés par les supernovae. Nous considérons aussi le re-

froidissement lié à l'hydrogène moléculaire, en incluant les contributions des collisions avec les atomes d'hydrogène, d'hélium, et les autres molécules de dihydrogène. La formation d'étoiles est modélisée par une méthode stochastique, et la rétroaction énergétique des supernovae de type II est appliquée sous forme cinétique dans la plupart des simulations.

Nous faisons varier l'important de la rétroaction énergétique des supernovae. Nous étudions tout d'abord des simulations de galaxies spirales sans prendre en compte d'hydrogène moléculaire. Nous imposons un gradient de métallicité dans le gaz afin de reproduire les observations de profils de métallicité. Le gaz est d'autant plus hétérogène, avec des pics de masses volumique, dans les parties centrales que la rétroaction est faible. En présence de rétroaction, la formation d'étoiles dans les régions denses limite la masse volumique maximale du gaz et régule donc aussi la formation d'étoiles. Les parties externes, pauvres en métaux, sont elles diffuses car peu refroidies, et forment très peu d'étoiles.

Nous observons que la prise en compte de l'hydrogène moléculaire permet d'obtenir, pour toutes les intensités de rétroaction stellaire, une faible formation d'étoiles dans les parties externes des disques, régions pauvres en métaux et donc peu susceptibles d'être assez refroidies pour former des étoiles en l'absence du refroidissement lié à l'hydrogène moléculaire. Ce résultat est cohérent avec de récentes observations de rayonnement ultra-violet dans les parties externes de certaines galaxies spirales. Nous relierons le taux de formation d'étoiles surfacique à la masse surfacique de tout le gaz ou de la partie d'hydrogène atomique ou moléculaire, et obtenons une meilleure corrélation avec le gaz moléculaire seul, comme observé dans des études de galaxies proches. La corrélation est meilleure en présence de rétroaction stellaire car le gaz est alors moins hétérogène en masse volumique.

La formation stellaire accentuée par l'hydrogène moléculaire dans les parties externes influe sur la structure verticale du disque. La rétroaction des supernovae provoque l'épaississement du disque à grands rayons, d'autant plus que la rétroaction est importante.

Les résultats obtenus peuvent être sensibles aux méthodes utilisées pour la modélisation de la physique baryonique. Nous présentons quelques variations dans la modélisation de la formation d'étoiles et la rétroaction stellaire. L'état physique du gaz est affecté par des changements tels que l'augmentation du seuil de masse volumique à partir duquel le gaz peut former des étoiles.

Les résultats des simulations suggèrent que la présence d'hydrogène moléculaire peut jouer un rôle dans le cycle baryonique en accumulant du gaz accrété dans les parties externes des disques.

Thanks

I would like to thank Françoise Combes for having allowed me to work on this subject and for her great availability, Benjamin L’Huillier for having helped in many computing details and for a nice office sharing for two years, Philippe Salomé for many conversations and a lot of advice, Yves Revaz for his precious help on Gadget, Maxime Bois, Martin Stringer and Benoît Sémelin for helpful conversations about my work, Alain Coulais for saving my Ubuntu after a de-installation of Python, Antoine Radiguet, Maëva Milan, Jonathan Freundlich and Charlène Lefèvre that were friendly office-mates during these years. Thank you to many other LERMA people such as Michel Caillat or Jeanne Treuttel for pleasant lunches, and to the nice LERMA administrative staff for their efficiency.

Thank you to my friends, especially Alice Fagard, Audrey Proust, Matthew Lee, Irène Balmès, Rémi Proville and Adeline Pons, and to my family for having supported me.

The first chapters of this thesis were partly inspired from the reading of a few text books: [Binney & Tremaine \(2008\)](#); [Mo et al. \(2010\)](#); [Draine \(2011\)](#).

Contents

1	Galaxies: an overview	1
1	Diversity and scaling laws followed by galaxies	1
1.1	Galaxy classifications	1
1.2	Some properties of elliptical galaxies	3
1.3	Some properties of spiral galaxies	4
2	Galaxies in a cosmological context	8
2.1	Λ CDM model and the baryonic budget	8
2.2	Organisation of galaxies at various scales	10
3	Some statistical properties	11
3.1	Bimodality	11
3.2	Dependence on environment	11
2	Spiral galaxies	13
1	The ISM of spiral galaxies: content, physics and star formation	13
1.1	Composition and phases	13
1.2	Molecular hydrogen	15
1.3	Cooling and heating in the ISM	19
1.4	Star formation in spiral galaxies	20
2	Instabilities, bars and spiral structure	23
2.1	Observations	23
2.2	Local instability	24
2.3	Nature of bars and spiral structure	26
2.4	Secular evolution	26
3	Simulations of galaxies	29
1	Different types of simulations	29
1.1	Cosmological simulations	29

1.2	Galactic scale simulations	30
2	Simulating stars and dark matter dynamics	31
2.1	The Vlasov-Poisson system	31
2.2	Algorithms for collisionless dynamics	32
2.3	Time integration	37
3	Simulating gas dynamics	38
3.1	Sticky particle algorithm	38
3.2	Hydrodynamics algorithms	38
4	Implementing astrophysical processes	46
4.1	Star formation	46
4.2	Stellar feedback	47
4.3	Cooling and heating of the ISM	49
4.4	Molecular hydrogen formation and destruction	49
4.5	Importance of resolution	50
4	Introducing baryonic physics in Gadget-2	53
1	Some specific features of Gadget-2	53
1.1	Parallelisation	53
1.2	Individual time-steps	54
2	Code steps and implemented additions and changes	55
2.1	Initialisation	55
2.2	Main loop	55
3	Radiative cooling	60
3.1	Line cooling	60
3.2	Cooling by metals under 10^4 K	62
3.3	Cooling of H, He and metals above 10^4 K	63
3.4	Cooling by molecular hydrogen	64
3.5	Cooling by HD	66
3.6	Total cooling	70
3.7	Algorithm for cooling	70
4	H ₂ fraction	72
5	Star formation	74
6	Supernova feedback	75
5	Simulations	77

1	Initial Conditions	77
1.1	Density profiles	77
1.2	Velocities	78
1.3	Resolution	79
1.4	Relaxation of initial conditions	80
2	Feedback efficiency variation in metal-cooling only simulations	81
2.1	Gas and stars discs	81
2.2	Thermal state of the gas	84
3	Simulations including H ₂	87
3.1	H ₂ fraction	87
3.2	Gas physical state	87
4	Results on star formation	91
4.1	Gas mass depletion and total SFR	91
4.2	SFR as a function of radius	92
4.3	Stellar discs	93
4.4	Kennicutt-Schmidt diagrams	94
4.5	Gas density profile variation	99
5	Vertical structure of the disc	99
6	Variations of parameters or baryonic physics methods	102
6.1	Resolution	102
6.2	Threshold density for star formation	103
6.3	Recipe for feedback	105
6	Conclusion and perspectives	109
A	Influence of baryonic physics in galaxy models: a semi-analytic treatment of the molecular component	111
B	Graph of the functions of the code	113

List of Figures

1.1	Hubble Sequence	2
1.2	Colour and neutral hydrogen mass fraction for galaxies of different types	3
1.3	Surface densities and rotation curves	6
1.4	Baryonic Tully-Fisher Law	7
1.5	Matter-energy content and baryonic content of the Universe	10
1.6	Spatial distribution of galaxies in the 2dFGRS survey	11
1.7	Colour-magnitude diagram of galaxies in the SDSS survey	12
2.1	GMC complex in the Perseus arm	16
2.2	Energy levels of H_2	17
2.3	Cooling functions.	20
2.4	Compilation of observations of surface SFR vs $HI+H_2$ surface density	22
2.5	Surface SFR vs $HI+H_2$, HI and H_2 gas surface density	22
2.6	M51 observed in different wavelengths	24
2.7	Schematic zones of stability or instability for perturbations in a disc	25
3.1	Gas density maps of simulations at different scales	30
3.2	Quad-tree (in 2 dimensions)	36
3.3	Cubic spline softening kernel and potential of a point mass for different potentials	37
3.4	Eulerian vs Lagrangian discretisations	39
3.5	Schematic view of an SPH kernel volume	41
3.6	Simulations of a dense gas cloud in a supersonic flow	45
4.1	Peano-Hilbert curve	54
4.2	Schematic view of individual time-steps	55
4.3	Schematic rearrangement of particles in memory	58
4.4	Two-level system	62
4.5	Individual cooling curves of metals	63

4.6	Cooling curves of metals for different densities	64
4.7	Cooling curves of Sutherland & Dopita (1993)	65
4.8	Full cooling curves for metals	65
4.9	Low densities collisional cooling rates of H ₂	67
4.10	Cooling rate of H ₂ for different H ₂ mass fractions	67
4.11	Cooling rate of H ₂ for different hydrogen nuclei densities	68
4.12	LTE cooling rates of H ₂ and HD per molecule	68
4.13	Comparison of cooling rates of H ₂ and HD	69
4.14	Total cooling rates for T < 10 ⁴ K for different metallicities and H ₂ mass fractions	71
5.1	Initial rotation curve	79
5.2	Initial surface densities	80
5.3	Initial gas density map	81
5.4	Gas density maps for $\alpha_{\text{fb}} = 0\%$ and $\alpha_{\text{fb}} = 1\%$	82
5.5	Gas density maps for $\alpha_{\text{fb}} = 10\%$ and $\alpha_{\text{fb}} = 40\%$	83
5.6	Time Fourier analysis	85
5.7	Temperature-density histograms	86
5.8	Temperature-density histograms with H ₂	86
5.9	Global H ₂ mass fraction	88
5.10	Surface densities of gas components	88
5.11	Gas density maps with H ₂	89
5.12	Temperature-density histograms with H ₂	90
5.13	Evolution of the fraction of cold gas	91
5.14	Hydrogen nuclei number density-galactocentric radius histograms	92
5.15	Global star formation	93
5.16	Star formation as a function of radius	94
5.17	Surface densities of new stars	95
5.18	Surface densities of all stars	96
5.19	K-S diagrams for $\alpha_{\text{fb}} = 0\%$	97
5.20	K-S diagrams for $\alpha_{\text{fb}} = 10\%$	98
5.21	Surface densities of gas components	99
5.22	Vertical structure of the gas	100
5.23	Fraction of gas beyond 1 kpc from the disc plane	101
5.24	Vertical mass profile at large radii	101
5.25	Global star formation for different resolutions	103

5.26	Global H ₂ mass fractions for different resolutions	104
5.27	Hydrogen nuclei number density PDFs for different resolutions	104
5.28	Gas density maps for a high density threshold for star formation	105
5.29	Hydrogen nuclei number density-galactocentric radius histograms	106
5.30	Global star formation	106
5.31	Gas density maps for different feedback methods	107
5.32	Global star formation for different feedback methods	107
5.33	Temperature-density histogram for different feedback methods	108
B.1	Part 1 of functions graph	114
B.2	Part 2 of functions graph	115

Chapter 1

Galaxies: an overview

Galaxies can be loosely defined as gravitationally bound objects containing many stars, from a lower bound at $\sim 10^5$ stars for the smaller galaxies, below the $\sim 10^6$ stars in the largest stellar clusters (substructures of galaxies), to an upper bound of $\sim 10^{12}$ stars (Binney & Tremaine 2008). They were proved to be extragalactic objects only in the 1920s, when Edwin Hubble calculated distances of a few close galaxies using the properties of Cepheid stars (Hubble 1926). Observations of increasing resolution and in a vast range of wavelengths have then allowed to derive properties of our own galaxy, the Milky Way, and to explore the diversity of sizes, shapes and physical properties of galaxies in the local universe and also at larger distances, meaning, due to the finite speed of light, at earlier times of the Universe.

1 Diversity and scaling laws followed by galaxies

1.1 Galaxy classifications

Hubble proposed a classification of galaxies, originally expressing what he thought was a time evolution, from the left of Figure 1.1 to one of the ends of the branches on the right. This classification distinguishes galaxies according to their morphology.

The galaxies at the left of the sequence are elliptical galaxies, exhibiting smooth ellipsoidal isophotes (contours of same surface brightness). They are sorted as E n 's, with n growing as the isophotes are more elongated. n is the closest integer to $10(1 - \frac{b}{a})$, with a the semimajor axis and b the semiminor axis of the isophotes. A spherical galaxy is thus an E0, and the classification goes up to the most elongated ellipticals observed, E7's.

On the right side of the sequence reside spiral galaxies, barred (e.g. SBa) or not (e.g. Sa). Spiral galaxies have most of their stars in a thin disk, with a characteristic height much smaller than their characteristic radial length, supported against gravitational collapse by the rotation of the stars around the center. They often present a stellar central spheroidal "bulge" component. In the Hubble sequence, spiral galaxies are separated into a, b and c types according to the relative size of the bulge compared to the disc, and how tightly wound

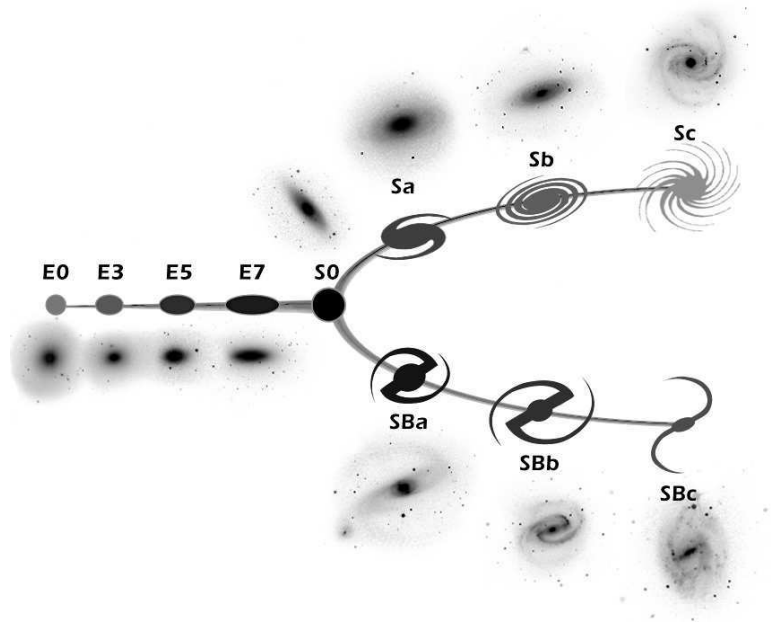


Figure 1.1: Hubble Sequence. From an image created by NASA and ESA.

the spiral arms are. Sa galaxies have a large bulge to disc ratio and tightly wound spiral arms, while types b and c have progressively smaller bulge to disk ratios and more loosely wound arms. About half of observed disc galaxies have a central bar component.

Lenticular galaxies, S0s, are intermediate galaxies insofar as they have a stellar disc with possible spiral arms and bars, but contain very little gas and have a more dominant bulge than disc galaxies. They are mainly found in clusters of galaxies.

Dwarf galaxies or galaxies of ellipsoidal or irregular shapes that have a faint luminosity, are not included in this classification in its original version. A population of dwarf galaxies resemble ellipticals except that they have lower masses. Amongst the elliptical shaped dwarves, the lighter ones with an almost spherical shape have been called dwarf spheroidals.

Finally, some galaxies are called “peculiar” galaxies because of their unique shape that makes it impossible to attribute them a Hubble type. The Antennae (NGC 4038 and 4039) are such galaxies. Peculiar galaxies are thought to often be the result of mergers between galaxies. The tidal forces explain long tails that can be observed in some of these galaxies.

Other morphological classifications have been proposed. [de Vaucouleurs \(1974\)](#) inserted sub-categories in the spiral branches of the Hubble sequence, such as Sbc, and extended the classification to Sd types and irregular galaxies, lacking any clear symmetry, but that can be added on the right of the sequence as an extension to normal spirals or barred spirals if they contain a bar-like component. The de Vaucouleurs classification attributes a number accounting for the bulge to disk ratio, from -6 for ellipticals, to 10 for irregular galaxies.

It is also possible to classify galaxies in terms of other properties. Photometric properties, such as luminosity, surface brightness or colour can be used. The gas fraction or the star

formation rate can also serve as a basis for classifications. While it is no longer thought that galaxies evolve from the beginning of the Hubble sequence to one of its end during their life time, the sequence (or the de Vaucouleurs classification) is still useful to separate morphological classes, and because physical properties such as the colour or neutral hydrogen fraction vary systematically along it as shown on Figure 1.2.

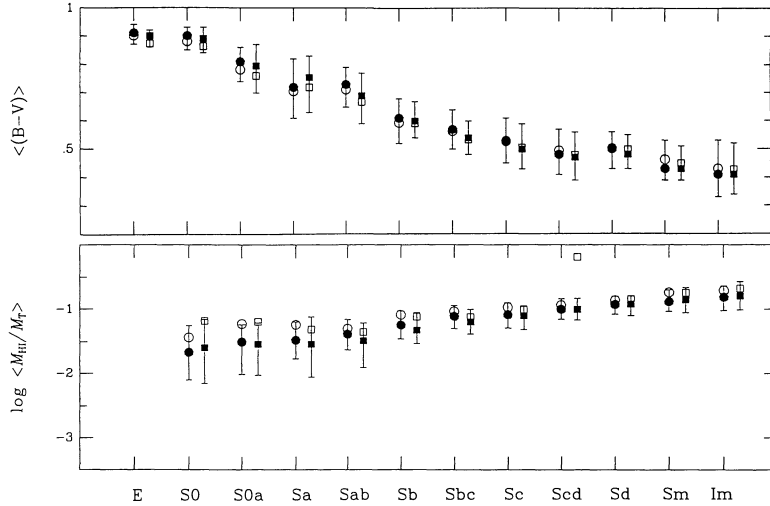


Figure 1.2: Colour and neutral hydrogen mass fraction for galaxies of different types, from Roberts & Haynes (1994).

1.2 Some properties of elliptical galaxies

1.2.1 Baryonic content

Elliptical galaxies have stellar masses from $\sim 10^6 M_{\odot}$ for dwarf ellipticals, to $\sim 10^{12} M_{\odot}$ for the most massive ellipticals in the centre of galaxy clusters. Their photometric colour is red, indicating old stellar populations. They contain little cold gas, although some small gas discs are present in some elliptical galaxies. Diffuse hot (10^7 K) gas is observed in X-ray: it forms coronae around ellipticals (e.g. Fabbiano 1989).

1.2.2 Stellar density profiles

One of the best fits to the one dimensional surface-brightness profiles $I(R)$, the surface brightness as a function of the semimajor axis R of the isophotes of ellipticals, is the Sérsic profile (Sersic 1968):

$$I(R) = I(0) \exp \left[-\beta_n \left(\frac{R}{R_e} \right)^{1/n} \right] \quad (1.1)$$

where $I(0)$ is the central surface brightness, R_e is the effective radius, i.e. the radius enclosing half of the total luminosity, β_n is a coefficient that must be determined numerically from R_e

and n is the Sérsic index. The steepness of surface brightness profiles inside R_e increases with n . $n = 4$ and $\beta_n = 7.67$ give the original density profile of giant ellipticals observed by [de Vaucouleurs \(1948\)](#) (the “ $R^{\frac{1}{4}}$ law”). The Sérsic index of the more general Sérsic profile is found to decrease from $n \simeq 10$ for the most luminous ellipticals to $n \simeq 0.5$ for faint dwarf ellipticals.

1.2.3 Shapes and kinematic properties

Stars in elliptical galaxies are mainly supported against collapse by their random motion, with variations following their shape that may deviate slightly from ellipsoids: “boxy” ones, i.e. galaxies whose isophotes resemble a parallelepipedal box, are almost uniquely supported by random motions while “discy” galaxies, i.e. galaxies that are a little flat, are also partly supported by rotation, which flattens them (e.g. [Kormendy & Bender 1996](#)). Ellipticals have also been divided into “slow rotators” and “fast rotators” by [Emsellem et al. \(2007\)](#) who studied the variations in the stellar specific angular momentum in central regions of a sample of local elliptical galaxies.

1.2.4 The fundamental plane

The kinematic of ellipticals is correlated with their photometric properties. The higher the central velocity dispersion is, the brighter and larger an elliptical is. [Faber & Jackson \(1976\)](#) derived the Faber-Jackson law relating the central velocity dispersion σ_0 to the luminosity L :

$$L \propto \sigma_0^\beta, \text{ with } \beta \sim 4 \quad (1.2)$$

while another relation, the D_n - σ relation relates central velocity dispersion to size. In fact, the logarithms of the effective radius, of the mean surface brightness inside the effective radius and of the central velocity dispersion can be used as coordinates variables of a fundamental plane on which ellipticals fall with a smaller scatter.

1.3 Some properties of spiral galaxies

1.3.1 Baryonic content

Spiral galaxies have lower stellar masses than ellipticals, going up to a few $\sim 10^{11} M_\odot$. They have a cold gas fraction (the ratio of the mass of cold gas to the mass of cold gas and stars) that goes from a few percent for Sa galaxies to $\sim 80\%$ for low mass/low surface brightness galaxies ([McGaugh & de Blok 1997](#)). The interstellar medium and the bar and spiral structures will be discussed in Chapter 2.

1.3.2 Stellar density profiles

The surface stellar density profiles of spiral galaxies can usually be fitted by a decomposition into a central spheroidal component with a Sérsic profile and an exponential disc:

$$I(R) = I(0) \exp\left(-\left(\frac{R}{R_d}\right)\right) \quad (1.3)$$

where $I(0)$ is the central surface brightness, and R_d is the characteristic radius that can go from 1 kpc to 50 kpc for giant low surface brightness galaxies (e.g. [de Jong 1996](#)).

Vertical profiles can be fitted by laws that decrease exponentially with the distance from the disc plane far away from the plane, and with central variations. In most discs seen edge-on, two components with about the same radial scale lengths but different scale heights can be distinguished: a thin disc of young stars with a scale height of a few hundreds of parsecs and a thick disc of older stars with a scale height $\simeq 1$ kpc.

1.3.3 Rotation curves

Rotation curves represent the circular velocity, the speed of a body in a circular orbit, as a function of galactocentric radius. Circular velocities are usually obtained from spectroscopy of HII regions emission lines (coming from ionised regions around young hot stars) or spectroscopy of the 21 cm emission line of HI, assuming that young stars and cold gas have almost circular orbits. The cold neutral HI gas extends much beyond the star forming disc, allowing the measurement of the circular velocities far away from the centre of galaxies, two or more times the radius of the stellar disc.

The rotation curves usually have the following features:

- Near the centre, circular velocity rises linearly with radius, as for a solid rotation (for which the angular speed $\Omega(R)$ is constant and the circular velocity $R\Omega(R)$ thus increases linearly with radius).
- The circular velocity reaches a plateau instead of decreasing at large radii. The maximal rotation speeds ranges from $\gtrsim 50$ km/s to $\simeq 300$ km/s.

The latter point, revealed in the 1970s by observations of ionised gas ([Rubin et al. 1978, 1980](#)) and the 21 cm hydrogen line ([Bosma 1978](#)), poses a problem if only observed mass is taken into account and if the gravitational law is trusted at the galactic scale. Indeed, if most of the mass is in stars, outside of the stellar disc, the curve should fall as $\sqrt{\frac{GM}{R}}$, where M is the stellar mass. Figure 1.3 shows the surface density profiles of stars and gas in two example galaxies with high or low surface brightnesses, and the two rotation curves deduced from 21 cm observations, with the contribution due to the baryonic components (the stellar bulge and disc having been decomposed) obtained from a numerical resolution of the Poisson equation from the surface densities. The total circular velocity inferred from the observed baryonic mass is significantly below the observed circular speed curve, at large radii or almost all radii for respectively the high and low surface brightness galaxies. The observed discrepancy is

usually attributed to the presence of an invisible component that does not radiate but is subject to gravitation and called dark matter. Observations of many flat rotation curves have brought an increasing body of proof for dark matter in spiral galaxies.

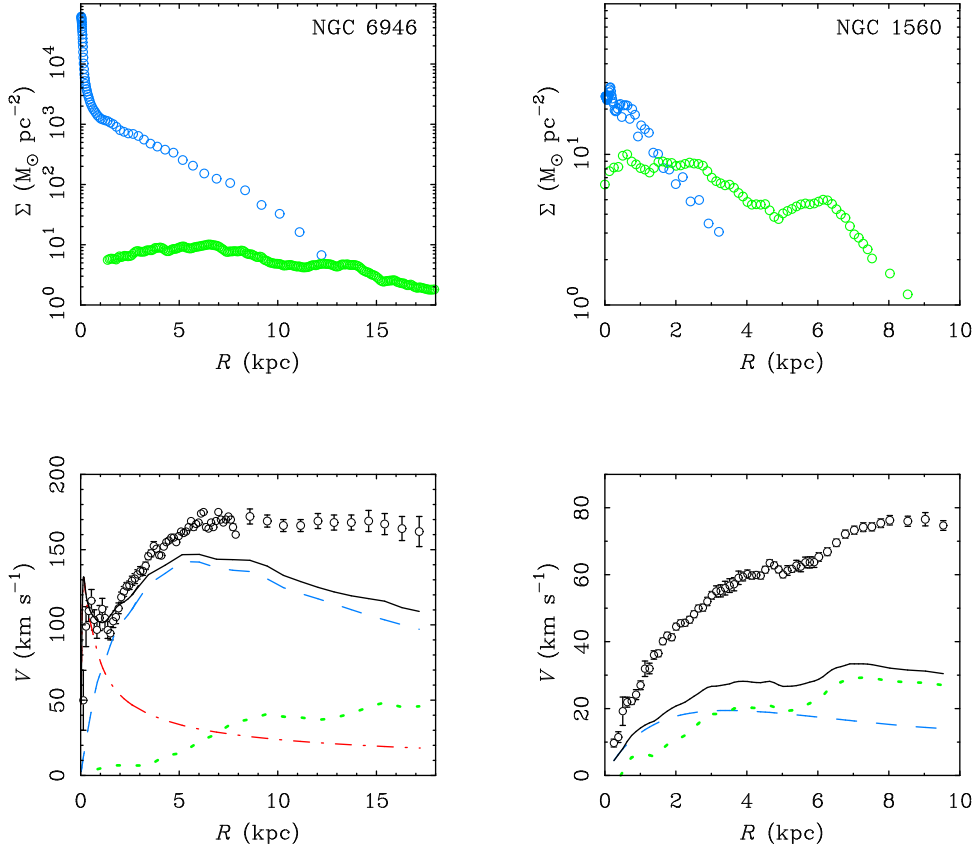


Figure 1.3: Top row: surface density profile of stars (blue circles) and neutral hydrogen (green circles). Bottom row: Rotation curves with the contributions inferred from the observed components: gas (dotted line), stellar bulge (dash-dotted line), stellar disc (dashed line), and the total contribution from observed baryonic matter (black solid line). Figure from [Famaey & McGaugh \(2012\)](#).

However, some alternatives to dark matter have been suggested. One of them is Modified Newtonian Dynamics (MOND), introduced by Milgrom in 1983 ([Milgrom 1983c,a,b](#)). According to his modified Newton’s law (or modified gravitational field, depending on the version), the acceleration/gravitational field felt by a body differs from the Newtonian one in the “low acceleration regime”, ie around and below an acceleration scale $a_0 \simeq 10^{-10} \text{ m/s}^2$, that is of the order of the centripetal accelerations felt by stars in galaxies. The gravitational field for low accelerations becomes $\sqrt{g_N a_0}$, where g_N is the Newtonian gravitational field and thus does not fall as $\frac{1}{r^2}$, but as $\frac{1}{r}$, making the circular speed constant with radius for large radii. MOND can fit rotation curves in details and is successful as a rule at the galactic scale, but it encounters some problems at clusters scale and building a satisfying corresponding

covariant theory analogous to General Relativity is still a problem.

1.3.4 The Tully-Fisher law

The luminosity of disc galaxies is observed to be correlated with their maximal circular speed V_{\max} . Tully & Fisher (1977) found the following relation between optical luminosity and the maximal rotation speed inferred from the width of the neutral hydrogen 21 cm emission line:

$$L \propto V_{\max}^N \quad (1.4)$$

The exponent N and the scatter depend on the colour band in which the observation is made. The exponent increases for longer wavelengths, from $\simeq 3$ in the B band to $\simeq 4$ in the redder K band and the scatter diminishes with wavelength. This relation is analogous to the Faber-Jackson relation for elliptical galaxies.

The Tully-Fisher relation may rather be a relation between baryonic mass and circular speed. As stellar populations radiate differently depending on the colour band, the mass to light ratio depends on the band and when adding the observed mass of gas to the stellar mass inferred from luminosity in near infrared bands (tracking the bulk of the stellar mass), it is actually possible to obtain a baryonic mass M_b vs circular speed tighter relation, the Baryonic Tully-Fisher Relation (McGaugh et al. 2000):

$$M_b \propto V_{\max}^4 \quad (1.5)$$

This law applies over a range of five decades in baryonic mass with a limited scatter as shown on Figure 1.4.

2 Galaxies in a cosmological context

2.1 Λ CDM model and the baryonic budget

2.1.1 Cosmology and the Λ CDM model

Most cosmological models rely on General Relativity (Einstein 1916), and the cosmological principle that states that, on large scales, the universe is homogeneous and isotropic. The Einstein equations link the geometry of spacetime to the matter-energy content, the geometry being encapsulated in a generic metric. When using the Friedmann-Lemaître-Robertson-Walker, a metric that is a solution of the Einstein equations that satisfies isotropy and homogeneity and involves a scale factor $a(t)$, and when describing the matter-content as an isotropic and homogeneous fluid of density ρ and pressure P , one gets equations that can be

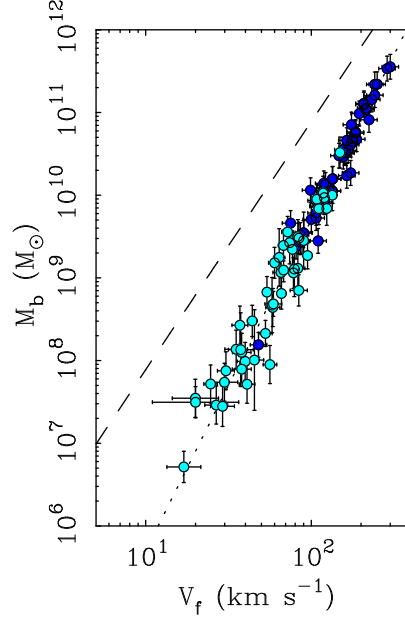


Figure 1.4: Baryonic Tully-Fisher Law (V_f is the outer disc velocity.). Data points are galaxies whose baryonic mass is dominated by gas (light blue points) or stars (dark blue points). Figure from [Famaey & McGaugh \(2012\)](#) using values from [McGaugh \(2005, 2011\)](#).

arranged the following way:

$$\left(\frac{\dot{a}}{a}\right)^2 = \frac{8\pi G}{3}\rho - \frac{kc^2}{a^2} + \frac{\Lambda c^2}{3} \quad (1.6)$$

$$\frac{\ddot{a}}{a} = -\frac{4\pi G}{3}\left(\rho + \frac{3P}{c^2}\right) + \frac{\Lambda c^2}{3} \quad (1.7)$$

where k is the curvature signature and Λ is named the cosmological constant. $H(t) = \frac{\dot{a}}{a}$, the rate at which the Universe expands, is named the Hubble constant as [Hubble \(1929\)](#) made the first observations of the expansion of the Universe studying the recession of distant galaxies and derived a first estimate of the current value H_0 of the constant.

A separation of the density ρ into the matter density $\rho_m \propto a^{-3}$ and the radiation density $\rho_r \propto a^{-4}$ gives for the first equation:

$$H^2(t) = H_0^2 \left[\Omega_{r,0} \left(\frac{a}{a_0}\right)^4 + \Omega_{m,0} \left(\frac{a}{a_0}\right)^3 + \Omega_{k,0} \left(\frac{a}{a_0}\right)^2 + \Omega_{\Lambda,0} \right] \quad (1.8)$$

where $\Omega_{r,0} = \frac{\rho_{r,0}}{\rho_{c,0}}$, $\Omega_{m,0} = \frac{\rho_{m,0}}{\rho_{c,0}}$, $\rho_{c,0} = \frac{3H_0^2}{8\pi G}$, $\Omega_{k,0} = -\frac{kc^2}{H_0^2}$, and $\Omega_{\Lambda,0} = \frac{\Lambda c^2}{3H_0^2}$. $\Omega_{r,0}$ is negligible compared to $\Omega_{m,0}$ and $\Omega_{\Lambda,0}$.

The currently preferred model, that fits very well with a number of observations and whose parameters are especially well constrained by the analysis of the Cosmic Microwave Background (CMB) by the WMAP mission (e.g. [Komatsu et al. 2011](#)) and the recent Planck

mission (Planck Collaboration et al. 2013), is the Λ CDM model, in which the universe has a flat geometry ($k = 0$), and is currently composed of:

- about two thirds of “dark energy”: $\Omega_{\Lambda,0} = 0.683$
- about one quarter of “Cold Dark Matter” (CDM): $\Omega_{\text{CDM},0} = 0.268$
- only a few percent of ordinary matter named in this framework “baryonic matter” (though including electrons): $\Omega_{b,0} = 0.049$

The values come from the 2013 results of the Planck mission. The matter contribution $\Omega_{m,0}$ to the content of the Universe is thus divided into $\Omega_{m,0} = \Omega_{\text{CDM},0} + \Omega_{b,0}$.

Dark energy, encapsulated in this model in the cosmological constant Λ in the equations of evolution of the geometry of the Universe, has been inferred from observations of distant supernovae of type Ia, that showed the expansion of the Universe is accelerating (Riess et al. 1998; Perlmutter et al. 1998). It acts as a fluid of negative pressure, thus allowing for expansion, and the value of the cosmological constant is sufficient for the expansion to be accelerating. Its nature remains a mystery.

Cold dark matter is postulated as a non-baryonic collisionless medium with no electromagnetic interaction but a gravitational role. It is needed at galactic and galaxy clusters scales to explain the often observed flatness of rotation curves incompatible to a Newtonian gravitation for the observed mass (as seen in 1.3.3), and to explain the mass of galaxies or clusters inferred from lensing and that are also incompatible with the observed matter and General Relativity. It is also assumed to allow the formation of structures to be quick enough so that the density fluctuations inferred from the temperature fluctuations of the CMB can give rise to current galaxies in a time of 13.7 Gyr, the estimated age of the Universe in this cosmological model. CDM is thought to collapse first, while in the hot baryon-photon plasma, the baryons are prevented from collapsing by the pressure of photons. As the Universe expands and the temperature of the plasma goes down, protons recombine with electrons, photons are now no longer scattered by free electrons and can propagate freely (giving rise to the CMB), and the baryonic matter can now collapse in the already formed dark matter wells. A number of detection experiments, assuming some energy range for dark matter particles, have been performed but they have still not given any clear detection.

While this model involves two components whose nature is not determined, it is an effective framework to reproduce observations.

2.1.2 Missing baryons

The fraction of 4.6% for the baryons is deduced from the CMB power spectrum analysis, is also predicted by primordial nucleosynthesis, and is consistent with Lyman α observations at a redshift $z \simeq 3$. However, at low redshift, according to the study of the baryonic budget performed in Fukugita et al. (1998) and updated in Fukugita & Peebles (2004), only $\sim 10\%$ of these baryons are truly observed in gas and stars, in galaxies or galaxy clusters. The rest is more speculative. A fraction of 25% to 40% is thought to be in a Warm Hot

Intergalactic Medium, a very diffuse medium in the form of coronae around galaxies or filaments. The WHIM has not been convincingly observed yet. [Lehner et al. \(2007\)](#) estimates from observations of the Ly α forest at low redshift that it could constitute $\gtrsim 20\%$ of the baryonic fraction, and some other estimates of $30 - 40\%$ come from results of numerical simulations (e.g. [Davé et al. 2001](#)).

Depending on the chosen estimation, $\sim 50\%$ of baryons are not accounted for. This leaves room for potential baryonic dark matter, possibly in the outer parts of galactic discs (e.g. [Pfenniger et al. 1994](#); [Pfenniger & Combes 1994](#)). Cold dense gas could potentially be too difficult to observe, if it radiates very little or in difficultly observable wavelengths, or if it has a too little volume filling factor.

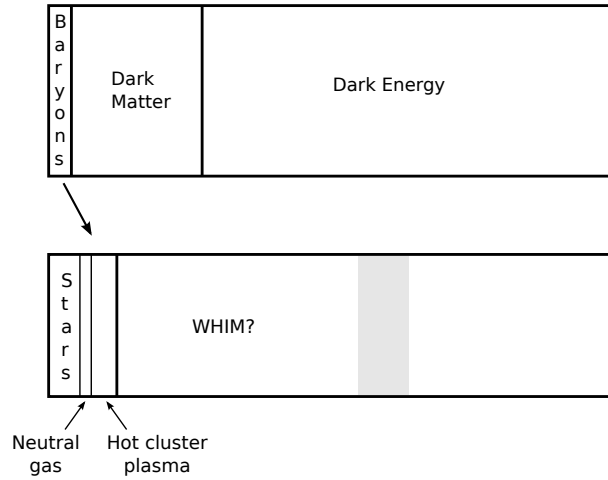


Figure 1.5: Schematic matter-energy content of the Universe respecting the Planck proportions (top) and speculative baryonic content derived from observations and simulations (bottom).

2.2 Organisation of galaxies at various scales

2.2.1 Clusters and groups

Some galaxies are observed to be gathered in gravitationally bound ensembles of several or many galaxies, respectively groups or clusters, with an arbitrary dividing line, the rest being “field” galaxies, relatively isolated.

The group of galaxies to which the Milky Way belongs is called the Local Group. Its size is of order of 1 Mpc. The Milky Way and Andromeda (M31) are its two more massive members, and most of the other members are satellites of these two galaxies. The two largest satellites of the Milky Way are irregular galaxies disrupted by their interaction with the Milky Way: the Small and Large Magellanic Clouds (SMC and LMC). These two satellites contain gas while all the other satellites of the Milky Way are so far observed to be gas-free dwarf spheroidals. Andromeda has a star-forming spiral satellite, M33, and dwarf ellipticals and

spheroidals as other satellites.

Clusters can contain as many as thousands of galaxies, extending over several Mpc. The closest cluster from the Milky Way is the Virgo cluster. Usually, one very massive elliptical galaxy is found at the centre of clusters. Other galaxies evolve around it, with a high velocity dispersion of around 1000 km/s. Some hot ($\sim 10^7$ K) intra-cluster gas is observed in X-ray.

2.2.2 Large-scale structures

At larger scales, galaxies are found to lie on a cosmic web, as shown on Figure 1.6. This is consistent with an evolution of the Universe driven by the counteracting effects of gravity and expansion: in such a situation with initial density fluctuations, overdense regions collapse while underdense regions become expanding voids. These voids will be separated by the collapsed matter that will take the aspect of sheets, lines or nodes between the voids.

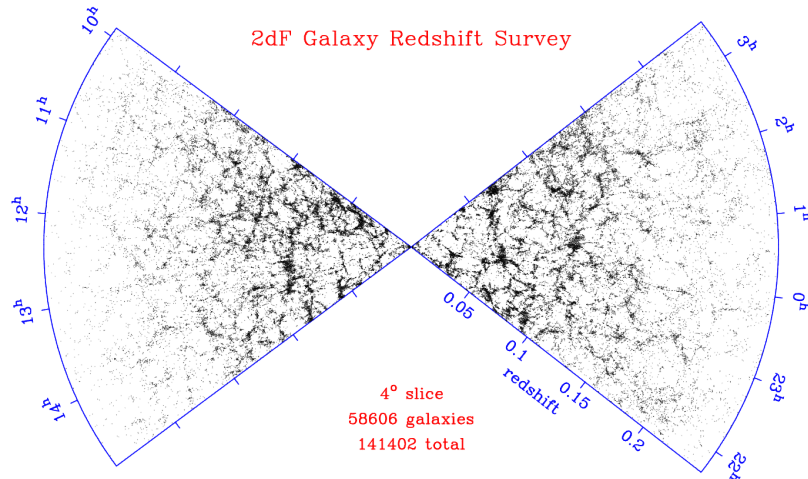


Figure 1.6: Spatial distribution of galaxies (each represented by a black dot) in the 2dFGRS survey. Figure from Peacock et al. (2001).

3 Some statistical properties

3.1 Bimodality

We saw in 1.1 (see Figure 1.2) that elliptical galaxies are redder and contain less gas than spirals. Galaxy surveys have shown a bimodality in the distribution of colours and magnitudes of galaxies in the local Universe. Figure 1.7 shows that two main populations of galaxies can be distinguished: a red and a blue sequence. The red sequence consists mainly of ellipticals being gas poor and thus having mostly old stars emitting in red wavelengths, and the blue sequence of spiral galaxies having a higher gas fraction and thus ongoing star formation that makes them appear bluer. The higher masses reached by ellipticals is consistent with the preferred scenario of structure formation according to which galaxies experience a varying

number of mergers during their lifetimes, which tend to increase their velocity dispersion, hence their spheroidal component, and heat their gas. The most massive ellipticals would thus be the product of numerous mergers.

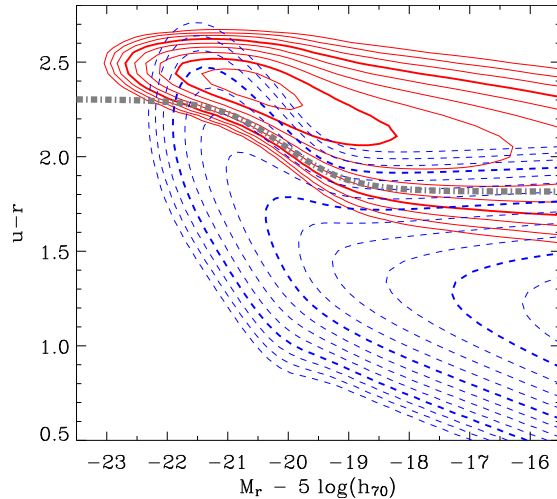


Figure 1.7: Colour-magnitude diagram of galaxies in the SDSS survey. Figure from [Baldry et al. \(2004\)](#).

3.2 Dependence on environment

The statistical morphologies of galaxies are a function of their environment: ellipticals and lenticulars are found in a higher fraction in clusters of galaxies. Their number fraction is up to $\sim 80\%$ in clusters, compared to $\sim 30\%$ in the field. Galaxies in clusters are also found to be on average more massive, less gas-rich and redder (e.g. [Kauffmann et al. 2004](#); [Baldry et al. 2006](#)). The higher fraction of ellipticals in clusters can be explained by the higher merger rate in groups that hierarchically form galaxy clusters. Ram-pressure stripping of the cold gas of spiral galaxies entering a cluster by intra cluster gas can explain their low gas fraction and red colour due to the lack of recent star formation.

Chapter 2

Spiral galaxies

Disc galaxies are thought to acquire their thin disc shape due to the dissipative property of gas. The dissipation causes loss of velocity dispersion and the gas settles in a flat disc perpendicular to the total angular momentum, the state of lowest energy for such a system in which angular momentum transfer is not very efficient. The Inter-Stellar Medium (ISM) of disc galaxies is observed to be a multiphase medium, as we will describe in this chapter. Star formation can be empirically related to the gas content. We will then present some aspects of the instabilities that give rise to the morphological features of disc galaxies: bars and spiral arms.

1 The ISM of spiral galaxies: content, physics and star formation

The ISM of galaxies is composed of gas, radiation and dust grains. We will first present these components with a focus on the molecular gas phase, and then detail some aspects of star formation.

1.1 Composition and phases

1.1.1 Dust

Dust grains are solid particles composed of heavy elements with varying sizes, mainly belonging to the range $0.01\text{--}0.2\mu\text{m}$, mixed with the interstellar gas. It was historically discovered by its obscuration effects on starlight. Despite its low mass contribution –the mass of dust is typically only 1% of the total mass of the ISM in a disc galaxy– it also has an impact on the thermal evolution of the ISM by cooling through infrared emission and heating through photoelectric effect on the grains, and on molecule formation by adsorption of atoms on the grains.

1.1.2 Radiation

Radiation in the ISM of disc galaxies comprises cosmic rays and electromagnetic radiation.

Cosmic rays are ions and electrons with a large kinetic energy that makes them very relativistic. Their origin (or more exactly the way they acquire this large energy) is a matter of debate. The main mechanism must however be through shocks, in particular in supernovae remnants (Bell 1978; Blandford & Ostriker 1978).

Electromagnetic radiation in the ISM encompasses photons with a variety of origins and frequencies: stars emit radiation from the infrared to the UV; ions, atoms or molecules in the ISM emit line-radiations with frequencies depending on their energy spectra; dust grains heated by starlight re-emit the radiation thermally in the infrared; hot ionised gas gives place to bremsstrahlung radiation, often from electrons interacting with ions and losing part of their energy given to a photon in the X-rays frequencies; relativistic electrons can emit radio radiation by the synchrotron effect due to magnetic fields; and some gamma rays can be produced in nuclear transitions or π^0 decays. A given galaxy may receive electromagnetic radiation due to other galaxies. A background common to all galaxies is the Cosmic Microwave Background field, emitted during the last moments of scattering of electrons by protons before recombination of hydrogen atoms in the early universe. This background has a temperature close to 3 K in the local Universe, and is thus at radio frequency.

1.1.3 Gas

The gas is observed to be in several phases with characteristic temperatures, densities and ionisation or molecule content (e.g. McKee & Ostriker 1977; Cox 2005; Krumholz et al. 2009a). The coldest gas is mainly in the molecular form and becomes mainly atomic and then mainly ionised if it is heated up. The different phases (numerical values from Draine (2011)) are:

- The Hot Ionised Medium (or coronal gas) that has a temperature $\gtrsim 10^{5.5}$ K and a number density $\sim 10^{-3}$ cm $^{-3}$. It has been heated by supernovae explosions or stellar winds. It can be observed in UV and X ray emission, or radio synchrotron emission.
- The Warm Ionised Medium (WIM) and the HII regions that have a temperature $\sim 10^4$ K and number densities in the range 0.3 – 10^4 cm $^{-3}$. HII regions have been photoionised by UV radiation from young massive stars. They can be in the form of dense ionised clouds near young stars, or more diffuse gas between clouds. The WIM encompasses low-density photoionised regions.
- The Warm Neutral Medium that has a temperature ~ 5000 K and a number density ~ 0.6 cm $^{-3}$.
- The Cold Neutral Medium that has a temperature ~ 100 K and a number density ~ 30 cm $^{-3}$. The Warm and Cold Neutral Media consist mainly of atomic hydrogen and are observed for example through the HI 21 cm line.

- The Molecular Medium that can be separated in two sub-categories: the diffuse molecular gas with a temperature ~ 50 K and a number density $\sim 100 \text{ cm}^{-3}$, and the dense molecular gas with a temperature ~ 10 K – 50 K and a number density $\sim 1 \times 10^3 \text{ cm}^{-3} - 1 \times 10^6 \text{ cm}^{-3}$.

The Molecular Medium Dense molecular gas, i.e. gas in molecular clouds, is itself very heterogeneous. Molecular clouds are indeed organised in Giant Molecular Clouds (GMCs) often themselves grouped in complexes, and, inside the GMCs, star-forming clumps can be found, having density peaks named molecular cores. Clouds having about the same density as GMCs but a lower mass can be called Dark Clouds, and can come in complexes as well. The various sizes, densities and masses of these systems are indicated in Table 2.1, taking values from [Draine \(2011\)](#), and an example of GMC complex is shown on Figure 2.1.

Denomination	Size [pc]	n_{H} [cm^{-3}]	Mass [M_{\odot}]
GMC Complex	25–200	50–300	10^5 – $10^{6.8}$
Dark Cloud Complex	4–25	10^2 – 10^3	10^3 – $10^{4.5}$
GMC	2–20	10^3 – 10^4	10^3 – $10^{5.3}$
Dark Cloud	0.3–6	10^2 – 10^4	5–500
Star-forming Clump	0.2–2	10^4 – 10^5	10 – 10^3
Core	0.02–0.4	10^4 – 10^6	0.3 – 10^2

Table 2.1: Categories of molecular clouds and complexes. From [Draine \(2011\)](#).

1.2 Molecular hydrogen

1.2.1 Properties of the molecule

The H_2 molecule consists of two H nuclei bound together by a covalent bond. It has excited states that can be due to its electronic state or to vibration or rotation of the molecule.

The first accessible excited electronic state is well above the ground state: at 11.2 eV from it, so it is very little populated in the molecular phase of the ISM of spiral galaxies. The energy of the molecule can change according to the distance between the atoms and the angular momentum of the molecule. The two H nuclei can indeed vibrate with respect to each other, or rotate around a symmetry axis orthogonal to the internuclear axis. The molecule thus has energy levels that can be labelled by a quantum rotational number J and a vibrational number v and can experience ro-vibrational transitions, i.e. transitions between states of different J and/or v . In the approximation of a harmonic-oscillator energy spectrum and a rigid-rotor rotation spectrum, the total rovibrational energy in the electronic state q can be written as:

$$E_q(v, J) = V_q(r_0) + h\nu_0\left(v + \frac{1}{2}\right) + B_v J(J + 1) \quad (2.1)$$

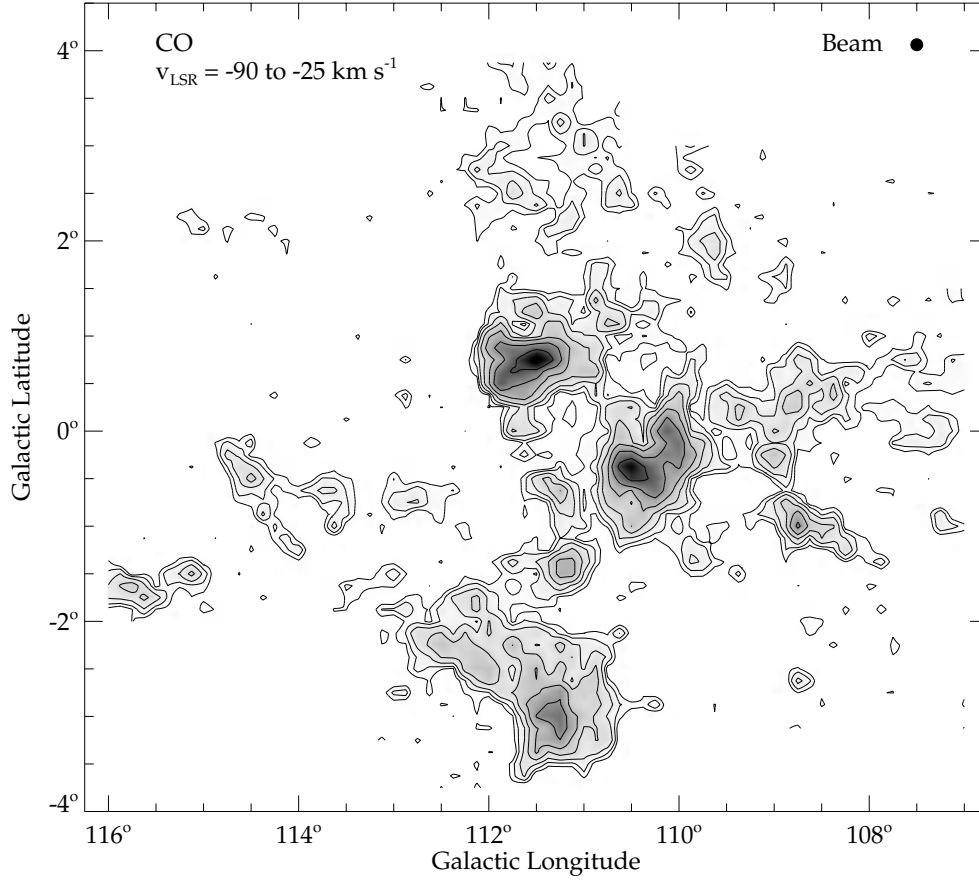


Figure 2.1: GMC complex in the Perseus arm. Map obtained from CO emission. For the estimated distance of 3.5 kpc, the height and width of the plot are respectively ~ 80 pc and ~ 90 pc. Figure from [Ungerechts et al. \(2000\)](#).

where r_0 is the distance minimizing V_q , the effective potential governing the internuclear separation in the electronic state q ($r_0 = 0.741$ in the ground electronic state), ν_0 is the vibrational frequency of the harmonic oscillator, and B_v is the “rotation constant” that depends on the vibrational state. In the ground electronic state, $h\nu_0 = 0.52$ eV and $B_v = 7.4$ meV (numerical values from [Huber & Herzberg \(1979\)](#)). As the molecule is symmetric, it has a null permanent electric dipole moment. The allowed radiative transitions are thus only quadrupole ones, that correspond to transitions between states with $\Delta J = 0, +2$ or -2 . Those transitions have probabilities that are much lower than the dipolar ones in non-symmetric diatomic molecules. Because of the relative values of ν_0 and B_0 , the energy levels of the ground electronic state consists of vibrational levels with sub rotational levels for each vibrational level, as represented in Figure 2.2.

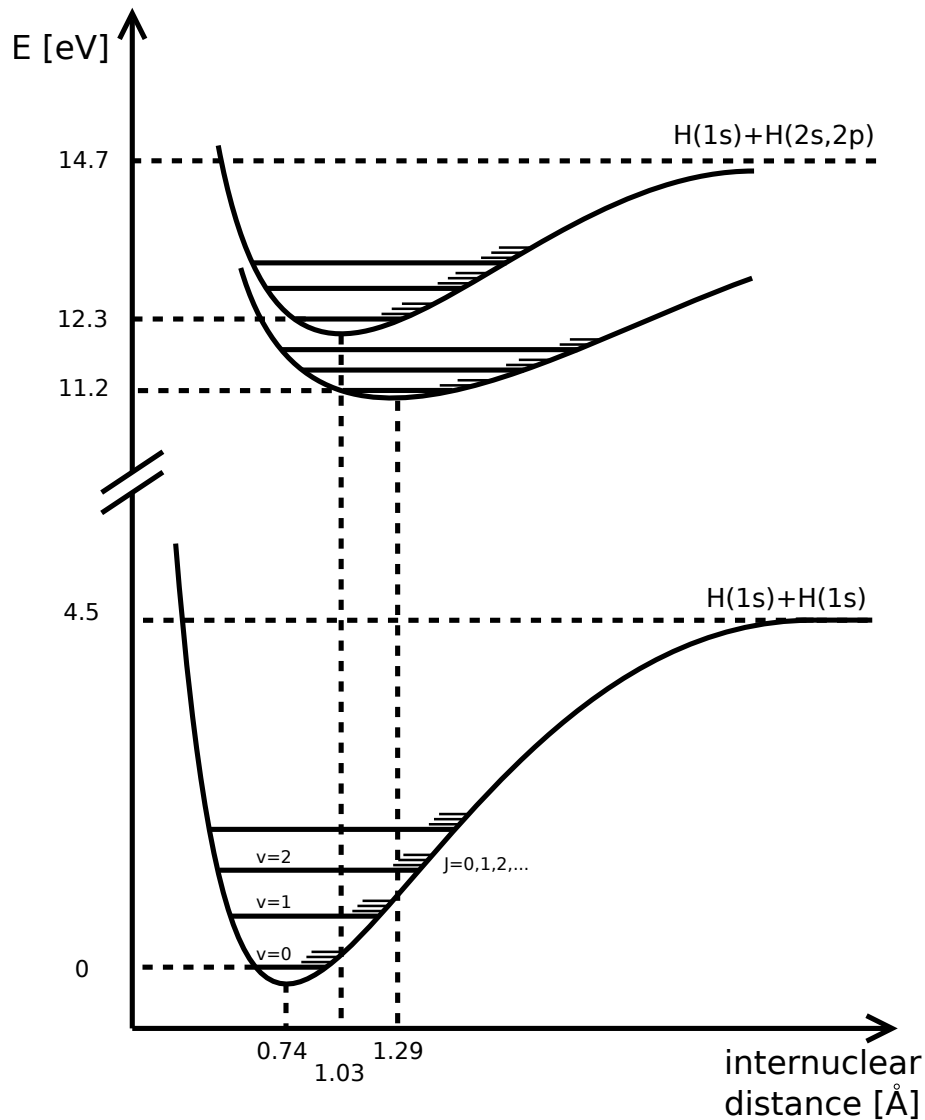


Figure 2.2: Ground electronic level, two first accessible electronic levels and their rovibrational sub-levels. The states corresponding to dissociated H atoms with electrons in either the ground electronic state 1s or one of the first electronic states 2s and 2p (both of same energy) are indicated.

1.2.2 Formation

The reaction $H + H \rightarrow H_2$ is exothermic: for two H atoms each in the ground electronic state, the reaction liberates 4.5 eV (as can be seen on Figure 2.2), that must be carried off for the molecule to be left in a bound state.

Gas-Phase formation Two H atoms approaching each other have a very small probability of forming an H_2 molecule because the symmetry forbids dipolar radiation from removing energy from the system, leaving only quadrupole transitions whose rate is very low to get rid

of the excess of energy. Another H atom can take off this energy in the case of a three-body reaction involving three H atoms, but the rate for three-body reactions is very low at the densities of the ISM.

H₂ can also form through a reaction with H⁻ (formed by $\text{H} + \text{e}^- \rightarrow \text{H}^- + h\nu$), with the detached electron in $\text{H}^- + \text{H} \rightarrow \text{H}_2 + \text{e}^-$ carrying off the energy. H⁻ is however little abundant in the ISM because it is quickly destroyed by reactions with positive ions or by photodetachment ($\text{H}^- + h\nu \rightarrow \text{H} + \text{e}^-$). The formation through H⁻ is the main one in the early Universe (e.g. Galli & Palla 1998).

Dust-catalysed formation As soon as dust is present, H₂ forms dominantly by adsorption on dust grains as described in Gould & Salpeter (1963); Hollenbach & Salpeter (1971, e.g.). An H atom can indeed become bound to the surface of a grain, diffuse on it until it becomes more strongly bound and trapped at a given position. If a new H atom that arrives on the grain meets the first atom before being trapped itself, the two atoms can form an H₂ molecule, liberating energy that will unbind the molecule from the dust grain and be partly given to the dust grain. As dust is made of metals, the rate of H₂ formation thus depends on metallicity.

1.2.3 Photodissociation

H₂ can be dissociated by Lyman-Werner photons, i.e. photons with energy in the range of 11.2 to 13.6 eV (higher energy photons being more likely to ionise H atoms as the corresponding cross section is larger), that can make the molecule reach an electronically excited state. De-excitation then results in a dissociation with a probability of $\sim 15\%$, when the molecule decays into the vibrational continuum of the ground electronic state (i.e. in an unbound state above 4.5 eV from the ground energy state) and gets quickly dissociated.

1.2.4 Shielding

H₂ molecules can be protected from such radiation if they are shielded by dust grains, H atoms or by other H₂ molecules. A region is shielded if it is surrounded by enough medium absorbing the radiation at the wavelengths that dissociate H₂. Regions of predominantly molecular gas are thus dense, allowing for sufficient shielding, and surrounded by Photo-Dissociation Regions (PDRs) in which the gas is mostly atomic (Hollenbach & Tielens 1999, e.g.). Self-shielding of H₂ is an efficient process (Draine & Bertoldi 1996; Wolcott-Green et al. 2011, e.g.), occurring at low column densities compared to other molecules like CO.

1.2.5 Observations of H₂ in the ISM

Absorption in the Lyman-Werner UV bands in the spectra of stars has been observed from space (the Earth atmosphere being almost opaque to UV radiation) (e.g. Spitzer et al. 1974;

Rachford et al. 2002). The vibrational lines can be observed in dense molecular gas excited by shocks, or in PDRs (e.g. Shull & Beckwith 1982). They are also observed in nuclei of active galaxies or starburst galaxies (having a particularly high star formation rate) because of UV pumping, i.e. the excitation to an excited electronic state followed by de-excitation in a vibrational excited state of the ground electronic level and subsequent cascade-like de-excitation into the lower vibrational level. Rotational lines have been observed in a number of environments, first in a PDR, the Orion Bar by Parmar et al. (1991).

The H_2 abundance is however very often deduced from observations of the CO molecule (e.g. Dickman et al. 1986; Solomon et al. 1997), that is assumed to trace H_2 reliably, except in low metallicity regions (where there is little CO and its relative abundance to H_2 is not well constrained). The CO molecule is not symmetric and has a $J = 1-0$ transition with a corresponding temperature of only 5 K, which makes it easily observable in emission. The mass of molecular clouds can be deduced from the determination of their velocity dispersion by the study of the $J = 1-0$ emission of CO and the use of the Virial theorem.

1.3 Cooling and heating in the ISM

The ISM gas can be heated and cooled by adiabatic contraction or expansion, shocks from supernovae explosions, and by a number of other processes depending on its temperature, ionisation state, radiation due to external sources or internal sources such as young massive stars, and chemical composition. The metal fraction in the gas phase is correlated with star formation, through the enrichment by stellar winds or supernovae explosions, and with possible inflows of extragalactic metal-poor gas.

1.3.1 Heating

Heating processes (see e.g. Dalgarno & McCray 1972) include photoionisation, in which the excess energy of a Far-UV (FUV) photon (for example a 20 eV photon ionizing a H atom with a 13.6 eV ionisation energy) is transferred into kinetic energy of the escaping electron that distributes it to the surrounding gas by collisions. A similar photoelectric heating occurs on dust grains or large molecules (Polycyclic Aromatic Hydrocarbons PAHs): electrons can be pulled out from dust grains or PAHs hit by energetic photons. Cosmic rays and X-rays can also heat the gas by ionising molecules or atoms.

1.3.2 Cooling

Radiative cooling, i.e. radiation loss due to the escape of photons from the ISM gas includes line cooling by atoms, ions or molecules. Line-cooling is due to the emission of a photon that allows to go from an energy state down to a lower energy state. The energy spectrum depends on the electronic configuration for atoms or mono-atomic ions but can also be a function of a whole molecule configuration, as in the case of the rotation or vibration

energy levels of diatomic molecules. The excitation to a high energy level can be due to collisions.

Collisional excitation is a cooling process because excited atoms or ions make transitions back to lower energy states by emitting photons. At low temperatures, from ~ 10 K to $\sim 10^4$ K, line cooling is dominated by molecules and a few metals (in atomic or ionised form). Around 10^4 K, the dominant cooling process is hydrogen Ly α emission due to collisional excitation. Between 10^5 and 10^7 K, cooling is dominated by collisional excitation of a few metal atoms or ions, mainly by the electrons provided by the ionisation of hydrogen. Recombination is also a cooling process because it removes the kinetic energy of the recombining electron from the gas, and so is collisional ionisation, because part of the kinetic energy is used for the ionisation.

At larger temperatures, above 10^7 K, the cooling is dominated by bremsstrahlung: free electrons are braked by ions and the lost energy escapes in the form of a photon.

The volume cooling rate or cooling function of plasmas (having a temperature above 10^4 K) has been computed for different metallicities by [Sutherland & Dopita \(1993\)](#); [Schure et al. \(2009, e.g.\)](#). Figure 2.3 shows the detailed contribution of cooling processes for hydrogen and helium cooling, as well as the cooling rate obtained for different metallicities.

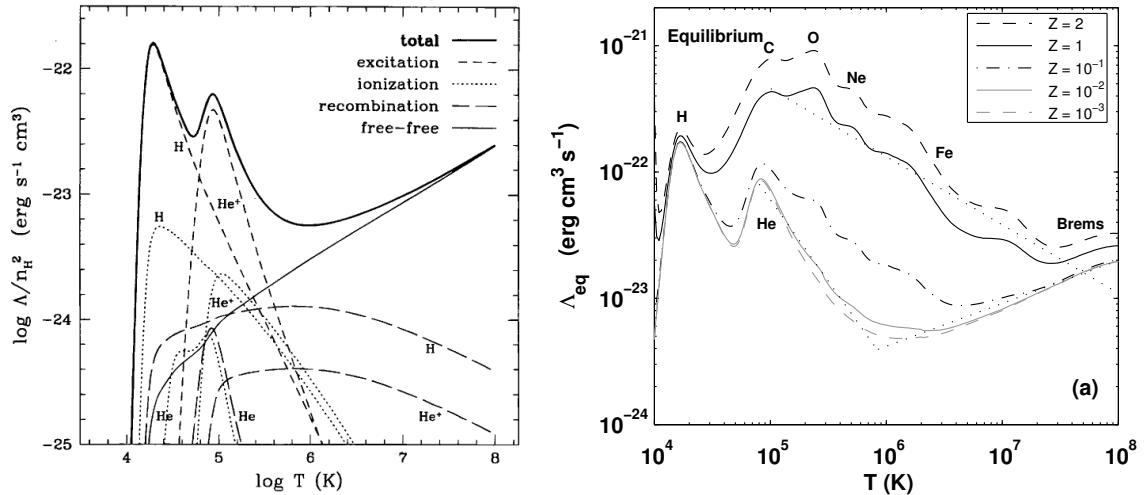


Figure 2.3: Left: contribution of different cooling processes to the total cooling due to hydrogen and helium from [Katz et al. \(1996\)](#). Right: cooling curves for different metallicities, with the various dominant cooling species indicated ([Gnat & Sternberg 2007](#)).

1.4 Star formation in spiral galaxies

1.4.1 Estimations of star formation rates

In galaxies where stars cannot be individually resolved, the Star Formation Rate (SFR) can be estimated from different types of observations relying on massive short-lived young

stars (Kennicutt 1998):

- The UV luminosity is dominated by these young massive short-lived stars, so it gives a good estimate of recent star formation, with a minimal dependence on the previous star formation history.
- Massive young stars have hot ionised atmospheres that radiate in H α . The H α emission is thus a good tracer of stars younger than around 10 Myr. For high redshift galaxies, the H α redshifted line falls outside the optical wavelengths when observed, so other lines such as the oxygen OII lines are often used to trace star formation.
- Dust absorbs the UV light emitted by young stars and reemits it in the far infrared. Far infrared observations can therefore give an indication of star formation rates. They can be combined with the other observations to account for all the star formation occurring in a galaxy.

Deducing the SFR from the light due to young massive stars, or ionisation processes occurring in their atmospheres requires the assumption of an Initial Mass Function (IMF). The IMF ϕ is such that $\phi(m)dm$ represents the number fraction of stars formed with a mass between m and $m + dm$. Salpeter (1955) deduced an initial mass function from observations in the solar neighbourhood. He found $\phi(m) \propto m^{-2.35}$ for stars in the mass range $0.4 M_{\odot} \leq m \leq 10 M_{\odot}$. Some other IMFs have been derived, for example the Scalo (1986) IMF, or the Kroupa (2002) IMF, that have slopes relatively close to the Salpeter slope for massive stars but extend the global mass range and break the power-law into different parts of different slopes according to the mass range, with slight variations between the two. These two IMFs are “top-heavy”, meaning that more high mass stars are formed than for the Salpeter IMF. In all these IMFs, the mass is dominated by low mass stars.

1.4.2 Star formation laws

Numerous attempts of relating the SFR to the gas properties have been made. Schmidt (1959) first proposed the Schmidt law using observations of local gas clouds:

$$\rho_{\text{SFR}} \propto \rho_{\text{gas}}^N \quad (2.2)$$

This relates the volume SFR ρ_{SFR} to the volume density of gas ρ_{gas} . Schmidt found $N \simeq 2$.

Kennicutt (1998) observed a sample of nearby spirals and starbursts galaxies and obtained as the best fit for the relation between the surface SFR Σ_{SFR} and the surface density of gas Σ_{gas} :

$$\Sigma_{\text{SFR}} = (2.5 \pm 0.7) \times 10^{-4} \left(\frac{\Sigma_{\text{gas}}}{M_{\odot} \text{ pc}^{-2}} \right)^N M_{\odot} \text{ yr}^{-1} \text{ kpc}^{-2} \quad (2.3)$$

with $N = 1.4 \pm 0.15$. This involved the average surface densities and SFRs of galaxies. Thanks to the increasing resolution of observations that is achievable, it is now possible to observe the SFR and surface density at sub-galactic scales. Bigiel et al. (2008) observed a sample of local galaxies with observational bin sizes of $750 \text{ pc} \times 750 \text{ pc}$. They find that the

SFR correlates well with gas density at surface densities larger than $10 M_{\odot}/\text{pc}^2$ with a slope of $\simeq 1$ while the correlation fails at lower densities and the slope is significantly higher (see Figure 2.4).

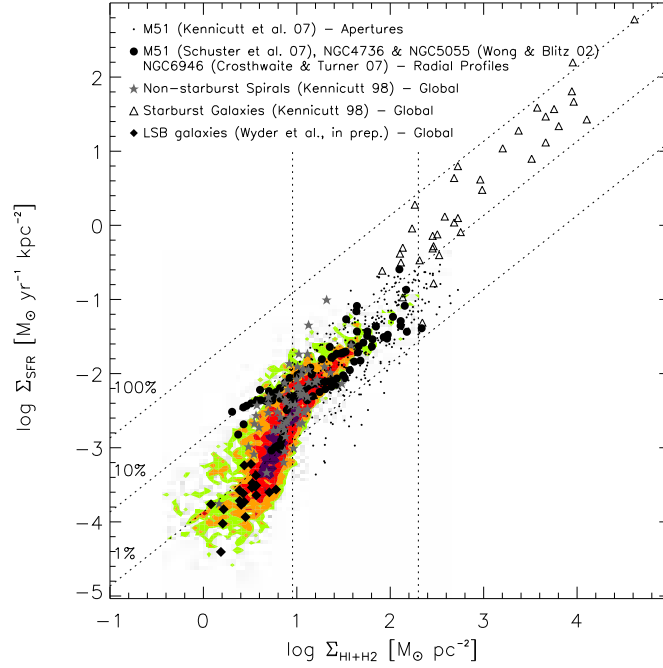


Figure 2.4: Compilation of observations of surface SFR vs $\text{HI}+\text{H}_2$ gas surface density. Colour-filled contours show results obtained from observations of 750 pc squared regions in local disc galaxies by Bigiel et al. (2008). Figure from Bigiel et al. (2008).

By separating gas between atomic and molecular hydrogen, Bigiel et al. (2008) find the high density zone is occupied by molecular hydrogen whose density correlates well with the SFR, while the low density is occupied by atomic hydrogen, with a poor correlation with SFR (see Figure 2.5).

1.4.3 Star formation trigger and regulation

Stars are formed in the densest parts of molecular clouds. The most obvious trigger for molecular cloud formation is gravitational instability: collapsing gas will eventually form stars when its density becomes high enough. Other processes such as supernovae explosions can shock gas to high densities, allowing for the gas to cool and form stars. Gas that enters density features such as spiral arms can also be compressed and give rise to star formation, as observations seem to indicate (see 2.1).

Star formation can be regulated by supernovae explosions that disrupt molecular clouds, or turbulence that stabilises the gas against gravitational collapse, but many uncertainties remain on the star formation process itself and what influences it the most. The same

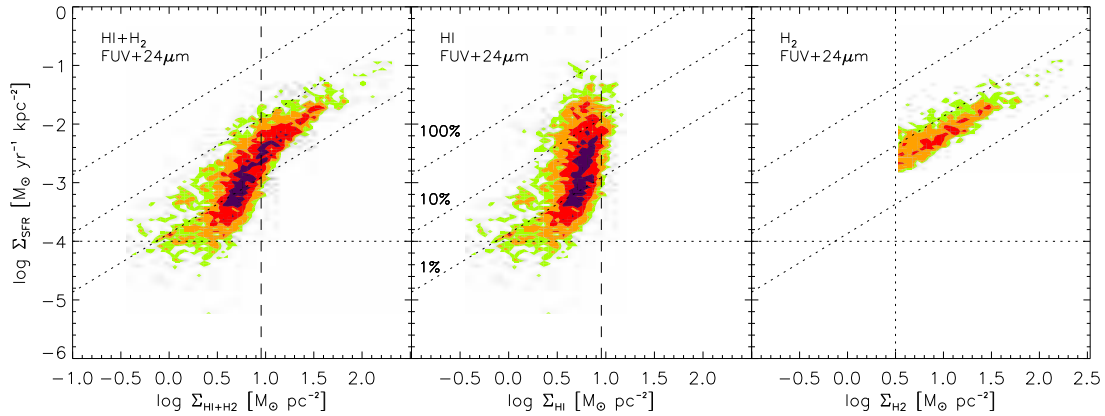


Figure 2.5: From left to right: surface SFR vs HI+H₂, HI and H₂ gas surface density. Results obtained from observations of 750 pc squared regions in 7 local disc galaxies by Bigiel et al. (2008).

processes that are thought to limit it can also enhance it: as previously mentioned, supernovae can also trigger star formation, and turbulence is also thought to play a triggering role (e.g. McKee & Ostriker 2007).

2 Instabilities, bars and spiral structure

2.1 Observations

2.1.1 Spiral arms

Optical observations of some galaxies show well defined spiral arms (often two) going from the centre to the external parts. These galaxies are called grand-design galaxies. Observations in several wavelengths (see Figure 2.6 for the example of M51) show that spiral arms are present for different components of the galaxies (de Vaucouleurs et al. 1991; Buta & Combes 1996, e.g.):

- the old stars observed in the near infrared;
- the young stars emitting the bulk of optical light and also observed by the H α emission in their hot atmospheres;
- neutral hydrogen gas observed by the radio 21 cm emission line of hydrogen;
- molecular gas observed through the radio CO rotational emission.

Some dust lanes are observed (by their obscuration on optical images or by their infrared emission) in the inside of the arms, indicating a compression of the ISM in these regions.

Some other kinds of spiral galaxies named flocculent galaxies appear globally as spiralling but without having arms defined from the inner regions to the outside. The arms seem to be due to differential rotation of young stellar regions (e.g. Gerola & Seiden 1978).

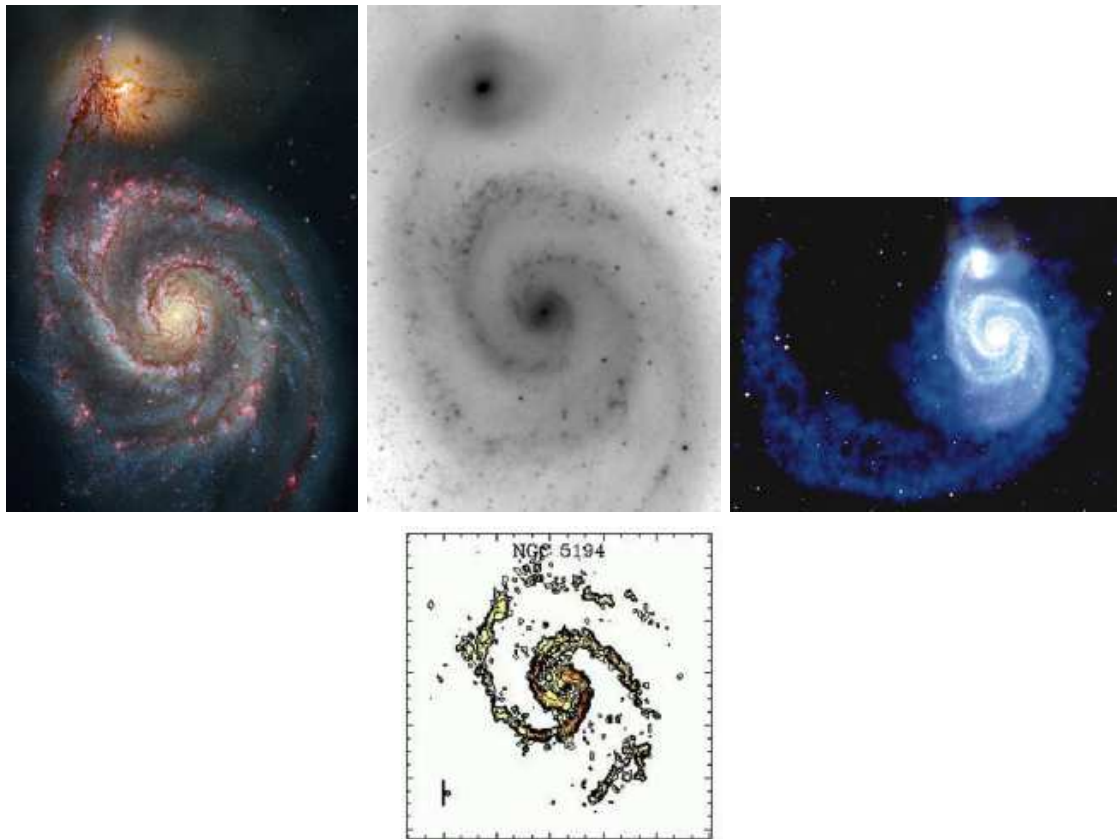


Figure 2.6: M51 (also referred to as NGC 5194) observed in different wavelengths. Its companion NGC 5195 is visible in the top left corner of the top row pictures. Top left picture: optical image from the Hubble Space Telescope with an emphasis on the $H\alpha$ Balmer line at 656 nm (pink features) and the near-infrared I band at 800 nm. Credits: S. Beckwith (STScI), Hubble Heritage Team, (STScI/AURA), ESA, NASA. Additional Processing by Robert Gendler. Top middle figure: near-infrared ($3.6 \mu\text{m}$) image from the IRAC instrument of Spitzer. Image adapted from [Buta et al. \(2010\)](#). Top right figure: superimposed optical image (in bright blue) and distribution of HI gas (darker blue) obtained from the HI 21 cm line. Image courtesy of NRAO/AUI and Juan M. Uson. Bottom row: Molecular gas distribution inferred from the CO emission, from [Regan et al. \(2001\)](#).

2.1.2 Bars

A high fraction of local disc galaxies are observed to be barred, $\sim 70\%$ when observed in the near infrared H band (e.g. [Eskridge et al. 2000](#)). The Milky Way itself is barred, and so are its two largest (and irregular) companions, the SMC and LMC. Bars are larger compared to the size of the disc in galaxies of type Sa than in Sb's or Sc's. Their isophotes are typically intermediate shapes between ellipses and rectangles, with a generally significant elongation. They exhibit dust lanes on their leading side (where “leading” refers to the rotation), and often some young stars near the tips of the bar.

2.2 Local instability

Discs are locally stabilised against gravitational collapse by either pressure in the case of gas discs, or velocity dispersion in the case of stellar discs. This stabilisation occurs for perturbations having a scale lower than the Jeans length λ_J (Jeans 1902), gravitational collapse being the winning process above this scale. This length can be derived from a number of methods: by using perturbation analysis of the fluid equations, by comparing counteracting forces, or by an analysis of the timescales involved (Schaye 2004). For a gaseous medium, a region of size L is stable against gravitational collapse if the sound crossing timescale $t_s = \frac{L}{c_s}$, with c_s the sound speed, is smaller than the dynamical timescale t_{dyn} . For a perturbation of volume density ρ , $t_{\text{dyn}} \propto \frac{1}{\sqrt{G\rho}}$, so $t_s < t_{\text{dyn}}$ if $L < \lambda_{J,\text{vol}}$ with:

$$\lambda_{J,\text{vol}} = \frac{c_s}{\sqrt{G\rho}} \quad (2.4)$$

For thin discs, studies in terms of the surface density are of special interest. The dynamical time for a perturbation of size L and surface density Σ is $t_{\text{dyn}} \propto \sqrt{\frac{L}{G\Sigma}}$, which sets another Jeans length:

$$\lambda_{J,\text{surf}} = \frac{c_s^2}{G\Sigma} \quad (2.5)$$

For stars, replacing the sound speed by the velocity dispersion σ (i.e. by considering the random motions of stars act like a pressure), one gets:

$$\lambda_{J,\text{vol}} = \frac{\sigma}{\sqrt{G\rho}} \quad (2.6)$$

$$\lambda_{J,\text{surf}} = \frac{\sigma^2}{G\Sigma} \quad (2.7)$$

On larger scales, discs are stabilised by differential rotation that counteracts local collapse for large enough perturbations, larger than a critical length λ_{crit} (Toomre 1964). Conservation of angular momentum indeed makes perturbations rotate around their own centres, adding to the support against gravitational collapse. The corresponding natural timescale is the epicyclic period, $t_{\text{dyn}} = \frac{2\pi}{\kappa}$, involving the epicyclic frequency κ of radial oscillations. This sets:

$$\lambda_{\text{crit}} = \frac{4\pi^2 G\Sigma}{\kappa^2} \quad (2.8)$$

In this (simple) analysis, perturbations are thus unstable only if they have sizes L such that $\lambda_{J,\text{surf}} < L < \lambda_{\text{crit}}$ (see Figure 2.7).

If the Jeans length is larger than λ_{crit} , perturbations of all scales will be stable. This is the case if $\frac{c_s \kappa}{2\pi G\Sigma} > 1$, which is different by just a factor 2 from the original Toomre criterion:

$$Q = \frac{c_s \kappa}{\pi G\Sigma} > 1 \text{ for stability} \quad (2.9)$$

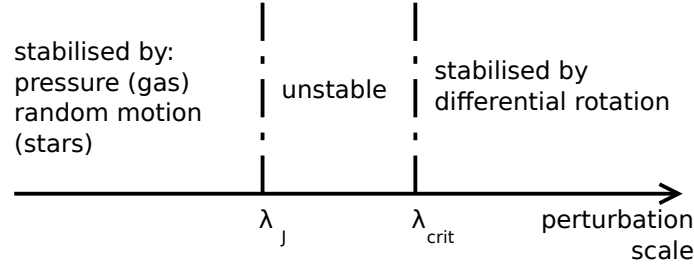


Figure 2.7: Schematic zones of stability or instability for perturbations in a disc.

Again, this criterion for a stellar disc is:

$$Q = \frac{\sigma \kappa}{\pi G \Sigma} > 1 \text{ for stability} \quad (2.10)$$

For discs composed of both stars and gas, some effective Toomre-like criteria have been proposed (e.g. [Jog & Solomon 1984](#)).

2.3 Nature of bars and spiral structure

Spiral structure is observed only in galaxies containing cold gas.

While the appearance of flocculent galaxies can be explained by local instabilities that have just been presented and that are sheared by differential rotation, the nature and generation of grand-design spiral arms is more problematic. If the arms were material arms, it can indeed be shown that differential rotation would wind them up much more tightly than what is observed, in a couple of Gyrs (e.g. [Binney & Tremaine 2008](#)).

[Lindblad \(1963\)](#) first suggested that spiral arms could be a pattern rotating as a solid body, with a uniform angular speed Ω_p . Particles of angular frequency Ω in nearly circular orbits can be approximated as having a radial oscillation of frequency κ . In general, $\Omega < \kappa < 2\Omega$. They can resonate with the spiral perturbation if their orbits are closed in a reference frame rotating at Ω_p , i.e. if $\Omega - \Omega_p = \frac{n\kappa}{m}$. The most common cases are $\Omega = \Omega_p$, “corotation”, $\Omega - \Omega_p = \frac{\kappa}{2}$, “inner Lindblad resonance” (depending on the form of Ω , there can be two inner Lindblad resonances), and $\Omega - \Omega_p = \frac{-\kappa}{2}$, “outer Lindblad resonance”.

Spiral arms are thought to be density waves ([Lin & Shu 1964](#)) that can be amplified by a “swing amplifier” mechanism, i.e. by reflections of wave packets on resonances (one inner Lindblad resonance and corotation resonance) that, together with differential rotation, make the wave amplitude grow (e.g. [Goldreich & Lynden-Bell 1965](#); [Toomre 1981](#)). However studies show that such waves are damped in a couple of galactic rotations. Spiral arms would thus be transiently excited by perturbations such as the tidal interaction with another galaxy (e.g. [Toomre 1981](#)), as seems to be the case of M51, or by bars.

2.4 Secular evolution

Internal evolution is thought to play a major role on the dynamics and morphology of disc galaxies on long time scales.

Spiral arms are almost only observed as being trailing, i.e. as being seemingly dragged by the disc rotation, which can be explained by the ability of trailing arms to transfer angular momentum away from the centre (e.g. Lynden-Bell & Kalnajs 1972), allowing galaxies to lower their energy.

Bars, by their action on the gas disc, can generate spiral arms in some cases where inner Lindblad resonances are present and make the stable orbits in the bar region rotate by 90° at each resonance, being ellipses with a major axis either parallel to the bar major axis or perpendicular to it. As the orbits of the gas –a collisional medium– can not cross, a spiralling pattern is created. However, the apparent link between bars and spiral arms in some grand-design spiral galaxies could sometimes be an illusion, as revealed by the often lower speed of the spiral arms compared to the bars (e.g. Sellwood & Sparke 1988). Bars can be easily destroyed. Shocked gas in the bar region can lose angular momentum and flow towards the centre of the galaxy (e.g. Bournaud et al. 2005), creating a central mass accumulation that will lead to chaotic orbits and destruction of the bar. A bar can be formed again due to external gas accretion (e.g. Bournaud & Combes 2002). A galaxy could thus experience several phases of bar formation and destruction.

Finally, vertical resonances in bars can lead to the buckling instability that can make bars appear as peanut-shaped (Combes et al. 1990), creating a pseudo-bulge, i.e. a structure resembling a normal central bulge, but differing by the kinematics of the stars (the support by rotation compared to velocity dispersion being higher in pseudo-bulges than in bulges), the density profile and the colour. Pseudo-bulges are frequently observed in spiral galaxies (e.g. Kormendy & Kennicutt 2004)

Chapter 3

Simulations of galaxies

Simulations of galaxies have made considerable progress in resolution and sophistication over the past decades, due to increase in computer power, algorithms which can compute gravitational and hydrodynamical forces both more efficiently and accurately, and advances in models of baryonic physics. The aim of simulations is to test hypotheses at various scales, for non-linear complex processes that cannot be studied analytically.

In this chapter, after a presentation of the variety of types of simulations aiming at studying galaxies, we will present the algorithms used to simulate the dynamics of different components of galaxies: cold dark matter (assumed to be a collisionless fluid), stars and gas, and then present how baryonic physics is introduced in simulations.

1 Different types of simulations

1.1 Cosmological simulations

Some simulations address the problem of galaxy formation and evolution on cosmological scales, starting for example with initial density fluctuations of dark matter in periodic boxes, allowing the study the hierarchical formation of dark matter haloes (e.g. [Navarro et al. 1997](#); [Springel et al. 2005](#)) with possible post-processing to try to match the baryonic matter distribution to the CDM distribution. If gas is also simulated (e.g. [Springel et al. 2008](#)), the galaxy formation process itself can be better studied in the cosmic dark matter web, including the interactions of galaxies with the intergalactic medium by gas accretion or outflows, mergers or tidal interactions of galaxies, or the effects of ram-pressure stripping in galaxy clusters. Those simulations usually have a low resolution at the level of individual dark matter haloes and galaxies, but it is possible to perform “zoom” simulations (e.g. [Navarro & White 1994](#); [Semelin & Combes 2005](#)), i.e. to re-simulate a zone of a simulation box with an increased resolution while taking into account the dynamical effects of the exterior of the re-simulated zone.

1.2 Galactic scale simulations

Other simulations, like the ones we will describe in this thesis, focus on isolated galaxies, or on a couple of galaxies so as to study galaxy interactions. The hypothesis that tidal interaction was the origin of patterns such as bridges between close galaxies and tails was in fact one of the motivations for the first simulations of galaxies. [Holmberg \(1941\)](#) simulated a system of two galaxies using light bulbs, making use of the analogous decline of the light flux and gravitational force with distance. Galaxies were then simulated for some time with stellar particles considered as test particles (neglecting self-gravity) for computational speed due to the limited calculation powers (e.g. [Toomre & Toomre 1972](#)). Fast algorithms for gravity computation and hydrodynamics (detailed later in this chapter), and increased computer power has allowed for self-gravity to be taken into account, and for gas to be included. Individual galaxies are now often modelled with a CDM halo.

Simulations of individual galaxies have the advantage of being simpler to perform than cosmological ones and of allowing for a high spatial and mass resolution. Problems such as the physical state of the ISM, its chemistry, star formation, or dynamical evolution by secular processes can be easily studied.

Finally, some simulations aiming at understanding the star formation process using a high resolution, while considering dynamical conditions of a galactic disc, can be performed by simulating gas in an external potential due to stars, with possible rotating spiral arms, and a CDM halo (e.g. [Dobbs & Bonnell 2008](#)). Some re-simulations of gas clouds can be performed ([Bonnell et al. 2013](#)).

Examples of hydrodynamical simulations at different scales can be seen on figure 3.1.

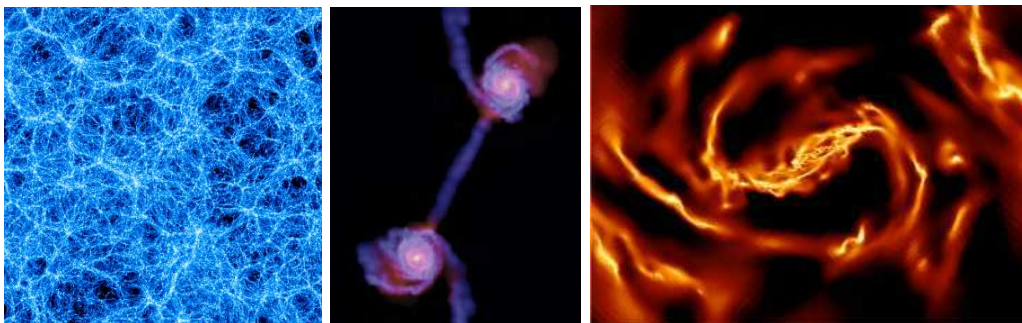


Figure 3.1: Gas density maps of simulations at different scales. Left: SPH structure formation simulation using Gasoline ([Wadsley et al. 2004](#)). $400 \text{ Mpc} \times 400 \text{ Mpc} \times 40 \text{ Mpc}$ slice. Credits: James W. Wadsley. Middle: SPH merger simulation using Gadget-2 ([Springel 2005](#)). Figure extracted from ([Di Matteo et al. 2005](#)). Right: AMR simulation of a disc galaxy similar to the LMC using RAMSES. Most refined regions are resolved with cells of width 0.8 pc . Box size: $4 \text{ kpc} \times 7 \text{ kpc}$. Figure from [Bournaud et al. \(2010\)](#).

2 Simulating stars and dark matter dynamics

Whether a system is collisional or not can be determined by comparing the relaxation time t_{relax} of the system – the time for which a particle has interacted gravitationally with enough other particles to lose memory of its initial conditions – to relevant time scales such as the crossing time, t_{cross} , the characteristic time in which a body crosses the system. A possibility to quantify t_{relax} is to study the deviations encounters will cause when a body of velocity \mathbf{v} crosses the system, and to define this time as the one for which the velocity change $\sqrt{\Delta v^2}$ becomes equal to the initial velocity of the body.

For a system of N bodies, such an approach gives the following relaxation time:

$$t_{\text{relax}} = \frac{N}{8 \ln \Lambda} t_{\text{cross}} \quad (3.1)$$

where $\ln \Lambda$ is the Coulomb logarithm: $\ln \Lambda = \ln \left(\frac{b_{\text{max}}}{b_{\text{min}}} \right)$. b_{max} and b_{min} are the maximal and minimal impact parameters of encounters. It can be shown that $\ln \Lambda \sim \ln N$ (e.g. Binney & Tremaine 2008). For a typical galaxy containing 10^{11} stars, this gives $t_{\text{relax}} \gg t_{\text{cross}}$.

Moreover, for a galaxy of radius R and mass M , the crossing time is of the order of $\simeq \frac{R}{v_c}$, where v_c is the circular velocity $v_c = \sqrt{\frac{GM}{R}}$. R is generally of the order of a few tenths of kpc, while v_c is of the order of 100 km/s. This gives a crossing time $\simeq \frac{1}{10} \frac{\text{kpc}}{\text{km/s}} \simeq \frac{1}{100} t_{\text{Hubble}}$, where $t_{\text{Hubble}} = 10 \frac{\text{kpc}/h}{\text{km/s}}$ is the Hubble time (h is the Hubble parameter), that gives an approximation of the age of the Universe (Springel 2009). For galaxies, as $t_{\text{relax}} \gg t_{\text{cross}}$ by much more than two orders of magnitude, one thus also has $t_{\text{relax}} \gg t_{\text{Hubble}}$. Stars in galaxies thus behave collisionlessly over the age of the Universe and should be treated accordingly in numerical simulations. Sellwood (2013) discusses relaxation in simulations of stellar discs.

2.1 The Vlasov-Poisson system

Stars or CDM particles can be described statistically as collisionless fluids by using a distribution function f such that $f(x, v, t) d^3x d^3v$ is the probability that the particles are in the phase-space volume $d^3x d^3v$ at time t , and that is normalised by:

$$\int f d^3x d^3v = 1 \quad (3.2)$$

The mass density is:

$$\rho = Nm \int f d^3v \quad (3.3)$$

with N the number of particles and m the (average) mass of a particle. In the absence of collisions, the Liouville theorem ensures conservation of the volume occupied by a constant

number of particles in phase-space, which can be written as a continuity equation for the distribution function f :

$$\frac{\partial f}{\partial t} + \frac{\partial(f\dot{\mathbf{w}})}{\partial \mathbf{w}} = 0 \quad (3.4)$$

where $\mathbf{w} = (\mathbf{x}, \mathbf{v})$. $\frac{\partial}{\partial \mathbf{w}}$ is a generalised divergence and $f\dot{\mathbf{w}}$ can be thought of as a streaming velocity in phase-space. The system of bodies is Hamiltonian and the divergence term in the continuity equation can be developed and simplified using the Hamilton equations $\dot{\mathbf{q}} = \frac{\partial H}{\partial \mathbf{p}}$ and $\dot{\mathbf{p}} = -\frac{\partial H}{\partial \mathbf{q}}$, where $\mathbf{q} = \mathbf{x}$ and $\mathbf{p} = m\mathbf{v}$. One obtains the Collisionless Boltzmann Equation, that, together with the Poisson equation, forms the Vlasov-Poisson system that accounts for the dynamical evolution of the system:

$$\frac{\partial f}{\partial t} + \mathbf{v} \cdot \frac{\partial f}{\partial \mathbf{x}} - \frac{\partial \phi}{\partial \mathbf{x}} \cdot \frac{\partial f}{\partial \mathbf{v}} = 0 \quad (3.5)$$

$$\Delta \phi = 4\pi G N m \int f d^3v \quad (3.6)$$

2.2 Algorithms for collisionless dynamics

Solving this Vlasov-Poisson system of integral partial differential equations involving 6 phase space coordinates in 3D (3 for position and 3 for velocity) is a challenge. A possibility is to consider truly the system as a 6 dimensional fluid and to solve the equations on a 6 dimensional grid (e.g. [Yoshikawa et al. 2013](#)), or on a cold 3D manifold ([Abel et al. 2012](#)), but the codes using these methods run slowly. Such simulations have already started being run thanks to the increased computer possibilities.

The two main alternative methods we will describe in more details rely on a sampling of the system, considering a lower number of particles and advancing their positions and velocities in time, using the computation of the gravitational forces in a way specific to each method. It can indeed be shown (e.g. [Binney & Tremaine 2008](#)) that the Vlasov-Poisson system can be approximated by using a Monte-Carlo sampling of the potential that amounts to considering a system of N bodies ($N \ll N_*$ for a system of N_* stars for example) and following their trajectories using Hamiltonian dynamics, i.e. by solving for each body the system of equation:

$$\dot{\mathbf{x}} = \mathbf{v} \quad (3.7)$$

$$\dot{\mathbf{v}} = -m\nabla\phi \quad (3.8)$$

Gravitation is a long-range force, making it very difficult to handle numerically as the force acting on one particle depends on all the other particles. Direct force summation is the only exact method but can be very time and memory consuming. For N particles, the number of gravitational forces to compute at each step of a time integration is the number of pairs of particles, $\frac{N(N-1)}{2}$, which for large numbers of particles scales as N^2 . The computation can be encoded in hardware in special-purpose devices such as GRAPE (e.g.

(Makino & Funato 1993), while some algorithms with a better scaling, typically $N \ln N$, have been developed, trying to keep a reasonable accuracy. In Tree methods (Barnes & Hut 1986), forces are computed using grouping of distant particles, while in the Particle Mesh method (e.g. Hockney & Eastwood 1981), the forces are obtained from the potential corresponding to the density on a spatial mesh put onto the particles.

This sampling to a lower number of particles than in the original system introduces some noise but will be accurate if the number of bodies N is such that the relaxation time remains larger than the time-scales of interest. The minimal approach of bodies must be taken care of as the fewer bodies there are, the less smooth the potential created by all the bodies will be, which increases the importance of encounters. A softening depending on the number of particles must therefore be introduced; it has to be increased when there are fewer particles. For mesh codes, the softening occurs at the cell size, while for pure N-body methods, a softening length is explicitly introduced.

2.2.1 Particle Mesh and variations

In particle mesh codes, space is divided into cells (usually cubes for 3D simulations). The gravitational forces that apply to particles are obtained by:

1. Computing the mass density on the grid;
2. Using this mass density to obtain the gravitational potential by solving the Poisson equation;
3. Calculating the forces on the grid from the potential;
4. Extrapolating the forces to the positions of the particles.

The mass density is computed for each cell using a “particle to cell” mass assignment. Each particle is given a “shape”, i.e. a mass distribution in space, and the density of a given cell is obtained from summing the contributions of particles whose extension overlaps with the cell. The simplest assignment scheme is the Nearest Grid Point scheme in which the shape function of a particle is a Dirac function, assigning its mass to the sole cell that encloses the particle. It is almost never used because it suppresses all spatial information below the cell size and induces discontinuities in the gravitational force applied to a particle when the particle changes cell. More sophisticated schemes allow for a more precise density field computation and also for the force, and possibly its derivatives, to be continuous:

- In the Cloud in Cell scheme, a particle mass is uniformly distributed over a cube of the same size of a cell, centred on the particle position, thus overlapping with $2^3 = 8$ cells in 3D. The force is then piecewise linear and continuous.
- In the Triangular Shaped Cloud scheme, a particle mass is distributed over a cube of width twice larger than a cell width, with a shape function that decreases linearly with the distance to the particle position and that overlaps with $3^3 = 27$ cells in 3D. The force and its first derivative are continuous.

The potential is often obtained from a Fourier transform of the density, using the relation between the density and the potential that applies to the problem (depending especially on the chosen boundary conditions). The gravitational force field is then obtained either firstly in the Fourier space before being reversely Fourier transformed, or from a finite difference scheme on the real potential obtained from a reverse Fourier transform of the Fourier potential. Forces are finally extrapolated to the positions of the particles, using for this the same shape function as for the density field computation, which ensures momentum conservation.

It is also possible to solve for the potential in real space, without resorting to Fourier transforms. This can be done by computing the density field as previously, by starting with a trial potential and iterating to find a potential field that satisfies a finite-difference approximation of the Poisson equation. Errors are quickly eliminated on the scale of a few grid cells, but a much higher number of iterations is needed for long-range interactions. To solve this problem, multigrid methods can be used: the iteration is done quickly on low resolution grid and is then refined on higher and higher resolution grids. The ART code (Kravtsov et al. 1997), MLAPM code (Knebe et al. 2001) and RAMSES code (Teyssier 2002) use this approach.

Improvements The PM scheme is quick and simple but the spatial force resolution is limited to about the cell size, which poses a serious problem for simulations involving highly clustered areas. These dense regions can difficulty be treated with the desired resolution because the cell size would have to be small everywhere, demanding a lot of memory and time, and creating numerical errors due to unphysical two-body relaxation in poorly populated regions that would be over-resolved.

Some refined methods can be used to increase the resolution only in areas of interest:

- In the Particle-Particle PM scheme (Hockney & Eastwood 1981), or P³M scheme, short-range forces (inside a cell) are computed using direct summation. It makes the dynamic range higher, but can be slow in the case of high clustering, if numerous particles are in the same cell. Couchman (1991) has developed an adaptive P³M, AP³M, refining clustered regions recursively with hierarchical grids and using a local PM algorithm to speed up the computation.
- In the Tree-PM scheme, the potential is split into a long-range potential computed with a PM algorithm, and a short-range potential computed with a Tree algorithm (detailed in the following section).
- In the Adaptive Mesh Refinement scheme (or AMR scheme), the grid is refined using sub-grids in clustered regions, so that the number of particles in a cell is roughly constant and relatively low. The algorithm is however complex and there is an ambiguity on the choice of secondary grids locations. This algorithm is for example used by ART Kravtsov et al. (1997), RAMSES (Teyssier 2002) or ENZO (O’Shea et al. 2004).

Another drawback of the PM scheme is that it induces force errors with preferred directions.

2.2.2 Tree algorithm

The principle of tree codes is to approximate the force on a particle by a multipole expansion based on a hierarchical grouping of particles. This hierarchical grouping, the Tree, can be done by a recursive splitting of space performed until the final regions contain only one particle. The root node of the Tree consists of all the particles, and branches lead to sub-nodes containing sub-groups of particles, these nodes being divided further and further until the “leaves” of the Tree that contain only one particle. In the Barnes-Hut algorithm (Barnes & Hut 1986), a cube containing all the particles is recursively split in 8. A Quad-Tree (the corresponding decomposition in 2D) is represented on Figure 3.2.

To compute the gravitational force on one particle, the Tree is walked down from the root node (containing all the particles) in its different branches, stopping, for a given branch, when an accuracy criterion is satisfied, basically when the ratio of the spatial extension of the Tree sub-domain to its distance to the particle falls below a certain value. This ratio, or opening angle θ , can be thought of as how the distant node is seen from the particle. If the angle is below the selected threshold, the sum of the forces due to the individual particles of the node can be approximated using a multipole expansion of the distribution of particles, truncated at a chosen order. The gravitational potential at position \mathbf{r} due to a group of particles at \mathbf{x}_i of masses m_i , total mass M , and centre of mass at \mathbf{s} is:

$$\phi(\mathbf{r}) = -G \sum_i \frac{m_i}{|\mathbf{r} - \mathbf{x}_i|} \quad (3.9)$$

$$= -G \left[\frac{M}{|\mathbf{r} - \mathbf{s}|} + \frac{1}{2} \frac{(\mathbf{r} - \mathbf{s})^T \mathbf{Q} (\mathbf{r} - \mathbf{s})}{|\mathbf{r} - \mathbf{s}|^5} \right] + o\left(\left(\frac{|\mathbf{s} - \mathbf{x}|}{|\mathbf{r} - \mathbf{s}|}\right)^2\right) \quad (3.10)$$

where index T indicates a transpose operation of the vector $(\mathbf{r} - \mathbf{s})$, and \mathbf{Q} is the quadrupole tensor:

$$Q_{ij} = \sum_k m_k [3(\mathbf{s} - \mathbf{x}_k)_i (\mathbf{s} - \mathbf{x}_k)_j - \delta_{ij} |\mathbf{s} - \mathbf{x}_k|^2] \quad (3.11)$$

Most of the time, either only monopoles are kept, or also quadrupoles.

In case θ is too high, the next nodes in the tree are recursively considered until the condition is satisfied for each sub-node and the contributions from all particles have been taken into account.

Tree codes have the advantage of not setting a limit for dynamic range, contrarily to a mesh with a fixed number of cells. The “mesh” here (i.e. the cubes of the Tree, empty cubes not being stored) adapt to the clumping. The force accuracy is also interestingly monitored by the threshold opening angle, and can be adjusted depending on the needs. Finally, tree codes allow for problems of any geometry to be studied, without risking that particles leave a fixed mesh.

Tree code scaling is in $N \ln N$ and depends only weakly on the clustering, but they are a little slower than PM codes. This is modulated by the possibility of computing forces only for a small number of particles in time-integration involving individual time-steps, contrarily to PM codes that require the whole force field to be computed to obtain the force applying

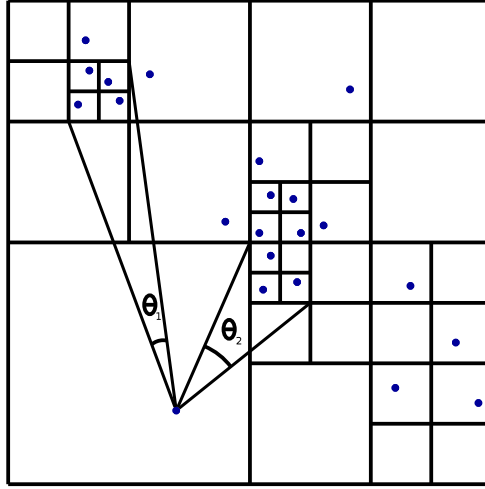


Figure 3.2: Quad-tree (in 2 dimensions). For a threshold opening angle θ , if $\theta_1 < \theta < \theta_2$, the node seen with an angle θ_2 will be opened and the force will be computed using the 4 corresponding leaves of the tree, while a multipole expansion will be used to compute the contribution of the node seen with an angle θ_1 .

to a restricted number of particles. Another drawback of Tree methods is that they do not manifestly conserve momentum because of errors due to the truncation of multipole expansions.

A different use of the tree construction for force computation is made in the Fast Multiple Method (Dehnen 2002), in which the forces are computed symmetrically for each pair of interacting nodes, ensuring therefore momentum conservation. The code is very fast, scaling as N , but it does not work as well as the tree code for individual time-steps, and is difficult to parallelise efficiently on memory distributed machines.

Force softening For N-body techniques (direct summation or Tree codes), the softening necessary to avoid any collisional behaviour is done by replacing the potential of a point mass m , $\phi(r) = -\frac{Gm}{r}$ by a potential that will not become infinite for small distances. The most natural choice is the Plummer softening:

$$\phi(r) = -\frac{Gm}{\sqrt{r^2 + \epsilon^2}} \quad (3.12)$$

where ϵ is the softening length, but this form of potential has the disadvantage of differing from the Newtonian potential at all distances, which introduces a systematic error. A better possibility is to modify the potential only at small distances where relaxation problems occur. One replaces the density of a point mass $\rho(r) = m\delta(r)$ by $\rho(r) = mW(\frac{r}{h})$, where h is a softening length parameter and W is a finite-support softening kernel (so that the potential is Newtonian at large distances). The following spline kernel (see left panel of Figure 3.3) is

the most often used kernel:

$$W(u) = \begin{cases} 1 - 6u^2 + 6u^3, & \text{if } u < \frac{1}{2} \\ 2(1 - u^3), & \text{if } \frac{1}{2} \leq u < 1 \\ 0 & \text{if } u \geq 1 \end{cases} \quad (3.13)$$

The associated potential has a finite value at $r = 0$ contrarily to the Newtonian one, and becomes Newtonian at $u = 1$. It is roughly equivalent to a Plummer potential if $h = 2.8\epsilon$ (see right panel of Figure 3.3).

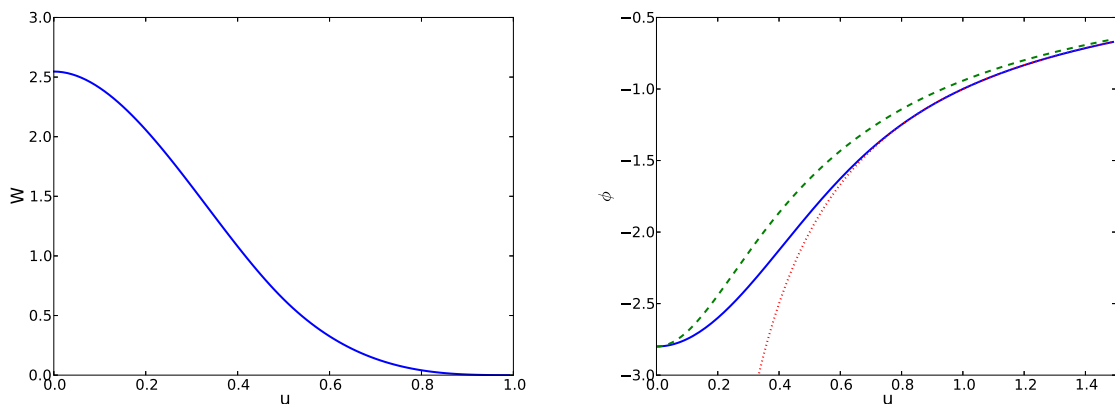


Figure 3.3: Left: Cubic spline softening kernel. Right: potential of a point mass for a Newtonian potential (dotted line), a Plummer potential with softening $\epsilon = \frac{1}{2.8}$ (dashed line) and using the cubic spline with $h = 1$ (solid line)

2.3 Time integration

We have so far presented the way gravitational forces are computed. To solve for the motion of particles, the time is discretised into time-steps, updating velocity and position using the force computation and repeating the process with the updated spatial repartition of particles.

To conserve energy and phase-space volume as imposed by the Hamiltonian evolution, an adequate time integrator has to be chosen, a symplectic integrator, having a mapping between coordinates of the last time-step and the present time-step that has a unity Jacobian determinant. The most straightforward explicit Euler scheme and the Runge-Kutta integration scheme do not satisfy this condition, and accumulate errors at each time-step. The most used symplectic integrator is the Kick-Drift-Kick second order integrator (analogous to a “leap-frog” integrator). A Kick transformation advances velocities while keeping positions fixed, and a Drift transformation advances positions while keeping velocities fixed. Velocities

\mathbf{v} and positions \mathbf{x} are thus updated the following way:

$$\mathbf{v}^{t+\frac{\Delta t}{2}} = \mathbf{v}^t - \nabla\phi^t \frac{\Delta t}{2} \quad (3.14)$$

$$\mathbf{x}^{t+\Delta t} = \mathbf{x}^t + \mathbf{v}^{t+\frac{\Delta t}{2}} \Delta t \quad (3.15)$$

$$\mathbf{v}^{t+\Delta t} = \mathbf{v}^{t+\frac{\Delta t}{2}} - \nabla\phi^{t+\Delta t} \frac{\Delta t}{2} \quad (3.16)$$

This integrator is used by Gadget-2 with which we have performed our simulations.

3 Simulating gas dynamics

The gas of the ISM can be modelled in different ways, depending on the physical assumptions that are made. It is usually considered as a collisional fluid, but sometimes as a cloudy heterogeneous medium. We will present the latter briefly and then detail Eulerian and Lagrangian algorithms commonly used to model a continuous ISM.

3.1 Sticky particle algorithm

The sticky particle scheme (e.g. [Brahic 1977](#); [Levinson & Roberts 1981](#)), aims at being a realistic simulation of the heterogeneous and non thermal ISM. Particles represent gas clouds and interact with each other through inelastic collisions in which they can form stars or coalesce (e.g. [Combes & Gerin 1985](#)), forming a whole mass spectrum. The velocity dispersion of particles differs from the thermal sound speed.

3.2 Hydrodynamics algorithms

The time evolution of the properties of a collisional gas fluid of density ρ , pressure P and specific energy (internal energy per unit mass) u follow from the continuity, Euler and energy equation:

$$\frac{\partial \rho}{\partial t} + \nabla \cdot (\rho \mathbf{v}) = 0 \quad (3.17)$$

$$\frac{\partial \mathbf{v}}{\partial t} + \mathbf{v} \cdot \nabla \mathbf{v} = -\frac{\nabla P}{\rho} - \nabla \phi \quad (3.18)$$

$$\frac{\partial u}{\partial t} + \mathbf{v} \cdot \nabla u + \frac{P}{\rho} \nabla \cdot \mathbf{v} = \mathcal{H} - \mathcal{C} \quad (3.19)$$

The first equation accounts for mass conservation, the second one is the Euler equation for a fluid submitted to a gravitational potential ϕ , and the third one describes the evolution of the specific energy in the presence of possible source and sink terms for heat: respectively \mathcal{H} and \mathcal{C} .

The system of equations can be closed by an equation of state. For an ideal gas of constant ratio of specific heat at constant pressure to specific heat at constant volume γ , one can write:

$$P = (\gamma - 1)\rho u \quad (3.20)$$

The evolution equations involve time derivatives at a fixed point in space. If one wishes to follow the time evolution of properties of a fluid element moving along with the fluid, the adequate derivative is the convective derivative $\frac{d}{dt} = \frac{\partial}{\partial t} + \mathbf{v} \cdot \nabla$. The evolution of the density, velocity and specific energy of this element are thus:

$$\frac{d\rho}{dt} + \rho \nabla \cdot \mathbf{v} = 0 \quad (3.21)$$

$$\frac{d\mathbf{v}}{dt} = -\frac{\nabla P}{\rho} - \nabla \phi \quad (3.22)$$

$$\frac{du}{dt} + \frac{P}{\rho} \nabla \cdot \mathbf{v} = \mathcal{H} - \mathcal{C} \quad (3.23)$$

The main algorithms for hydrodynamics use either a Eulerian, either a Lagrangian description of the fluid. In the Eulerian view, space is discretized and what is followed in time is the evolution of velocity, density, pressure and energy at fixed spatial points, while in the Lagrangian view, mass is discretized: one considers conceptual small fluid elements of an infinitesimal mass, and follows their velocity, density, pressure and energy as they move with the fluid (see Figure 3.4).

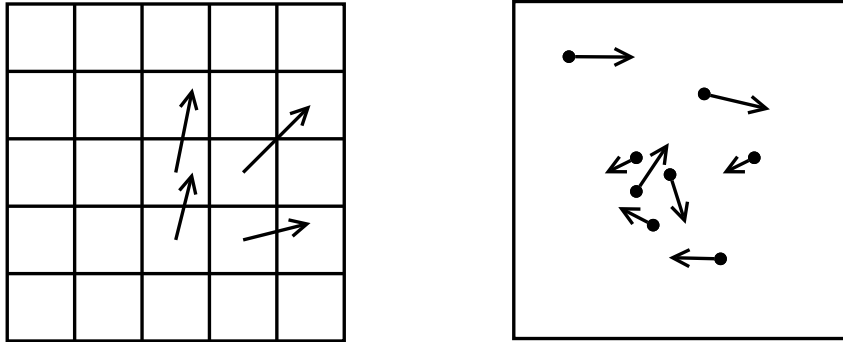


Figure 3.4: Left: Eulerian volume discretisation scheme used by mesh algorithms. Each cell has attached properties (density, velocity, internal energy...). Right: Lagrangian mass discretisation used by the SPH algorithm. Each point mass has attached properties.

3.2.1 Grid codes

The continuity, Euler and energy equations can all be written in the form:

$$\frac{\partial q}{\partial t} + \nabla \cdot \mathbf{F} = 0 \quad (3.24)$$

where q is the mass density ρ , linear momentum per unit mass $\rho\mathbf{v}$, or energy per unit mass $u + \frac{\rho v^2}{2}$ and \mathbf{F} is the corresponding flux. In grid codes, the fluid dynamical equations are

discretized at the cell scale, and a computation of the fluxes is carried out between adjacent cells. The implementations vary in the exact way the fluxes are computed. Many codes use the Godunov scheme, in which the fluxes are obtained using the exact solution of the Riemann problem for each interface between two cells, which ensures exact total energy conservation in the case where no gravity is included (e.g. Teyssier 2002). Mesh codes are thus well designed to treat shocks efficiently.

One of their drawbacks is that Galilean invariance is not enforced (e.g. Wadsley et al. 2008). A numerical truncation error depending on the cell width makes the behaviour of a fluid differ if the same velocity is added everywhere. This unwanted effect can however be reduced by increasing the spatial resolution.

3.2.2 SPH

Smoothed particle hydrodynamics was independently developed by Lucy (1977) and Gingold & Monaghan (1977). The fluid is treated in a Lagrangian way, by a further step compared to the original Lagrangian formalism that is the sampling of the fluid by point masses acting as a set of discrete tracer particles. The density at the point mass locations is done by a local average on neighbouring particles. A number of TreeSPH codes, using the Tree algorithm to compute gravitational forces, as gas are treated as particles in SPH, have been developed: Hernquist & Katz (1989) first combined the two methods, and more recent codes such as Gadget-2 (Springel 2005) or Gasoline (O'Shea et al. 2004).

The algorithm is based on a kernel interpolation. An interpolated version of any field $A(\mathbf{r})$ can be defined using a convolution with a kernel $W(\mathbf{r}, h)$:

$$\langle A(\mathbf{r}) \rangle = \int A(\mathbf{r}') W(\mathbf{r} - \mathbf{r}', h) d\mathbf{r}' \quad (3.25)$$

with h the characteristic width of the kernel, called the smoothing length. The kernel must be normalised to unity ($\int W(\mathbf{r}, h) d\mathbf{r} = 1$) and reduce to a Dirac distribution in the limit $h \rightarrow 0$. It is required to be spherically symmetric for angular momentum conservation, and to have a high order of interpolation.

The most used kernel is the same cubic spline kernel as often used for gravitational softening (see equation 3.13), proposed for SPH interpolation by Monaghan & Lattanzio (1985). It is a spherically symmetric kernel normalised to unity in three dimensions, i.e. $\int W(r, h) 4\pi r^2 dr = 1$, with a high order of interpolation. Starting with the lowest order kernel, the Dirac kernel, it can be obtained by performing four successive convolutions with a door function, by scaling the resulting kernel to have the desired support and by finally normalizing it to unity.

If the field A is known only at certain points \mathbf{r}_i that have an associated mass m_i and a density ρ_i , and so an associated volume element $\frac{m_i}{\rho_i}$, one can approximate the integral by an interpolated summation on the values $A_i = A(\mathbf{r}_i)$ by replacing the integral by a summation,

with the replacement $d\mathbf{r} \mapsto \frac{m_i}{\rho_i}$:

$$\langle A(\mathbf{r}) \rangle \simeq \sum_j \frac{m_j}{\rho_j} A_j W(\mathbf{r} - \mathbf{r}_j, h_i) \quad (3.26)$$

where the summation is on a limited number of particles in the case of a finite-support kernel, these particles being called the neighbours of particle i . Their number depends on the choice of estimation of the smoothing length.

The density can therefore be estimated at any position by:

$$\rho(\mathbf{r}) = \sum_j m_j W(\mathbf{r} - \mathbf{r}_j, h), \quad (3.27)$$

and can be in particular estimated at the positions of the sampling particles. Mass conservation is automatically fulfilled. Figure 3.5 shows a schematic SPH kernel volume around a particle i .

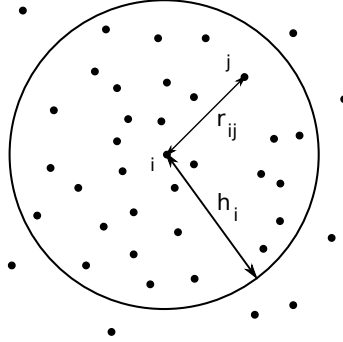


Figure 3.5: Schematic view of an SPH kernel volume of radius h_i around a particle i . r_{ij} is the length of $\mathbf{r}_{ij} = \mathbf{r}_i - \mathbf{r}_j$. The density ρ_i is obtained by the summation of the masses of particles inside the volume, weighted by the kernel function W .

The other partial differential equations – the Euler and energy equations – can be discretised and transformed into ordinary differential equations for the velocity and the specific energy, using the properties of the kernel interpolation. There is a number of choices for the exact way the discretisation is performed. The $-\frac{\nabla P}{\rho}$ term in the Euler equation is often symmetrised so as to obtain antisymmetric forces between two particles and conserve momentum. Using $\frac{\nabla P}{\rho} = \nabla \left(\frac{P}{\rho} \right) + \frac{P}{\rho^2} \nabla \rho$ and a symmetrised kernel for two particles i and j $\overline{W}_{ij} = \frac{1}{2}(W(|\mathbf{r}_{ij}|, h_i) + W(|\mathbf{r}_{ij}|, h_j))$, it is possible to write:

$$\frac{d\mathbf{v}_i}{dt} = - \sum_{j=1}^N m_j \left(\frac{P_i}{\rho_i^2} + \frac{P_j}{\rho_j^2} \right) \nabla_i \overline{W}_{ij} \quad (3.28)$$

and, without considering source or sink terms in the energy equation, it is also possible to write:

$$\frac{du_i}{dt} = \frac{1}{2} \sum_{j=1}^N m_j \left(\frac{P_i}{\rho_i^2} + \frac{P_j}{\rho_j^2} \right) \mathbf{v}_{ij} \cdot \nabla_i \overline{W}_{ij} \quad (3.29)$$

Other symmetrisations can be obtained from writing for example $\frac{\nabla P}{\rho} = \frac{2\sqrt{P}}{\rho}\nabla\sqrt{P}$ (e.g. Monaghan 1992).

Artificial viscosity Such an integration scheme relies on differential fluid equations whose validity breaks down in the case of shocks. In discontinuous shock regions, the integral form of the equations are required. Without any addition to the discretised equations, SPH would miss the dissipation of kinetic energy into thermal energy by microphysics in these regions.

Therefore, an artificial viscosity is introduced to generate dissipation due to shocks and spread the shock on a resolvable layer, i.e. two or three smoothing lengths, making the use of the differential form of the equations correct in these regions. This artificial viscosity is put as a friction force that damps the relative motions of particles:

$$\left.\frac{d\mathbf{v}_i}{dt}\right|_{\text{visc}} = -\sum_{j=1}^N m_j \Pi_{ij} \nabla_i \bar{W}_{ij}, \quad (3.30)$$

where $\Pi_{ij} \geq 0$ is an artificial viscosity tensor that is non-zero only when particles approach each other.

The exact choice for the viscosity form and parametrisation vary. The code Gadget-2 we use for our simulations takes a parametrisation from Monaghan (1997) that involves a “signal velocity” $v_{ij}^{\text{sig}} = c_i + c_j - 3w_{ij}$ where $w_{ij} = \frac{\mathbf{v}_{ij} \cdot \mathbf{r}_{ij}}{|\mathbf{r}_{ij}|}$ (from an analogy with the Riemann problem) in the case particles approach each other. $w_{ij} = 0$ otherwise. Π_{ij} takes the form:

$$\Pi_{ij} = -\frac{\alpha}{2} \frac{(c_i + c_j - 3w_{ij}) w_{ij}}{\rho_{ij}} \quad (3.31)$$

where $\alpha \simeq 0.5 - 1.0$. ρ_{ij} is the arithmetic mean of the densities of particles i and j . Multiplication by w_{ij} in Π_{ij} ensures the viscosity vanishes for rigid body rotation. This version prevents very large viscous accelerations from occurring. Moreover, a viscosity limiter is added following Balsara (1995) and Steinmetz (1996), so as to reduce the artificial viscosity in shear flows.

As the aim of this artificial viscosity is to convert some kinetic energy into thermal energy, the decrease in kinetic energy due to the viscous force is exactly balanced by an increase in thermal energy:

$$\frac{du_i}{dt} = \frac{1}{2} \sum_{j=1}^N m_j \Pi_{ij} \mathbf{v}_{ij} \cdot \nabla_i \bar{W}_{ij}, \quad (3.32)$$

and the total energy is thus conserved.

Energy or entropy integration If the internal energy is integrated, Hernquist (1993) showed that conservation of entropy can be violated (for adiabatic flows in which no entropy should be generated). Without any cooling included, the entropy can diminish, which is not physical.

Another possibility is to follow the evolution of an entropy function rather than the internal energy. One can use:

$$A = \frac{P}{\rho^\gamma} \quad (3.33)$$

with γ the adiabatic index of the gas, equal to $\frac{5}{3}$ for a mono-atomic gas. For an adiabatic flow, this function is constant and in bijection with the specific entropy s ¹.

This entropy function, that will be hereafter called simply entropy, will have an evolution due only to the artificial viscosity (in the absence of other cooling or heating terms):

$$\frac{dA_i}{dt} = \frac{1}{2} \frac{\gamma - 1}{\rho_i^{\gamma-1}} \sum_{j=1}^N m_j \Pi_{ij} \mathbf{v}_{ij} \cdot \nabla_i \bar{W}_{ij} \quad (3.34)$$

As this is positive definite, the entropy can only grow in time. The internal energy can be obtained from:

$$u_i = \frac{A_i}{\gamma - 1} \rho_i^{\gamma-1} \quad (3.35)$$

[Hernquist \(1993\)](#) however showed that if the entropy is integrated, the total energy is not necessarily conserved, problems arising from the adaptive behaviour of SPH, from neglected terms due to the variation of the smoothing lengths in space and time.

Conservative form A better way of solving for the evolution of a fluid in a conservative manner is to write a Lagrangian for the gas and to derive a discretised Euler equation from it. As the equation will be derived from a Lagrangian, energy and momentum conservation will automatically be enforced. [Springel & Hernquist \(2002\)](#) present such an approach and use in the Gadget-2 code. The Lagrangian for N particles (with no self-gravity added here) can be written as:

$$\mathcal{L}(q, \dot{q}) = \frac{1}{2} \sum_{i=1}^N m_i \dot{r}_i^2 - \frac{1}{\gamma - 1} \sum_{i=1}^N m_i A_i \rho_i^{\gamma-1} \quad (3.36)$$

where $q = (r_1, \dots, r_N, h_1, \dots, h_N)$. The A_i are the specific entropy of particles.

By taking into account the constraints ϕ_i expressing that the mass in a kernel volume is demanded to equal a constant M_{SPH} , i.e.:

$$\phi_i = \frac{4}{3} \pi h_i^3 \rho_i - M_{\text{SPH}} = 0, \quad (3.37)$$

it is possible to derive a discretised Euler equation using the Lagrangian equations:

$$\frac{d}{dt} \frac{\partial \mathcal{L}}{\partial \dot{q}_i} - \frac{\partial \mathcal{L}}{\partial q_i} = \sum_{j=1}^N \lambda_j \frac{\partial \phi_j}{\partial q_j} \quad (3.38)$$

1. Indeed, applying the thermodynamical identity $du = Tds + \frac{P}{\rho^2} d\rho$ to an isolated ideal gas having $P = (\gamma - 1)\rho u$, $u = \frac{kT}{\mu(\gamma - 1)}$ with μ the mean particle weight, one finds $ds = \frac{k}{\mu(\gamma - 1)} \frac{dA}{A}$.

where the λ_j are Lagrange multipliers. They are determined by one half of the equations and inserted in the other half so as to obtain:

$$\frac{d\vec{v}_i}{dt} = - \sum_{j=1}^N m_j \left[f_i \frac{P_i}{\rho_i^2} \nabla_i W_{ij}(h_i) + f_j \frac{P_j}{\rho_j^2} \nabla_i W_{ij}(h_j) \right], \quad (3.39)$$

with the f_i defined as:

$$f_i = \left[1 + \frac{h_i}{3\rho_i} \frac{\partial \rho_i}{\partial h_i} \right]^{-1} \quad (3.40)$$

3.2.3 Main differences

Significant differences that can arise in the results of simulations performed either with grid codes or SPH codes concern Galilean invariance and fluid mixing.

Galilean invariance As previously said, grid codes do not ensure Galilean invariance. This can for example have an impact on simulations with high velocity streams of gas accreting onto galaxies, or on simulations of galaxy clusters in which galaxies can have large velocities with respect to the centre of mass of the cluster. The lack of Galilean invariance can change their internal dynamics.

Fluid mixing A problem for SPH in its “normal” version (we used such a version in our simulations) concerns the mixing of different fluids. While grid codes naturally mix fluids at the cell level, SPH consists of particles having their own identity, and an artefact of SPH is a spurious numerical “surface tension” that prevents two fluids from mixing. This is related to the incapacity of SPH to produce entropy when mixing occurs (Springel 2010b), contrarily to mesh codes that generate entropy when averages are made at each time-step.

This fluid mixing is tightly related to two instabilities that are often used as tests for hydrodynamical codes: the Kelvin-Helmoltz instability and the Rayleigh-Taylor instability. The Kelvin-Helmoltz instability occurs when there is a velocity shear at the interface between two different fluids (of different densities, temperature...). The fluids inter-penetrate at the interfaces, creating wave-like spatial patterns. The Rayleigh-Taylor instability occurs when a fluid is accelerated by a less dense fluid, or when it is displaced by the less dense fluid. Significant differences in the evolution of a dense gas cloud moving supersonically relatively to a less dense bulk flow was shown by Agertz et al. (2007) (see Figure 3.6). The Kelvin-Helmoltz instability should gradually destroy the dense cloud by mixing it with the incoming fluid from its surface to its inside parts, but SPH codes do not show this behaviour. The cloud remains while it has long correctly been destroyed in grid codes.

Some attempts have been done so as to solve this problem. For example:

- Price (2008) and Wadsley et al. (2008) suggested to add an artificial heat conduction at contact discontinuities, similarly to the artificial viscosity. The scheme is however

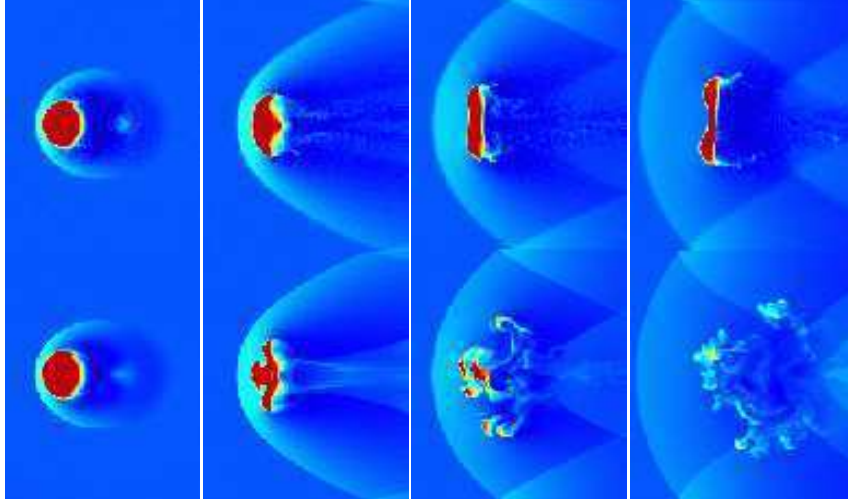


Figure 3.6: Simulations of a dense gas cloud in a supersonic flow. Top row: Simulation with the SPH code Gadget-2. Bottom row: Simulation with the mesh code Enzo. Figure extracted from [Agertz et al. \(2007\)](#).

difficult to tune so that artificial heat conduction occurs only when there should be some mixing.

- A scheme inspired by the density estimates of [Ritchie & Thomas \(2001\)](#) has been proposed by [Read et al. \(2010\)](#). They use a very large number of neighbours and thus a steeper kernel so that the “clumping” instability does not occur. This instability is due to the almost flat kernel shape for small separation of particles, making pressure gradients very small and tending to group particles together artificially. This very large number of neighbours slows down the code.
- [Abel \(2011\)](#) suggested to change the discretisation of the SPH equations in his rpSPH version of Gadget-2, evaluating the pressure forces with respect to the local pressure. The code needs however to be run with a specially fine resolution for energy to be conserved.
- The recent attempt by [Hopkins \(2013\)](#), “pressure-entropy SPH”, a modification of SPH implemented by using the structure of Gadget-2, changes which SPH equations are considered while interestingly retaining the conservative Lagrangian structure. The code has no apparent drawback so far.

In our simulations of disc galaxies, we used SPH in its normal version (with no attempt to lower the artificial surface tension), as the evolution of the discs is not likely to be very sensitive to this problem: in particular, we do not have any hot ambient medium with respect to which dense clumps would have a large velocity difference.

3.2.4 Hybrid codes

Some hybrid codes (“hybrid” is here used for the treatment of gas) try to combine the Lagrangian and Eulerian approaches so as to keep the interesting properties of both methods, particularly the fluid mixing of mesh codes and the Galilean invariance of SPH codes.

The idea of these codes is often to have cells that behave as particles, i.e. that can move along with the fluid. Early attempts of using such methods faced problems related to the distortion of cells (e.g. [Gnedin 1995](#); [Pen 1998](#)). However in the Arepo code ([Springel 2010a](#)), the cells are built by an optimised tessellation at each time-step, so that they have a simple shape, with a limited number of edges, and as “round” as possible. Comparisons between Gadget-2 and Arepo, with the same baryonic physics included, have shown differences in for example the sizes, angular momentum and entropy of gas discs formed in cosmological simulations ([Kereš et al. 2012](#)), shedding some doubt on the validity of normal SPH simulations.

4 Implementing astrophysical processes

We present here how some astrophysical processes, by which we mean processes that are other than gravitational or hydrodynamical, can be implemented in simulations of galaxies. The limited power of calculation prevents us from treating processes in a fully detailed way. Moreover, these processes are still not very well understood, which makes a phenomenological approach necessary. We focus on the implementation in SPH codes, as the code we used for our simulations.

4.1 Star formation

The resolution of simulations at galactic or extra galactic scales is in particular far too insufficient to allow for the study of the formation of individual stars.

Star formation algorithms can involve the creation of new purely stellar particles, or involve hybrid particles (in SPH codes) containing, at least for a while, a part of gas and a part of stellar matter. Star formation is implemented as either continuous (particularly in hybrid schemes), in which case a fraction of gas is necessarily converted into stars at each time-step (depending however potentially on some conditions on gas particles) or stochastic, in which case gas particles have a probability of creating some stellar mass at each time-step, either tied to them in hybrid schemes, or taking the form of a new stellar particle. Continuous schemes have been used mainly in simulations with lower numbers of particles than what is now achievable, their advantage being to reduce the accidental time behaviour of the SFR in stochastic schemes for low number of particles.

There are often some selection criteria for a gas particle (or gas cell in the case of mesh codes) to be allowed to participate in the star formation process. The most common is that the density must be above a certain threshold. This aims at reproducing the (often surface)

density thresholds observed in disc galaxies. Other criteria can be that the particle must be in a converging flow, that it must be Jeans unstable (this criterion is however dependent on the resolution and thus potentially problematic (e.g. [Stinson et al. 2006](#))), or that its temperature must be below a maximum temperature (this is for example used to forbid star formation in dense gas heated by supernovae).

The star formation implementation aims most of the time at reproducing a Schmidt law between the volume densities of stars ρ_* and gas ρ_g ([Schmidt 1959](#)):

$$\frac{d\rho_*}{dt} = C\rho_g^n \quad (3.41)$$

with variations in the chosen index n .

In the hybrid continuous star formation scheme of [Mihos & Hernquist \(1994\)](#), the gas mass M_g contained in a hybrid particle is for example reduced at each time-step by:

$$\frac{\dot{M}_g}{M_g} = -C\rho_g^{1/2} \quad (3.42)$$

so as to recover a Schmidt law with an index $n = \frac{3}{2}$.

In stochastic schemes, gas particles have a probability of converting some of their mass into stellar mass (keeping the stellar part tied to the gas particle in hybrid schemes, or freeing it). A commonly used probability is:

$$p_* = \frac{m_g}{m_*} \left(1 - e^{-c_*\Delta t/t_*}\right) \quad (3.43)$$

where m_g is the gas mass of the particle, m_* the created stellar mass, and t_* is a star formation time that is often taken as proportional to the dynamical time $t_{\text{dyn}} = \sqrt{\frac{3\pi}{32G\rho}}$. c_* is then the star formation efficiency per dynamical time, often set between 0.01 and 0.1 so as to reproduce observations of SFRs. The created stellar mass m_* is not necessarily a constant. [Katz \(1992\)](#) set it to a third of the parent gas particles that had various masses (depending on the mass gained through stellar gas mass loss). m_* is yet often taken as a constant ([Springel & Hernquist 2003](#); [Stinson et al. 2006](#), e.g.) so as to avoid effects of mass segregation.

In hybrid particles schemes, the particles feel and contribute to hydrodynamical forces only through their gas mass. The conversion to a fully stellar particle, that will be only subjected to gravity and no longer to hydrodynamical forces, depends on the algorithm: the particle can be converted into a stellar particle once its stellar mass fraction has reached a threshold (95% of the particle mass in ([Mihos & Hernquist 1994](#))), the rest of the gas being distributed to the neighbours, or once there is enough stellar mass when adding the stellar masses contained in the neighbouring hybrid particles (e.g. [Semelin & Combes 2002](#)). These algorithms have the advantage of keeping the number of particles constant, and therefore not increasing the CPU time needed to evolve the code if several stellar particles are formed out of one gas particle in stochastic spawning schemes. They also tend to be more able to reproduce strong star formation in galaxy mergers ([Mihos & Hernquist 1994](#)). However,

they kinematically couple the stars with gas, while they should evolve separately, gas feeling dissipative hydrodynamical forces and stellar particles behaving in a collisionless manner.

4.2 Stellar feedback

4.2.1 Energy from supernovae explosions

The most commonly implemented form of stellar feedback is the energy effect of core-collapse supernovae (SNII) on the gas. Implementing this feedback was initially partly motivated by its potential destructive effect on low mass galaxies created in a too large number in simulations, and its capacity to remove some low angular momentum material from the central parts of disc galaxies, so as to obtain discs of sizes large enough to be consistent with observations. The effect on star formation is complex: it can limit star formation by preventing it to occur in regions affected by the supernovae heating, but can also trigger it by creating dense shock regions that can be cooled efficiently.

Core-collapse supernovae are massive stars $> 8 M_{\odot}$ that explode after about 10 Myr. The exact fraction of energy that is given to the ISM rather than being radiated away is not well determined from observations and is a parameter that is often set so as to reproduce observations concerning the SFR.

The feedback can be implemented in a thermal way, by giving internal energy to gas particles, or in a kinetic way, by giving them velocity kicks.

If the energy is added thermally, as it is likely to be given to gas particles in dense regions, close to the star formation region, the energy will be radiated away quickly by the important cooling of the gas, making the feedback inefficient. What is often done is forbidding particles to cool for some time, so as to effectively prevent further star formation in heated gas and to give the particles time to transfer their internal energy into kinetic energy to their neighbours (e.g. [Gerritsen 1997](#); [Thacker & Couchman 2000](#)). The stopping can be ensured for a given amount of time, often $\sim 10 - 30$ Myr, or can last for a time that depends on the local properties of the gas and of a model of the SNII explosion evolution, as in the blastwave recipe ([McKee & Ostriker 1977](#)), as tested by [Stinson et al. \(2006\)](#).

The energy can also be added in the form of velocity kicks. [Navarro & White \(1993\)](#) try two implementations: the “energy” and “momentum” schemes:

- In the “energy” implementation, a velocity kick is added to neighbouring gas of a new stellar particle so that the total energy is properly augmented by the given supernovae energy. However, the velocities of affected gas particles point necessarily away from the stellar particle, which changes significantly the velocity distribution, reversing necessarily a converging flow into a diverging one (at least just after the energy injection).
- In the “momentum” implementation, the feedback energy E_{feedback_i} attributed to a gas particle i of mass m_i is transformed into a velocity kick \mathbf{v}_i radially away from the stellar particle, with a value determined by $E_{\text{feedback}_i} = \frac{1}{2}m_i v_i^2$. This kick velocity is simply

added to the velocity of the gas particle, and as the vectors have no reason of being co-linear, the total feedback energy will not be exactly added.

As particles affected by kinetic feedback are often in dense regions, they are likely to be quickly braked by the artificial viscosity of SPH. Some attempts of decoupling them from hydrodynamics for a while (similarly to the cooling shutting-off for thermal feedback) have also been made (e.g. [Springel & Hernquist 2003](#)).

Whether the energy is added in a thermal or kinetic way or both, the feedback energy from new stellar particles can be released in one step or gradually, injecting the total desired feedback energy in several time-steps.

Explosions of SNIa can also be included (e.g. [Stinson et al. 2006](#)), considering a delay between the formation of a stellar particle and the explosions of SNIa, trying to mimic the time needed for conversion into SNIa.

Most of our simulations have been run with kinetic feedback in its “momentum” version. We have not included feedback from SNIa so far.

4.2.2 Stellar mass loss and metal enrichment

Stars of various masses lose mass, in explosions for supernovae, or in continuous winds for low mass stars (before they become white dwarves). Recycled gas can help sustain star formation by providing an internal “gas source” in galaxies, and impacts the metallicity of the interstellar gas as the heavy elements content of the recycled gas has been increased by its time as a part of a star. This increase in metallicity is important to determine precisely the cooling undergone by the gas.

The most commonly stellar mass and metallicity feedback that is taken into account in simulations is from SNII. Low mass stars also lose mass in a gradual manner during their life-time. This mass can be given to the neighbouring gas of stellar particle time-step after time-step ([Jungwiert et al. 2001](#)). As metals production depends on the age of stars, some stellar population models are used to determine what mass of which heavy elements are returned to the interstellar gas at a given time (e.g. [Wiersma et al. 2009](#); [Revaz et al. 2009a](#)).

4.2.3 Radiation pressure

Another feedback mechanism is the pressure energetic UV photons emitted by young massive stars exert on dust grains that can transfer momentum to the gas. Some codes take this pressure into account, which strongly enhance the feedback related to star formation (e.g. [Hopkins et al. 2011](#); [Agertz et al. 2012](#)).

4.3 Cooling and heating of the ISM

4.3.1 Cooling and heating from microscopic processes

Cooling and heating are encapsulated in cooling functions, representing the volume rate of energy loss or gained by the gas depending on its chemical composition and its temperature. Tabulated cooling rates are often used: they are computed using theoretical computations of different microscopic processes as the ones mentioned in 1.3 of Chapter 2. Some codes can use detailed cooling rates that depend on the exact composition of the gas, for example with the package CLOUDY (Ferland et al. 1998).

It is also possible to use an effective equation of state that directly sets the temperature for a given density, based on the equilibrium temperature gas should have due to the considered composition and background radiation, and the corresponding heating and cooling processes (Teyssier et al. 2010; Bounaud et al. 2010). In certain conditions of strong shocks, such a scheme may however not treat accurately the thermal evolution of the gas.

4.4 Molecular hydrogen formation and destruction

Molecular hydrogen formation and destruction are tracked in some simulations (e.g. Gnedin et al. 2009; Dobbs & Bonnell 2008; Christensen et al. 2012b).

The formation and destruction rates linked to respectively dust and FUV radiation and cosmic rays can be included in an equation for the evolution of the number density of H_2 molecules as in Bergin et al. (2004):

$$\frac{dn_{H_2}}{dt} = R_{gr}n(H)n - [\zeta_{cr} + \zeta_{diss}(N(H_2), A_V)]n_{H_2} \quad (3.44)$$

where $n(H)$ is the number density of H atoms, n is the total number density of hydrogen nuclei, and R_{gr} depends on the temperature and the efficiency of H_2 formation on grains. ζ_{cr} and $\zeta_{diss}(0)$ are the dissociation rates dues to respectively cosmic rays and FUV photons, $N(H_2)$ is the H_2 column density and A_V the visual extinction. The main dissociation process is photodissociation (except in regions where A_V is very large). Its expression is often taken from Draine & Bertoldi (1996) as being:

$$\zeta_{diss}(N(H_2), A_V) = f_{shield}(N_{H_2})f_{dust}\zeta_{diss}(0) \quad (3.45)$$

where f_{shield} accounts for H_2 self-shielding, f_{dust} for dust absorption, and ζ_{diss} is the photodissociation rate for unshielded H_2 . f_{shield} is given by Draine & Bertoldi (1996) as a function of $N(H_2)$. Some approximations are used to determine this column density that plays a major role in the shielding. Wolcott-Green et al. (2011) detail a number of ways it can be estimated.

Other schemes, as the one we used and will detail in the next chapter, do not follow the time evolution of H_2 , but rather determine what equilibrium fraction it should have depending on its physical parameters.

4.5 Importance of resolution

The effect of baryonic physics recipes can be sensitive to resolution. An increased resolution (spatial and/or mass) tends to increase the maximum densities reached by the gas, which, as the cooling efficiency is proportional to the density (squared), increases the cooling of the gas and its ability to form stars. Moreover, in star formation recipes whose efficiency increases with density, as for most of the used recipes, an increased resolution will lead to more star formation. This can however be counterbalanced by the increased energetic stellar feedback. This feedback, depending on its exact implementation, can itself strongly depend on the adopted resolution.

Most of the time, parameters used in recipes are thus tuned depending on the resolution, so as to recover observed results, like an average SFR. The threshold density often considered in star formation is for example increased if the resolution is increased.

A special concern is to resolve the Jeans length/mass, that determine the scale at which a gas cloud becomes gravitationally unstable. [Bate & Burkert \(1997\)](#) show that for SPH simulations, a poor resolution of this length/mass can lead to numerical artefacts that depend closely of the relative values of the gravitational softening ϵ and hydrodynamical smoothing length h . For simulations with a fixed ϵ , h is often allowed to vary and to be potentially lower than ϵ , especially in schemes likes the one used in Gadget-2, in which the mass in a smoothing kernel volume is required to be constant. The smaller ϵ is, the higher gravitational forces can be at small distances, while the smaller h can be, the higher pressure forces can be (by means of higher pressure gradients). If the Jeans length is not well resolved, $\epsilon > h$ could lead to artificially pressure supported gas clouds, while the contrary could lead to artificial fragmentation. For Gadget-2, using a variable softening length ϵ –which would allow to have an adaptive resolution for both hydrodynamical and gravitational forces and to keep $\epsilon = h$ – requires a complex modification of the code so as to preserve the conservation of energy ([Iannuzzi & Dolag 2011](#)). [Schaye & Dalla Vecchia \(2008\)](#) use an effective equation of state at high densities that makes the Jeans mass independent of density, while [Hopkins et al. \(2011\)](#) take a density-dependent pressure floor to ensure the Jeans length is resolved, and [Bournaud et al. \(2010\)](#) use a temperature floor at high densities.

Chapter 4

Introducing baryonic physics in Gadget-2

We took Gadget-2 ([Springel 2005](#)) used as a TreeSPH code to perform our simulations of disc galaxies. In this chapter, we describe what we modified or added to the public version of Gadget-2 that contains only the computation of gravitational and hydrodynamical forces. After some comments about parallelisation and time-steps, we detail how the evolution of particles is exactly carried out, and then precise our treatment of cooling, computation of the molecular hydrogen fraction, stellar formation and feedback.

1 Some specific features of Gadget-2

1.1 Parallelisation

Gadget-2 is an MPI code, which means that the code is run on multiple cores (“tasks”) –each task dealing with a certain number of particles– that exchange messages so as to use the required information from other tasks to advance the code.

Space is discretised using a Peano-Hilbert curve, a space-filling curve (see Figure 4.1), and a particle is associated to a close point of this curve. This space-filling curve interestingly preserves locality: points that are close in 3D space are also close along the curve. Spatial domains are obtained by splitting this curve into as many parts as tasks, and in a way that optimises the work-load balance. Basically, clustered regions for which the force computation will be long (compared to diffuse regions) are split in a finer manner. Another interest of this curve is that its splitting can be easily done so that the resulting domains are the same domains that are obtained by the simple recursive oct-tree spatial decomposition that is used ([Warren & Salmon 1995](#)). A given task will thus have particles that correspond to nodes of the gravitational tree.

Each task builds a top-level tree containing the nodes at higher levels than the one it

contains. If a particle needs information contained uniquely on another task, it is exported to the other task, the desired computation is performed locally on this other task using the local data (this can be a gravitational computation or a density or hydrodynamical force computation), and the particle is imported back to its task.

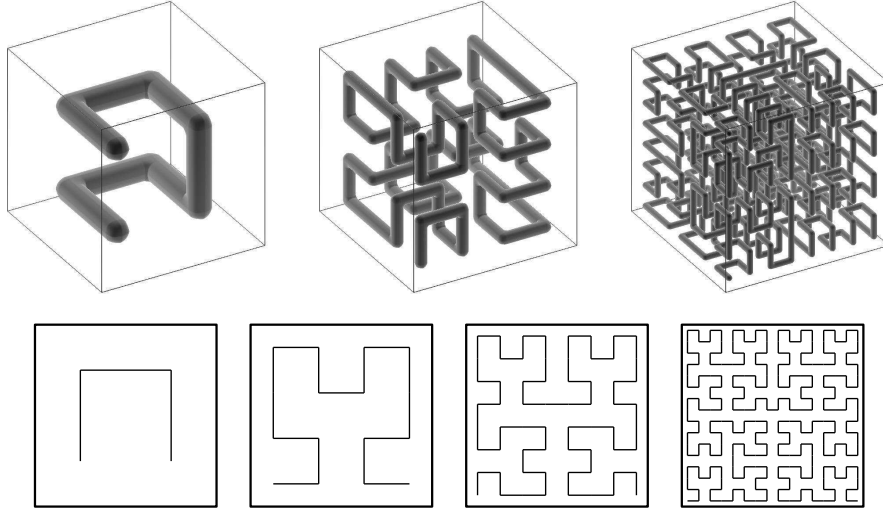


Figure 4.1: Peano-Hilbert curve in 3D (top row) and 2D (bottom row). Figure from [Springel \(2005\)](#).

1.2 Individual time-steps

The code uses individual time-steps so that the computing time is optimised, focusing on the updating of clustered regions without wasting time with low acceleration/diffuse regions that can be treated with longer time-steps. Time-steps are determined using a criterion on softening length ϵ_i and acceleration a_i of a particle i :

$$\Delta t_i = \sqrt{\frac{2\eta\epsilon}{|a_i|}} \quad (4.1)$$

where η is an accuracy parameter we kept at 0.025 as in the default Gadget-2 parametrisation. [Power et al. \(2003\)](#) showed this choice of time-step gives robust results. For gas particles, the time-step is the minimum of Δt_i and an additional Courant criterion:

$$\Delta t_i^{\text{Courant}} = C \frac{h_i}{\max_j v_{\text{sig } ij}} \quad (4.2)$$

where C is another accuracy parameter and h_i is the smoothing length of the particle i , $v_{\text{sig } ij}$ is the signal velocity between i and a neighbour j .

In the version of the time-integration method we used for our simulations, particles are synchronised: they all have time-steps that are equal to the smaller one multiplied by a power of two, and can increase their time-step only if it synchronises them with the particles

that have the desired larger time-step (this makes them have to wait to increase their time-step). This way, the kick operations involve a larger fraction of particles each time they happen, which optimises the computation time. This synchronisation scheme is represented on Figure 4.2.

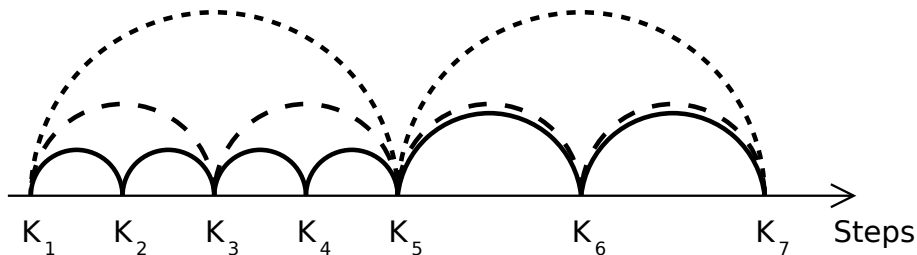


Figure 4.2: Schematic view of individual time-steps. 3 particles are represented by the 3 lines (solid, dashed and dotted). The K_n are kick operations. If the particle coded by a solid line wants to increase its time-step to the next larger time-step at K_4 , it has to wait until K_5 so as to be synchronised with particles that have this larger time-step.

2 Code steps and implemented additions and changes

We detail here the steps of the computation and the additions we made. A graph representing functions and calls is shown in Appendix B.

2.1 Initialisation

The code first performs some initialisation steps. The `main` function calls `begrun` that itself calls `init`. The two latter functions and their subfunctions:

- Read the parameters file and initial conditions file(s), set the internal units and convert the input into internal units if needed.
- Perform an initial domain decomposition.
- Build an initial tree.
- Set up the smoothing lengths of gas particles.
- Read the cooling rates data at various temperatures we stored in a couple of files and initialise interpolation functions.

2.2 Main loop

The `main` function then calls `run` that contains the iteration on time-steps.

2.2.1 Drift

The time integration is done with individual time-steps, which means that the particles with long time-steps have a drift operation done in a fractional manner, over several successive iterations, without being kicked, so that the particles that are kicked in-between have accelerations computed with all the drifted positions.

Next Kick time determination The next time $t_{\text{next kick}}$ at which some particles will be kicked is first determined. $t_{\text{next kick}}$ is the smallest ending point of time-steps.

Drift operation The code then drifts all the particles to this time, i.e. updates their position, and, for gas particles, also their predicted velocity, density, smoothing length and pressure. At start up this drift is not applied. The code starts (and ends) with a Kick operation on half a time-step of each particle.

With t_{curr} the current code time and $\Delta t_{\text{drift}} = t_{\text{next kick}} - t_{\text{curr}}$, for a particle i that has started its time-step of length Δt_i at t_{beg_i} and will finish it at time t_{end_i} ($t_{\text{beg}_i} \leq t_{\text{curr}}$ and $t_{\text{end}_i} = t_{\text{beg}_i} + \Delta t_i \geq t_{\text{next kick}}$):

- The position \mathbf{x}_i is updated by:

$$\mathbf{x}_i^{t_{\text{next kick}}} = \mathbf{x}_i^{t_{\text{curr}}} + \mathbf{v}_i^{t_{\text{beg}_i}} + \frac{\Delta t_i}{2} \Delta t_{\text{drift}} \quad (4.3)$$

- The predicted velocity \mathbf{vp}_i of a gas particle (used to compute the hydrodynamical forces) is obtained by:

$$\mathbf{vp}_i^{t_{\text{next kick}}} = \mathbf{vp}_i^{t_{\text{curr}}} + \mathbf{a}_i^{t_{\text{beg}_i}} \Delta t_{\text{drift}} \quad (4.4)$$

- The density ρ_i is updated by:

$$\rho_i^{t_{\text{next kick}}} = \rho_i^{t_{\text{curr}}} e^{-\nabla \cdot \mathbf{v}^{t_{\text{beg}_i}} \Delta t_{\text{drift}}} \quad (4.5)$$

(This comes from the continuity equation written in the Lagrangian form.)

- The smoothing length h_i is updated accordingly by:

$$h_i^{t_{\text{next kick}}} = h_i^{t_{\text{curr}}} e^{\frac{1}{3} \nabla \cdot \mathbf{v}^{t_{\text{beg}_i}} \Delta t_{\text{drift}}} \quad (4.6)$$

so as to conserve a constant mass in a smoothing volume.

- The pressure P_i is updated by:

$$P_i^{t_{\text{next kick}}} = \left[A_i \frac{t_{\text{beg}_i} + t_{\text{end}_i}}{2} + \frac{dA^{t_{\text{beg}_i}}}{dt} \left(t_{\text{next kick}} - \frac{t_{\text{beg}_i} + t_{\text{end}_i}}{2} \right) \right] \rho_i^{\gamma_{t_{\text{next kick}}}} \quad (4.7)$$

The entropies, as for velocities, are indeed known at mid time-steps. The time difference on which this last update is carried out can thus logically be negative in case the ending point of the drift is anterior to the mid-point of the particle time-step.

The soon to be kicked particles are named “active particles”. The current code time t_{curr} is updated to $t_{\text{next kick}}$.

The “snapshot” files are written at pre-set times or at constant time interval. To study our simulations, we added the output of some useful data blocks in the snapshot files amongst which the date of creation of stellar particles and the H_2 fraction in gas particles.

As the snapshot writing times do not necessarily coincide with $t_{\text{next kick}}$, the code may drift particles in two steps, one to reach the snapshot writing time, and one to reach $t_{\text{next kick}}$. For our disc simulations, we added the writing of the spatial Fourier components of the disc density at constant smaller time-steps than our snapshot writing time-steps (the time-steps of this analysis had to be constant so as to perform a time Fourier transform of them in a post-run analysis). We thus added a potential additional splitting of the drift to perform the Fourier analysis and write it in an output file.

The code then writes timing diagnostics at the current time t_{curr} .

2.2.2 Star formation

The function `star_formation` forms stellar particles out of active gas particles. The star formation is stochastic: if a particle satisfies conditions on its density, velocity divergence and temperature, a random number r is drawn between 0 and 1 and the particle undergoes star formation if $r \leq p$, with p the probability used to form stars. We use the same function for generation of random numbers as the one used elsewhere in the code, this function being designed to be independent of the number of tasks.

A new stellar particle is given the position and velocity of the parent gas particle, as well as its density and smoothing length that will both be used for stellar feedback. It is given the same Tree “father” as its parent gas particle so that if the Tree is not re-built, it will be properly dynamically kicked.

The new particles are stored at the end of the already existing particles on each task, and they are given a unique identifier (after communication of the number of new stellar particles on each task).

If some gas particles are completely converted into stellar particles, we added a function `rearrange_particle_sequence` that will be called before the next domain decomposition, because such a decomposition requires the particles to be ordered in a continuous block of gas particles first and then other particles. The functioning of this rearrangement is shown on Figure 4.3.

2.2.3 Acceleration computation

The code then computes the accelerations, and the entropy gain generated by viscosity using the updated positions of the particles. Newly formed stellar particles are not involved in SPH computations, their acceleration is purely gravitational.

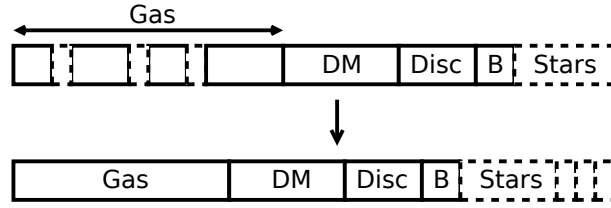


Figure 4.3: Schematic rearrangement of particles in memory when some gas particles are completely converted into new stellar particles. Particles are stored according to their type: gas, dark matter, disc, bulge, and new stars (the stellar particles created during a simulation and named "stars" on the figure).

A domain decomposition is made if needed, i.e. if a criterion of frequency of domain decomposition and tree updates is met. If a domain decomposition is performed, the tree will be updated.

The accelerations of the active particles are then computed:

- The gravitational acceleration is computed by either building a new tree if a new domain decomposition has been made, or by using the dynamically updated tree computed in the last kick operation. The new stellar particles are active and have thus their gravitational acceleration computed.
- The density and smoothing length are computed with an iteration that aims at making the mass in a softening kernel volume constant. Pressure of gas particles is computed, and so are the hydrodynamical force and entropy change. We have added the computation of the gradient of the density, needed for the molecular hydrogen fraction, in the function that computes the hydrodynamical forces.

2.2.4 SNII feedback computation

The function `compute_snfeedback` distributes feedback energy from SNII to the neighbours of new stellar particles. So as to always input the same energy, we compute a smoothing length for new stellar particles, without taking a possible remnant gas particle into account (the latter restriction is just for simplicity, as we mainly used kinetic feedback with velocity kicks given along the line joining a new stellar particle and a neighbouring gas particle). This way, the weighting by the smoothing kernel is properly normalised. The velocity kick will be added during the kick operation.

2.2.5 Kick, H_2 fraction computation and cooling

New time-steps computation After some energy statistics performed with a pre-set time interval, the code determines the new time-steps for the particles whose current time-step ends at $t_{\text{next kick}}$, using their newly computed accelerations and smoothing lengths and signal velocities for gas particles.

Taking into account the velocity kick from SNII feedback without slowing down the code is tricky because the signal velocity has been computed in the hydrodynamical forces loop. Updating it properly would require another SPH loop on gas particles. We tried a very simple additional time limiter for particles that are affected by feedback. In the case where the feedback kick is higher than the maximal signal velocity, we replace the maximal signal velocity by the feedback kick in the Courant time limiter of 4.2. This way, a large feedback kick can reduce the time-step of a gas particle.

Kick operation The Kick operation for those particles is then performed.

The velocities of particles taking part in the Kick are updated by:

$$\mathbf{v}_i^{t_{\text{curr}} + \frac{\Delta t_{\text{new}_i}}{2}} = \mathbf{v}_i^{t_{\text{curr}} - \frac{\Delta t_{\text{old}_i}}{2}} + \mathbf{a}_i^{t_{\text{curr}}} \frac{\Delta t_{\text{new}_i} + \Delta t_{\text{old}_i}}{2} \quad (4.8)$$

with Δt_{old_i} the old time-step and Δt_{new_i} the newly determined time-step of the particle i .

In the case where we use kinetic supernova feedback, we add the velocity due to the feedback to the affected particles.

The predicted velocities of gas particles are updated using these newly computed velocities:

$$\mathbf{vp}_i^{t_{\text{curr}}} = \mathbf{v}_i^{t_{\text{curr}} + \frac{\Delta t_{\text{new}_i}}{2}} - \mathbf{a}_i^{t_{\text{curr}}} \frac{\Delta t_{\text{new}_i}}{2} \quad (4.9)$$

H₂ fraction computation We compute the H₂ fraction of gas particles with the function `make_h2`. This computation could be done before the Kick operation because the Kick has no effect on it. As it must be done after the density gradient has been computed, we inserted it in this loop on particles for commodity. This is done before the cooling, so that the H₂ fraction has been properly updated for the computation of the cooling rates.

Entropy update, cooling The code then updates the entropy A of gas particles. This is done at this point of the code, with the same newly obtained time-step as the one with which the velocity is updated. This way, in the absence of other cooling or heating processes than the heating related to artificial viscosity, the change in internal energy exactly balances the corresponding change in kinetic energy. The update is done by:

$$A_i^{t_{\text{curr}} + \frac{\Delta t_{\text{new}_i}}{2}} = A_i^{t_{\text{curr}} - \frac{\Delta t_{\text{old}_i}}{2}} + \frac{dA_i}{dt}^{t_{\text{curr}}} \frac{\Delta t_{\text{new}_i} + \Delta t_{\text{old}_i}}{2} \quad (4.10)$$

If we use the cooling we have added, we update the entropy in a modified manner. The function `cool_evaluate` evaluates the entropy loss due to cooling by the atom/ion/molecule processes being considered. It computes the cooling rate according to the temperature, molecular content and metallicity of a gas particle. The cooling rates are obtained through interpolation using lookup tables, analytic fits or numerical solution of equations for low temperature metal cooling.

We use a semi-implicit scheme in case the total entropy change –summing the gain from viscosity heating and the loss from the added cooling– exceeds a tenth of the entropy (which amounts to when the cooling time is less than ten times the time-step). In this case, the new entropy is obtained by an iterative scheme.

3 Radiative cooling

We first present some basics of line-cooling we use to compute cooling functions of metals, H₂ and HD below 10⁴ K, and then present these cooling functions as well as the cooling used above 10⁴ K.

3.1 Line cooling

Species with several energy levels can change level due to collisions or radiation. Collisions with species of the same medium, whether they are elastic or not, do not make the gas lose any energy globally. Radiation, in cases in which the medium can be considered as optically thin, can however remove some energy from the gas by escaping. We do not consider stimulated emission or absorption.

The volume cooling rate due to a system of N levels of populations $n_1 \dots n_N$ (number densities in cm⁻³ of sum n_{tot}) and energies $E_1 \dots E_N$ is the rate of escaping radiation due to all the transitions (all the lines being considered as optically thin here):

$$\Lambda = \sum_{1 \leq i < j \leq N} n_j A_{ji} (E_j - E_i) \quad (4.11)$$

where A_{ji} is the probability of spontaneous de-excitation from level j to level i per unit time (in s⁻¹).

As species can be de-excited by radiation, it is not always possible to approximate the populations of energy levels using their Boltzmann value, as they would have in the case of Local Thermal Equilibrium (LTE):

$$n_i^B = n_{\text{tot}} \frac{g_i e^{-\frac{E_i}{kT}}}{Z} \quad (4.12)$$

where g_i is the multiplicity of level i and Z is the partition function:

$$Z = \sum_{i=1}^N g_i e^{-\frac{E_i}{kT}} \quad (4.13)$$

For low densities of the colliding species, the high energy levels are indeed not as occupied, as their depopulation by spontaneous emission of radiation is of the same order or greater than their depopulation by collisions. Populations of each energy level have to be computed.

The principle of detailed balancing can be used to determine the populations. This principle states that the number of transitions to a given energy level is equal to the number of transitions from that level to others per unit time and volume, i.e. the population of an energy level equals its depopulation by unit time and volume. For a level i , this detailed balance can be written as:

$$n_i \sum_j P_{i \rightarrow j} = \sum_j n_j P_{j \rightarrow i} \text{ for } i \neq j \quad (4.14)$$

where n_i is the number density of particles in level i , and $P_{i \rightarrow j}$ is the probability of transition from level i to level j by unit time (in s^{-1}). This probability can be the Einstein coefficient for spontaneous emission A or the probability of collisional transitions from level i to j . In the case of collisions with a species X (hydrogen atoms or electrons for example) this probability is:

$$P_{i \rightarrow j}^{\text{coll}} = n_X \gamma_{ij}^X \equiv n_X \langle v \sigma_{ij}^X \rangle = n_X \int_0^\infty v \sigma_{ij}^X f(v) d^3v \quad (4.15)$$

where γ_{ij}^X is a collision coefficient (in $\text{cm}^3 \text{s}^{-1}$), σ_{ij}^X is the corresponding collision cross-section (in cm^2) and f is the distribution function for velocity v .

Two-level species The case of a two-level species X is useful to exhibit deviations from the Boltzmann distribution. If X , with energy levels 1 and 2 of populations n_1 (lower level) and n_2 (upper level), experiences collisions with a species Y that makes it change of energy level with rates γ_{12}^Y and γ_{21}^Y (see Figure 4.4), the detailed balance principle can be written as:

$$\left. \frac{dn_2}{dt} \right|_{\text{coll-exc}} - \left. \frac{dn_2}{dt} \right|_{\text{coll-deexc}} - A_{21} n_2 = 0 \quad (4.16)$$

$$\gamma_{12}^Y n_1 n_Y - \gamma_{21}^Y n_2 n_Y - A_{21} n_2 = 0 \quad (4.17)$$

where A_{21} is the Einstein coefficient for spontaneous emission. As $\gamma_{12}^Y = \gamma_{21}^Y \frac{g_2}{g_1} e^{-\frac{E_2 - E_1}{kT}}$ (using the detailed balance principle in the absence of radiation), the equilibrium ratio of populations is:

$$\frac{n_2}{n_1} = \frac{g_2}{g_1} \frac{e^{-(E_2 - E_1)/kT}}{1 + \frac{A_{21}}{\gamma_{21}^Y n_Y}} \quad (4.18)$$

A critical density for the species Y can thus be defined as:

$$n_{\text{crit}} = \frac{A_{21}}{\gamma_{21}^Y} \quad (4.19)$$

If $n_Y \gg n_{\text{crit}}$, the populations ratio reduces to the Boltzmann ratio, while if $n_Y \lesssim n_{\text{crit}}$, the depopulation of level 2 will be due mainly to radiation, leading to a reduced higher level population.

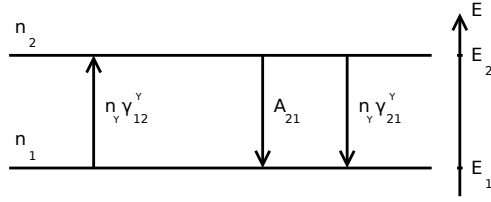


Figure 4.4: Energy levels with probabilities of excitation and de-excitation by collisions or spontaneous radiation.

3.2 Cooling by metals under 10^4 K

Following [Maio et al. \(2007\)](#), we compute cooling functions of a few metals below 10^4 K: ionised carbon CII, neutral oxygen OI, ionised silicium SiII and ionised iron FeII. These are the most abundant heavy atoms released by stars in the ISM and thus are the main ingredients for cooling. SNIIs expel mostly oxygen and carbon, and supernovae of type Ia expel silicon and iron. Carbon, silicon and iron are assumed to be completely ionised as a UV background below 13.6 eV escapes absorption from neutral hydrogen and can ionize these metals that have a first ionisation potential below 13.6 eV. Oxygen is mainly neutral as its first ionisation energy is at 13.62 eV.

For each species, we solve a system of equations including equations equalising the de-populations and populations of energy levels, and the equation accounting for the conservation of the number of particles. Collisions with hydrogen atoms and electrons are considered. The collision rates and Einstein coefficients are taken from [Hollenbach & McKee \(1989\)](#) and [Santoro & Shull \(2006\)](#).

We write the systems of equations and solve them either analytically for CII and SiII, or numerically for OI and FeII.

Carbon and silicium The CII system is modelled as a two-level system taking into account the fine structure transition between two states, so we have:

$$\begin{cases} n_1 + n_2 = n_{\text{tot}} \\ -n_1 n_H \gamma_{12}^H - n_1 n_e \gamma_{12}^e + n_2 n_H \gamma_{21}^H + n_2 n_e \gamma_{21}^e + n_2 A_{21} = 0 \end{cases} \quad (4.20)$$

The SiII system also consists of two levels, so the equation system is the same as for CII (with the coefficients specific to silicium).

Oxygen and iron OI and FeII are modelled with 5 energy levels. We write the equation systems with the relevant transition coefficients and solve them numerically to compute the cooling functions.

We choose the same abundances as in [Sutherland & Dopita \(1993\)](#) (solar abundances and primordial ratios) for the metals we consider here. As they did, we assume that the

abundances are solar for a metallicity $Z = [\text{Fe}/\text{H}] = \log_{10} \frac{n_{\text{Fe}}}{n_{\text{H}}} - \log_{10} \frac{n_{\text{Fe}}}{n_{\text{H}}}|_{\odot}$ from 0 to 0.5, primordial for $Z \leq -1$, and an interpolation between primordial and solar values for $-1 \leq Z \leq 0$. The ratios are listed in Table 3.2.

	Fe	O	Si	C
Solar $\log_{10} \frac{n}{n_{\text{H}}}$	-4.33	-3.07	-4.45	-3.44
Primordial $\log_{10} \frac{n}{n_{\text{H}}}$	-4.33	-2.57	-4.05	-3.44

We take a fixed low electronic fraction of ($\frac{n_{e^-}}{n_{\text{H}}} = 10^{-5}$), assuming the cold gas is quasi neutral.

The cooling functions of carbon, iron and silicium start saturating for densities of $10^4 - 10^5 \text{cm}^{-3}$, which is of the order of magnitude of the highest densities we can have, so the volume cooling rate is proportional to the density, not to its square. We represent on Figure 4.5 the individual cooling rates for solar abundances and $n_{\text{H}} = 1 \text{cm}^{-3}$, and on Figure 4.6 the volume cooling rate for various densities for a solar metallicity. We solve the equations in the code directly. We note that as we have all the data to solve for populations in different regimes, another possibility would be to write the cooling functions for individual metals as an interpolation between the high density LTE regime and the low density regime (in the spirit of what is done for the H_2 cooling in the next section) for which we can obtain analytic fits.

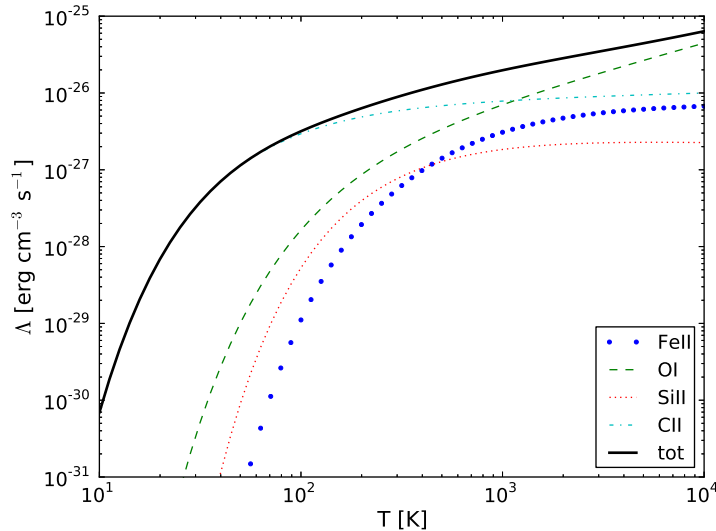


Figure 4.5: Volume cooling rates of metals for solar abundances, $n_{\text{H}} = 1 \text{cm}^{-3}$ and $\frac{n_e}{n_{\text{H}}} = 10^{-5}$

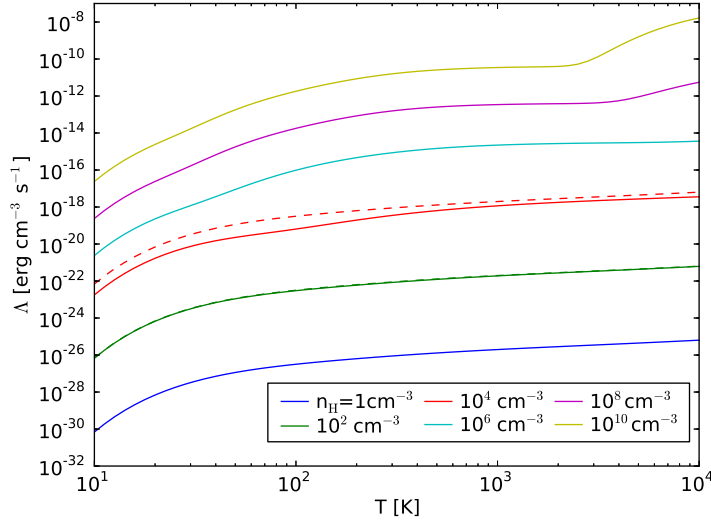


Figure 4.6: Volume cooling rate for a solar metallicity and increasing densities. The dashed lines are $n_{\text{H}}^2 \Lambda(n_{\text{H}} = 1 \text{ cm}^{-3})$ for $n_{\text{H}} = 10^2 \text{ cm}^{-3}$ and $n_{\text{H}} = 10^4 \text{ cm}^{-3}$ (in the colour corresponding to the cooling function obtained from the resolution of levels populations). This approximation starts breaking down at $n_{\text{H}} = 10^4 \text{ cm}^{-3}$

3.3 Cooling of H, He and metals above 10^4 K

We use the cooling functions computed by [Sutherland & Dopita \(1993\)](#) for an optically thin plasma in collisional ionisation equilibrium (CIE). These cooling functions include cooling due to H, He and metals, for different metallicities. Different cooling processes (collisional excitation, recombination and ionisation, free-free radiation or bremsstrahlung), and heating processes (photoionisation radiation and Compton heating) are included in the computation of the cooling functions.

The functions taken directly from the tables of [Sutherland & Dopita \(1993\)](#) are plotted on Figure 4.7. For intermediate metallicities, we used an interpolation on metallicity.

The full cooling functions for a gas with hydrogen only in atomic form is obtained by combining the cooling functions with the same metal abundances to get cooling functions from 10 K to $10^{8.5}$ K and are shown on Figure 4.8 for $n_{\text{H}} = 1 \text{ cm}^{-3}$.

3.4 Cooling by molecular hydrogen

To compute the cooling due to H_2 , we use the approach of [Glover & Abel \(2008\)](#), reminiscent of [Hollenbach & McKee \(1979\)](#). The cooling function is written as an interpolation between the LTE cooling function and the function for low densities.

$$\Lambda_{\text{H}_2} = n_{\text{H}_2} \frac{\Lambda_{\text{H}_2, \text{LTE}}}{1 + \frac{\Lambda_{\text{H}_2, \text{LTE}}}{\Lambda_{n \rightarrow 0}}} \quad (4.21)$$

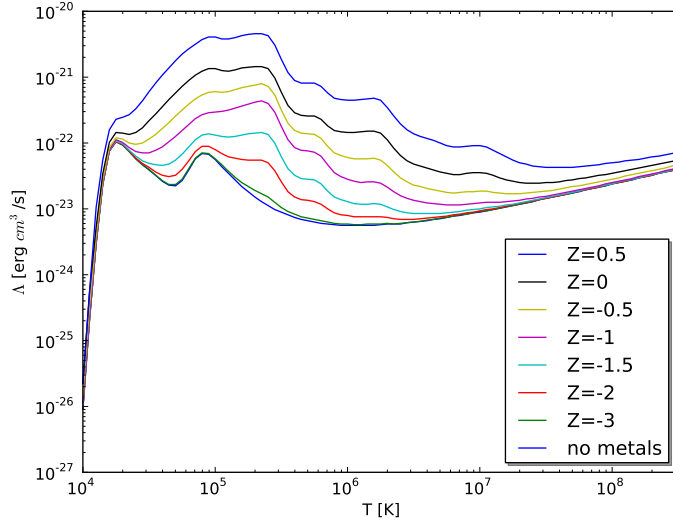


Figure 4.7: Volume cooling rates normalised by $n_{\text{H},0}^2$ with $n_{\text{H},0} = 1\text{cm}^{-3}$ of Sutherland & Dopita (1993) for different metallicities $Z = [\text{Fe}]/[\text{H}]$

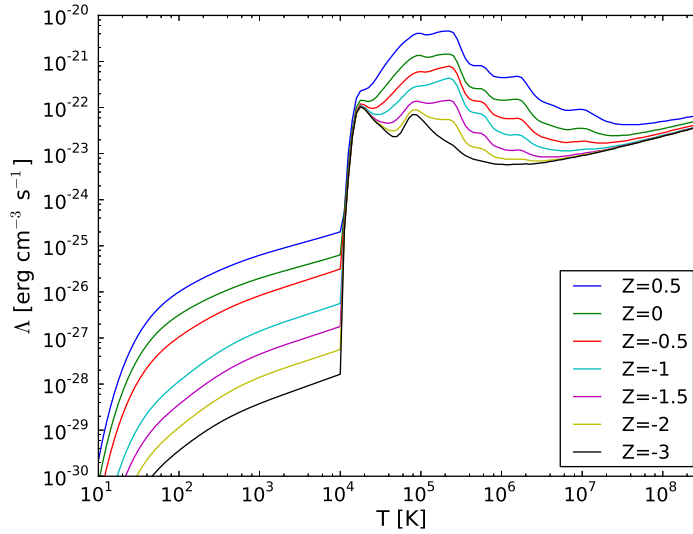


Figure 4.8: Full cooling curves of metals at different metallicities for $n_{\text{H}}=1\text{cm}^{-3}$.

with $\Lambda_{\text{H}_2,\text{LTE}}$ the LTE cooling rate per H_2 molecule in erg s^{-1} and:

$$\Lambda_{\text{H}_2,n\rightarrow 0} = \sum_k \Lambda_{\text{H}_2,k} n_k \quad (4.22)$$

where $\Lambda_{\text{H}_2,k}$ is the cooling rate in $\text{erg cm}^3 \text{s}^{-1}$ (normalised by $n_{\text{H},0}^2$ with $n_{\text{H},0} = 1\text{cm}^{-3}$) due to collisions of H_2 with the species k and n_k is the number density of the species k . For low densities, this reduces to $\Lambda_{n\rightarrow 0}$ and for high densities, to $\Lambda_{\text{H}_2,\text{LTE}}$.

As the H_2 molecule is symmetric, the allowed transitions are quadrupole ones with $\Delta J =$

0 ± 2 . The LTE cooling rate per molecule is:

$$\Lambda_{\text{H}_2, \text{LTE}} = \sum_{i < j, \Delta J = 0, \pm 2} f_j A_{ji} (E_j - E_i) \quad (4.23)$$

where f_j is the fraction of molecules in the energy level j :

$$f_j = \frac{g_j e^{-\frac{E_j - E_0}{kT}}}{Z} \quad (4.24)$$

with E_0 the energy of the non-degenerate ground state, and g_j the multiplicity of level j . There is a rotational degeneracy $(2J + 1)$, with J the rotation quantum number of the energy level in question, and another factor, $2S + 1$, due to nuclear spins that can be parallel (“ortho-hydrogen”, $S = 1$) or anti-parallel (“para-hydrogen”, $S = 0$). This factor is 3 for ortho-hydrogen, and to 1 for para-hydrogen. We calculated the LTE cooling rate per molecule using energies and Einstein coefficients for the allowed transitions from the CLOUDY package (Ferland et al. 1998).

The LTE approximation is correct only for high densities that are not reached in our simulations. We used the a_i coefficients of Glover & Abel (2008) for the approximation of the cooling function due to collisions with the species X for low densities:

$$\log \Lambda_{\text{H}_2, X} = \sum_i a_i (\log T_3)^i \quad (4.25)$$

where $T_3 = T/1000$ and $\Lambda_{\text{H}_2, X}$ is in $\text{erg}/\text{cm}^3/\text{s}$.

We assumed H_2 cooling below 10^4 K takes place in an almost neutral medium and thus considered collisions with the following species: other H_2 molecules, H atoms and He atoms. Collisions with H atoms are often the only one taken into account (e.g. Galli & Palla 1998), however, collisions with H_2 and He make a significant contribution and, as we are interested in describing media with a large fraction of H_2 compared to the fraction of H atoms, taking into account the collisions with H_2 and He is necessary to compute cooling that would otherwise be zero in regions poor in atomic hydrogen.

The final expression we use in the code is:

$$\Lambda_{\text{H}_2} = n_{\text{H}_2} \frac{\Lambda_{\text{H}_2, \text{LTE}}}{1 + \frac{\Lambda_{\text{H}_2, \text{LTE}}}{n_{\text{H}} \Lambda_{\text{H}_2, \text{H}} + n_{\text{H}_2} \Lambda_{\text{H}_2, \text{H}_2} + n_{\text{He}} \Lambda_{\text{H}_2, \text{He}}} \quad (4.26)$$

where $\Lambda_{\text{H}_2, \text{LTE}}$ is the LTE cooling rate per H_2 molecule, in erg s^{-1} , and $\Lambda_{\text{H}_2, \text{H}}$, $\Lambda_{\text{H}_2, \text{H}_2}$ and $\Lambda_{\text{H}_2, \text{He}}$, represented in Figure 4.9, are the low density normalised cooling rates in $\text{erg cm}^3 \text{s}^{-1}$ due to collisions with respectively H, H_2 and He. We plot this cooling rate in Figure 4.11 for a hydrogen nuclei number density, $n_{\text{H}_{\text{nuc1}}} = n_{\text{H}} + 2n_{\text{H}_2}$, of 1 cm^{-3} , and different mass ratios of molecular hydrogen over the total hydrogen component. In Figure 4.10, we plot the cooling rate per molecule (without the pre-factor n_{H_2} in 4.26) for a mass fraction $f_{\text{H}_2} = 0.1$ and different total hydrogen nuclei densities, so as to show the utility of the interpolation.

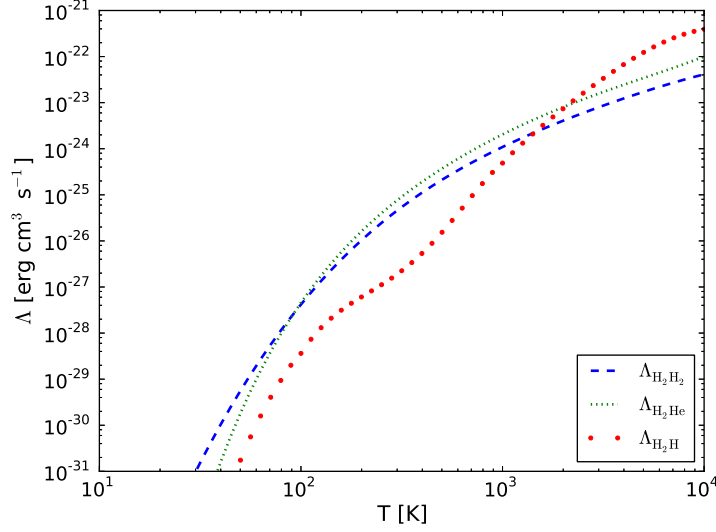


Figure 4.9: Normalised volume cooling rates of H_2 due to collisions with H atoms, H_2 molecules and He atoms (respectively $\Lambda_{\text{H}_2,\text{H}}$, $\Lambda_{\text{H}_2,\text{H}_2}$ and $\Lambda_{\text{H}_2,\text{He}}$).

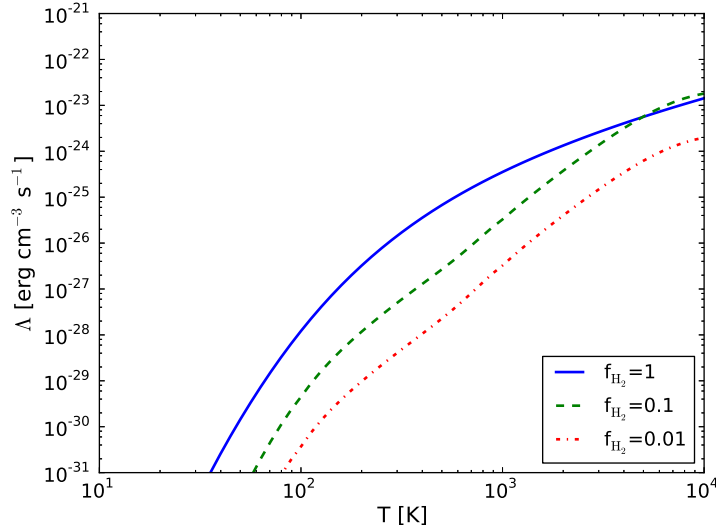


Figure 4.10: Volume cooling rates of H_2 for a hydrogen nuclei number density of 1 cm^{-3} as a function of temperature for different H_2 to total hydrogen mass ratios f_{H_2} . For high fractions of H_2 , and at densities for which the cooling rate depends on collisions, the cooling can become slightly more important just below 10^4 K as the mass fraction is reduced, because the contribution of collisions with atomic hydrogen dominates in this domain of temperatures.

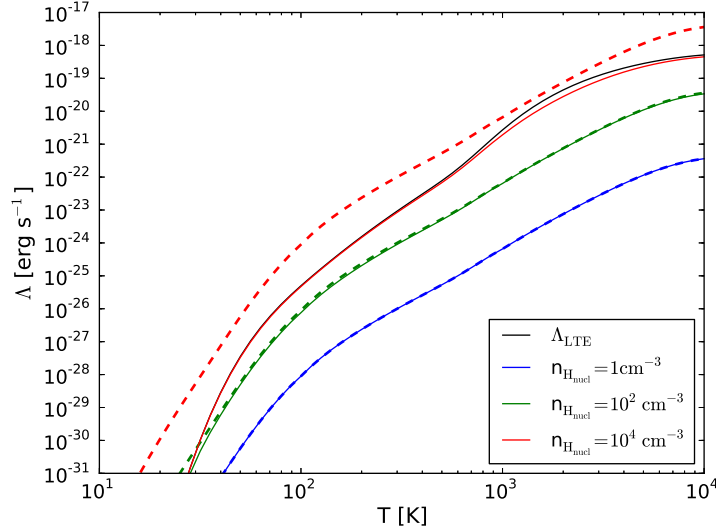


Figure 4.11: Cooling rates of H_2 per H_2 molecule for a mass fraction $f_{\text{H}_2} = 0.1$ and different hydrogen nuclei densities coded by colour. Coloured solid lines are the interpolated cooling function per molecule, the black solid line is the maximal LTE cooling function, and the dotted lines are the low densities approximations. For low $n_{\text{H}_{\text{nucl}}}$, the cooling rate per molecule is significantly lower than the LTE one, while for $n_{\text{H}_{\text{nucl}}} > 10^2 \text{ cm}^{-3}$, the interpolation must be used so as not to overestimate the cooling.

3.5 Cooling by HD

Despite its lower abundance than molecular hydrogen, the molecule HD can help cool the gas because of its permanent electric dipole. For HD dipolar transitions $\Delta J = + - 1$ have stronger probabilities than quadrupole ones of H_2 and make the cooling function by molecule much larger (the LTE cooling rates per molecule are shown on Figure 4.12).

We used data from [Abgrall et al. \(1982\)](#) extended to higher rotational levels (private communication) to compute the LTE cooling function in a similar way than for H_2 .¹

For low densities, we took the function of [Lipovka et al. \(2005\)](#). This cooling function takes into account the collisions of HD with H atoms and only dipolar transitions, which is justified by their much larger contribution to the cooling than quadrupole ones. The cooling function of [Lipovka et al. \(2005\)](#) is valid for a hydrogen atom density between 1 cm^{-3} and 10^8 cm^{-3} . We have densities lower than 1 cm^{-3} in our simulations, so we followed [Glover & Abel \(2008\)](#) by assuming that the cooling function is simply proportional to the H atoms density for low densities, so that the cooling function (per molecule) is simply $n_{\text{H}}\Lambda(n_{\text{H}} = 1 \text{ cm}^{-3})$.

1. Contributions from high energy levels play a noticeable role at high densities for temperatures from around 10^3 K to 10^4 K . As in [Coppola et al. \(2011\)](#), we indeed notice our LTE function is slightly higher for temperatures above 700 K, as we used the same data, than [Lipovka et al. \(2005\)](#) that do not include as many transitions.

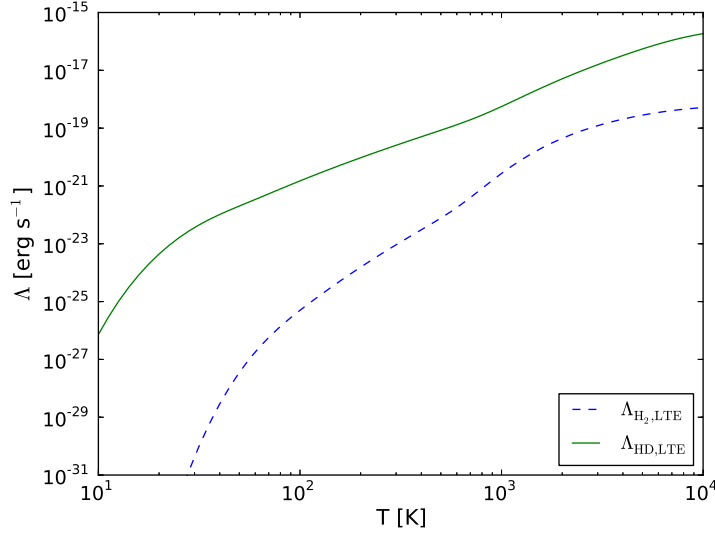


Figure 4.12: LTE cooling rates per molecule for H_2 and HD. HD has a higher cooling rate because of its allowed dipole transitions.

We write, as for H_2 :

$$\Lambda_{\text{HD}} = \frac{\Lambda_{\text{HD,LTE}}}{1 + \frac{\Lambda_{\text{HD,LTE}}}{\Lambda_{n \rightarrow 0}}} \quad (4.27)$$

which prevents errors in the estimation of the cooling function for high densities (more than 10^4 cm^{-3}).

In our present simulations, we have set $x_{\text{HD}} = 10^{-5}x_{\text{H}_2}$ and the temperature cannot go below 100 K so the HD cooling has no influence, as can be seen on Figure 4.13, but it would have an impact in other conditions.

3.6 Total cooling

The total volume cooling rate we use is:

$$\Lambda_{\text{tot}} = \Lambda_{\text{H}_2} + \Lambda_{\text{met}} \quad (4.28)$$

where Λ_{met} is the volume cooling rate due to metals, that depends on the number density of atomic hydrogen (as we did not include cooling due to collisions between H_2 and metals).

This volume cooling rate is represented in Figure 4.14 for a number density of hydrogen nuclei of 1 cm^{-3} , different metallicities and H_2 gas mass fractions. A small gas mass fraction of H_2 can significantly increase the cooling between 10^3 K and 10^4 K .

2. This would also prevent errors for low temperatures (from $\log T = 1$ to $\log T = 1.6$, below our temperature floor) for which the [Lipovka et al. \(2005\)](#) fit is not valid and gives a stronger cooling than the maximal LTE one.

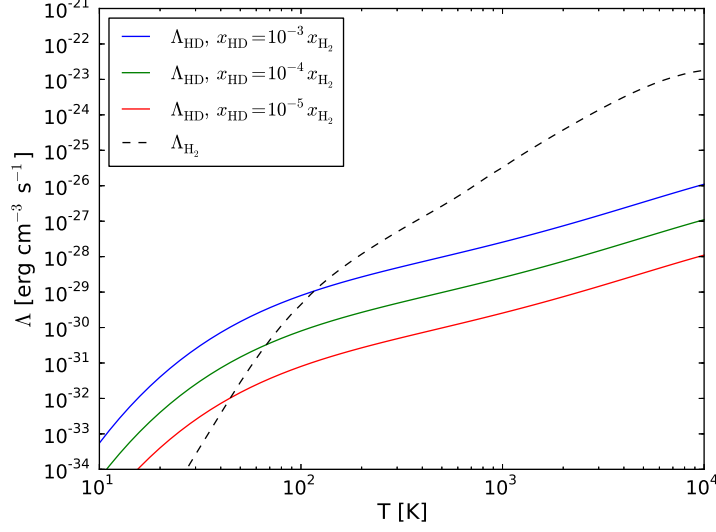


Figure 4.13: Volume cooling rates for $n_{\text{H}_{\text{nucl}}} = 1\text{cm}^{-3}$, for a H_2 mass fraction of 0.1 ($x_{\text{H}_2}=0.05$) and different HD abundances.

3.7 Algorithm for cooling

The interstellar gas component is modelled as an ideal gas with an adiabatic index $\gamma = \frac{5}{3}$ that we keep fixed.

Cooling in the entropy evolution equation The evolution of the specific entropy A_i of a particle i is governed by:

$$\frac{dA_i}{dt} = -\frac{\gamma-1}{\rho_i^\gamma} \Lambda(\rho_i, T_i) + \frac{1}{2} \sum_{j=1}^N m_j \Pi_{ij} \mathbf{v}_{ij} \cdot \nabla_i \bar{W}_{ij} \quad (4.29)$$

where Λ is the volume cooling rate in $\text{erg cm}^{-3} \text{s}^{-1}$ (the sum of the contributions described above) and Π_{ij} is the artificial viscosity tensor.

Semi-implicit time-integration As the cooling time can be lower than the time-steps, we use a semi-implicit cooling scheme³ to stabilise the resolution. We solve iteratively the implicit equation:

$$A_i(t + dt) = A_i(t) + \left(-\frac{\gamma-1}{\rho_i(t)^\gamma} \Lambda(\rho_i(t), T_i(t + dt)) + \frac{1}{2} \sum_{j=1}^N m_j \Pi_{ij} \mathbf{v}_{ij} \cdot \nabla_i \bar{W}_{ij} \right) dt \quad (4.30)$$

where dt is the time-step.

3. we keep the density constant, so it is an isochoric scheme

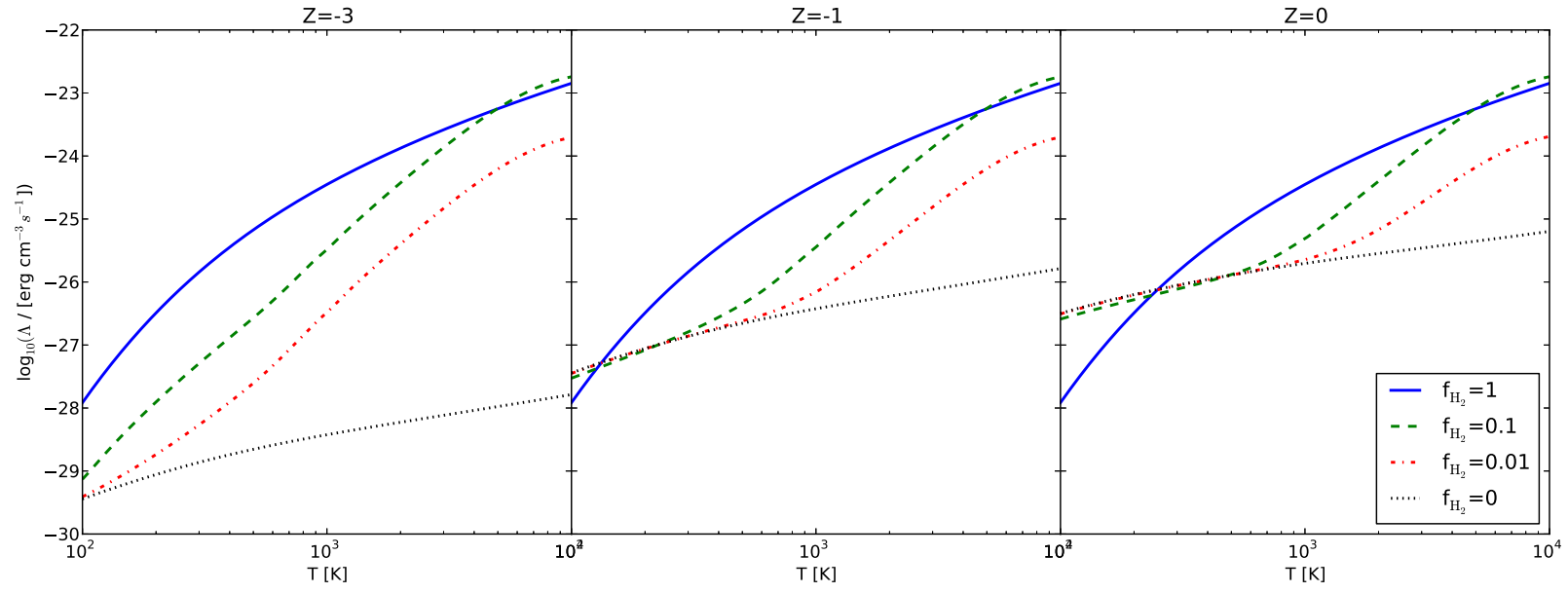


Figure 4.14: Volume cooling rates for different metallicities and H_2 gas mass fractions for $n_{\text{H,nucl}} = 1 \text{ cm}^{-3}$.

Temperature derivation from entropy As $A = \frac{P}{\rho^\gamma}$ and, for an ideal gas:

$$P = \frac{\rho k T}{\mu m_p} \quad (4.31)$$

where m_p is the proton mass and μ , the mean molecular weight, is:

$$\mu = \sum_i x_i \frac{m_i}{m_p} \quad (4.32)$$

with x_i the number fraction of the species i , the relation between temperature and specific entropy is:

$$T = \frac{\mu m_p \rho^{\gamma-1}}{k} A \quad (4.33)$$

For a gas composed of atomic and molecular hydrogen and helium, neglecting the metals contribution:

$$\mu = \frac{4}{1 + \left(3 - 4 \frac{n_{\text{H}_2}}{n_{\text{H}_{\text{nuc}}}} + 4 \frac{n_{\text{e}^-}}{n_{\text{H}_{\text{nuc}}}} \right) X} \quad (4.34)$$

where $n_{\text{H}_{\text{nuc}}}$ is the number density of hydrogen nuclei and X is the hydrogen nuclei mass fraction that we set to 0.76.

We do not compute the ionisation fraction $\frac{n_{\text{e}^-}}{n_{\text{H}_{\text{nuc}}}}$ in the simulations. We assume the gas is quasi neutral below 10^4 K. Above that temperature, we assume there is no molecular hydrogen and the gas is fully ionised (H^+ and He^{2+}). Electronic neutrality then imposes numbers of electrons, H and He ions related by $N_{\text{e}^-} = N_{\text{H}^+} + 2N_{\text{He}^{2+}}$, which gives a molecular weight:

$$\mu = \frac{4}{3 + 5X} \quad (4.35)$$

μ being higher for a neutral gas than for an ionised one, the temperature obtained considering the gas is neutral is higher than the one obtained considering the gas is fully ionised. We simply set to 10^4 K the temperature of the gas in the entropy range for which the temperature assuming a neutral gas is above 10^4 K but the temperature assuming a fully ionised one is above it.

4 H₂ fraction

As our goal was to determine the molecular abundance, but without a detailed chemical scheme, we looked for a simple way of obtaining a realistic mass fraction of molecular hydrogen as a function of the properties of the gas and its environment.

Krumholz et al. (2008, 2009b); McKee & Krumholz (2010) have derived a simple analytic expression for the mass fraction f_{H_2} (ratio of the molecular hydrogen mass on the total hydrogen nuclei mass) for a two-phase equilibrium, taking into account H₂ self-shielding and dust shielding. We follow this approach in writing:

$$f_{\text{H}_2} \simeq 1 - \frac{3}{4} \frac{s}{1 + 0.25s} \quad (4.36)$$

with:

$$s = \frac{\ln(1 + 0.6\chi + 0.01\chi^2)}{0.6\tau_C} \quad (4.37)$$

f_{H_2} is set to zero when $s > 2$.

- χ is a scaled UV radiation field proportional to the Lyman-Werner dissociating field over the number density of hydrogen nuclei. χ can be viewed as the relative importance of dust compared to H₂ in the shielding (Krumholz et al. 2009b): for high radiation fields there is indeed little H₂ so the shielding is predominantly due to dust, while for low radiation fields the higher fraction of H₂ makes self-shielding important.

- τ_C is the dust optical length:

$$\tau_C = \frac{\Sigma\sigma_d}{\mu_{\text{H}}} \quad (4.38)$$

- Σ is a column density $\Sigma = \rho L$ obtained from a local scale height: $L = \frac{\rho}{|\nabla\rho|}$. We compute $(\nabla\rho)_i$, the gradient of the density of the particle i by:

$$\rho_i(\nabla\rho)_i = \sum_j m_j(\rho_j - \rho_i)\nabla_i W(r_{ij}, hi) \quad (4.39)$$

The scale height takes the variation of the density into account: it increases with density but is inversely proportional to its gradient, so it is lower in the case of large gradients encountered on the outer parts of density features like clumps or spiral arms. It is thus well adapted to compute the column density used to determine the shielding from radiation, and interestingly does not depend on resolution as much as other characteristic lengths sometimes used for the same purpose, such as the smoothing length.

- σ_d is set, using the reference Milky Way value, to:

$$\sigma_d = \mathcal{Z}'10^{-21} \text{ cm}^2 \quad (4.40)$$

with \mathcal{Z}' the metallicity we normalise by the solar metallicity:

$$\mathcal{Z}' = \frac{n_{\text{Fe}}/n_{\text{H}}}{n_{\text{Fe}}/n_{\text{H}}|_{\odot}} \quad (4.41)$$

- μ_{H} is the mean mass per H nucleus.

We apply this expression of molecular hydrogen mass fraction to each gas particle.

As we want to use the information of new stellar formation in the disc, the χ is computed using a proxy for the radiation field from new stars G . We assume stars with age inferior to 10 Myr radiate in the Lyman-Werner band and can dissociate the H₂ molecules. We do not consider that older stars radiate in this band, so they do not have any effect on the fraction of H₂ in our simulations. We take $\chi \propto \frac{G}{n_{\text{Hnuclei}}}$, with a tunable scaling factor.

The radiation flux produced by stars decreases with the distance r to a star in $\frac{1}{r^2}$, as the gravitational field. We insert the computation of the flux received from stars younger than

10 Myr by one gas particle in the Gadget-2 gravitational tree functions, as it is similar to computing the gravitational force due to the young stars only and can be easily done by adding a range of variables representing this contribution only.

This approach is simple and would require a more detailed comparison of the obtained mass fractions for simulations directly comparable with observations. What we wanted was to have a reasonable molecular hydrogen fraction that was allowed to change for each particle, depending on the evolution of the galaxies, and therefore kept this method.

5 Star formation

In the stochastic star formation approach (Katz 1992) that we use, gas particles that satisfy selection rules listed below in this section have the following probability of spawning a stellar particle by time-step Δt :

$$p_* = \frac{m_g}{m_*} \left(1 - e^{-c_* \Delta t / t_*} \right) \quad (4.42)$$

meaning that gas particle of mass m_g can spawn a star particle of mass m_* with this probability at each time-step, the mass of the gas particle being then reduced by m_* , until there is no more mass in the gas particle. We used the free-fall time $t_{\text{ff}} = \sqrt{\frac{3\pi}{32G\rho}}$ for t_* in most of our simulations.

The number of $N_{g \rightarrow *}$ of star particles created by gas particle is a compromise between a good mass and time resolution of star formation and CPU cost: if several stellar particles are created from a single gas particle, star formation will be smoother, temporally better resolved, but the total number of particles can increase significantly, which slows down the code. We follow Springel & Hernquist (2003) that take a number of 4 star particles created by gas particle.

In the case where $N_{g \rightarrow *}$ is greater than one, we note that this spawning scheme implies that gas particles will have different masses, either the initial m_g , or a smaller multiple of $\frac{m_g}{N_{g \rightarrow *}}$. The density and smoothing length are computed by Gadget-2 so that the mass contained in a sphere of radius h_i is fixed, h_i being the smoothing length of the particle i , and we slightly modified the algorithm to take into account the different masses, so that this mass condition is still satisfied. The impact is minor, it makes the smoothing length slightly higher for a given density if low mass gas particles are amongst the neighbours. It is more useful if we want to monitor precisely the feedback energy that is given to the neighbours (this was the initial motivation for such a change).

We use common selection rules for the particles that are allowed to spawn stars:

- They must have a density higher than a threshold n_{Hmin} . We set $n_{\text{Hmin}} = 10^{-1} \text{cm}^3$ for most of our simulations. The threshold can be increased to allow for an ISM with more density structures, but if it is too high, the mass resolution must be increased for the Jeans mass to still be resolved.

- They must have a temperature lower than a maximum temperature T_{\max} . We use $T_{\max} = 30\,000$ K, which happens not to be selective as only a few diffuse particles can reach these temperatures in most of our simulations that use kinetic SNII feedback.
- They must be in a converging flow ($\nabla \cdot \mathbf{v} < 0$).

We note that using a constant value for t_* in the probability law (which amounts to considering a Schmidt law with an exponent $n = 1$) can give a highly heterogeneous gas medium, similarly to what is achieved by increasing the threshold density for star formation, because as the SFR is proportional only to the density and not its square, high density peaks can develop.

6 Supernova feedback

As stellar particles usually have a much larger mass than individual stars, they are considered as representing a whole stellar population. Assuming an IMF to determine which fraction are expected to explode as SNII, it is possible to compute the energy released at or after the formation of a stellar particle. If we take an IMF $\psi(M)$ –such that $\psi(M)dM$ is the number of stars of mass between M and $M + dM$ – the supernovae energy released by formed stellar mass is:

$$\epsilon_{\text{SN}} = \frac{\int_{\text{SN mass range}} \psi(M) dM}{\int_{\text{full mass range}} M \psi(M) dM} E_{\text{SN}} \quad (4.43)$$

where E_{SN} is the energy released by one supernova. We consider a supernova explosion releases the canonical value $E_{\text{SN}} = 10^{51}$ erg.

A fraction α_{fb} of this energy is given to the ISM, while the rest is radiated away. Each new stellar particle of mass m_* will thus input an energy $E_{\text{input}} = \alpha_{\text{fb}} \epsilon_{\text{SN}} m_*$. We consider that one SNII explodes for 100 M_{\odot} that are formed, which is of the order of the fractions obtained from commonly used initial mass functions (such as a Salpeter IMF with slope -2.35 and lower and upper limits of 0.1 and 40 M_{\odot} , with stars more massive than 8 M_{\odot} considered to be supernovae), so we have $\epsilon_{\text{SN}} = 10^{49}$ erg/ M_{\odot} .

We use the “momentum” version of kinetic feedback (Navarro & White 1993). Each neighbour i of a new star particle 0 receives an energy weighted by its distance to the new stellar particle:

$$E_i = \frac{W(|\mathbf{r}_{i0}|, h_0)}{\sum_{\text{ngb } k} W(|\mathbf{r}_{k0}|, h_0)} E_{\text{input}} \quad (4.44)$$

so that the sum of the energies given to the neighbours is E_{input} . If the newly created stellar particle has left a remnant gas particle, no feedback energy is given to the remnant. We recompute the smoothing length and neighbours list at the position of a new stellar particle, considering only the neighbouring gas that has not been turned into stars (and not considering a possible gas particle remnant at the exact position of the new stellar particle). Therefore

the sum of the fractions involving kernels is indeed unity, and the mass of the gas affected by each supernova explosion is a constant.

The neighbours are given a velocity kick $\sqrt{\frac{2E_i}{m_i}}$, directed along the line joining the stellar particle and the neighbour, and away from the new stellar particle.

The number $N_{g \rightarrow \star}$ of stellar particles created out of one gas particle has an influence on the distribution of feedback energy. Feedback energy is more gradually input for a larger $N_{g \rightarrow \star}$.

Variations We tried a couple of variations in the exact implementation of SNII feedback. We preferred keeping the simple approach of kinetic feedback in the momentum version we described above, but we briefly mention the attempts here:

- Thermal feedback can be chosen in our code. We have a tunable time during which the cooling of particles affected by feedback is turned off, allowing the particles to transfer kinetic energy to others rather than being simply cooled by the strong cooling in dense star forming regions.
- We implemented a hydrodynamical decoupling for particles affected by feedback, following [Springel & Hernquist \(2003\)](#). A kicked particle does not feel nor contribute to hydrodynamical forces for a while, until a tunable amount of time has passed or the density of the particle has fallen below a threshold. This increases significantly the effect of feedback, as gas particles are not braked by the artificial viscosity force for a while, allowing them to go further away from the disc plane in our disc simulations.
- The efficiency of a simple kinetic feedback is especially reduced in dense regions because of our implementation in which we input energy to all the gas particles in a smoothing kernel. To avoid strong clumping⁴, we therefore implemented a scheme in which a constant number of neighbours of a new stellar particle are kicked (or heated). The neighbours are all given the same suitable probability of being chosen $p = \frac{N_{\text{feedback}}}{N_{\text{ngb}}}$ where N_{feedback} is the desired number of neighbours affected by feedback and N_{ngb} is the number of neighbours. In the case in which the smoothing kernel contains fewer neighbours than N_{feedback} , all the neighbours are affected by feedback. This scheme requires more computation steps.
- We also tried to increase the feedback strength (limited to the maximum energy of 10^{51} erg per SN) for new stellar particles born in a specially dense region. In a simple implementation, the feedback strength was multiplied by two for particles having a density above a threshold given as a parameter to the code.
- Finally, we tried to input feedback both thermally and kinetically. This can lead to a reduced feedback in the case where particles have their cooling stopped and are decou-

4. that can be very CPU consuming and can lead to a questionable validity of the simulation if too high densities are reached, the Jeans length/mass are far from resolved and the SPH kernel leads to a potential numerical artefactual clumping instability

pled from hydrodynamics during the same amount of time. Indeed, if heated particles are also hydrodynamically decoupled, their internal energy can not be transferred to other particles in the form of kinetic energy because the hydrodynamical forces temporarily exclude the decoupled particles. Once the decoupling ends, if the cooling is turned on at the same time or rapidly, the thermal feedback will be rendered poorly efficient as the cooling will quickly lower the internal energy of particles.

Chapter 5

Simulations

We performed simulations mainly aiming at testing the effects of molecular hydrogen cooling and SNII feedback on star formation in disc galaxies, using the method we described in last chapter. In the present chapter, we first describe the initial conditions we used and then show our results on the variation of feedback efficiency and the impact of molecular hydrogen inclusion. The last section describes a few variations in resolution, disc parameters, or star formation and feedback implementation.

1 Initial Conditions

We generate initial conditions with a code we have adapted so that it uses gravitation and hydrodynamics routines of Gadget-2 for consistency with the simulations.

We consider the case of a giant Sb galaxy consisting of stellar and gaseous discs, a stellar bulge and a CDM halo.

1.1 Density profiles

Gaseous and stellar discs The gaseous and stellar discs follow Miyamoto-Nagai density profiles (Miyamoto & Nagai 1975). This profile is derived from the following axisymmetric potential, in cylindrical coordinates:

$$\Phi_{\text{MN}}(R, z) = -\frac{GM}{\left(R^2 + (a + \sqrt{z^2 + b^2})^2\right)^{1/2}} \quad (5.1)$$

where M is the total mass and a and b are scale lengths that allow for a varying degree of flattening: for $a = 0$, this potential reduces to the spherically symmetric Plummer potential, while for $b = 0$, it reduces to the axisymmetric Kuzmin potential for an infinitely thin disc.

The corresponding mass density, deduced from the Poisson equation, is:

$$\rho_g(R, z) = \frac{b^2 M}{4\pi} \frac{aR^2 + (a + 3\sqrt{z^2 + b^2})(a + \sqrt{z^2 + b^2})^2}{\left(R^2 + (a + \sqrt{z^2 + b^2})^2\right)^{5/2} (z^2 + b^2)^{3/2}} \quad (5.2)$$

Sb	M_h	M_d	M_b	M_g		
in M_\odot	$1.7 \cdot 10^{11}$	$4.5 \cdot 10^{10}$	$1.1 \cdot 10^{10}$	$0.9 \cdot 10^{10}$		
	r_h	a_d	h_d	r_b	a_g	h_g
in kpc	12	5	0.5	1	11.8	0.2

Table 5.1: Sb galaxy parameters

Stellar bulge and dark matter halo The spherical stellar bulge and dark matter halo have Plummer density profiles, which are in spherical coordinates:

$$\rho_b(r) = \frac{3M}{4\pi r_c} \frac{1}{\left(1 + \frac{r^2}{r_c^2}\right)^{5/2}} \quad (5.3)$$

All the masses and characteristic lengths are specified in Table 5.1. We use a total of 1 200 000 particles with 400 000 particles of each type: gas, stars, and dark matter. The masses of particles that follow are shown on Table 5.2.

1.2 Velocities

Gaseous and stellar discs The radial velocity dispersion of the discs is derived from:

$$\sigma_r(r) = \frac{3.36GQ\Sigma(r)}{\kappa(r)} \quad (5.4)$$

with Q the Toomre parameter that we set to $Q = 1$ for both discs, Σ the total surface density and κ the epicyclic frequency derived from the total potential Φ by:

$$\kappa^2(R) = \frac{\partial^2 \Phi}{\partial R^2} \Big|_{z=0} + \frac{3}{R} \frac{\partial \Phi}{\partial R} \Big|_{z=0} \quad (5.5)$$

The azimuthal velocity dispersion is obtained from:

$$\frac{\sigma_\theta(R)}{\sigma_r(R)} = \frac{\kappa(R)}{2\Omega(R)} \quad (5.6)$$

with Ω the circular frequency obtained by:

$$\Omega^2(R) = \frac{1}{R} \frac{\partial \Phi}{\partial R} \Big|_{z=0} \quad (5.7)$$

The vertical dispersion is set by assuming an isothermal equilibrium (e.g. [Binney & Tremaine 2008](#)):

$$\sigma_z(R) = \sqrt{2\pi Gh\Sigma(R)} \quad (5.8)$$

We use the gravitation and hydrodynamics routines of Gadget-2 to obtain the forces acting on particles. The circular velocity of disc particles are computed using these accelerations and an asymmetric drift correction is added to have a more realistic velocity profile.

The Miyamoto-Nagai profiles are chosen because the associated potential is analytic and the initial velocity dispersions can thus be easily computed, but relaxation makes the profiles quickly exponential.

Bulge and dark matter halo The velocity dispersion of the spherical components is derived from one of the Jeans equations for a non-rotating spherical system with an isotropic velocity dispersion. The dispersions $\sigma_i^2(r)$ where i is one of the spherical coordinates are thus:

$$\sigma_i^2(r) = \frac{1}{\rho(r)} \int_r^\infty \rho(u) \frac{\partial \phi}{\partial u} du \quad (5.9)$$

The velocity curve for this analytic model, with the contributions of the different components, is shown in Figure 5.1. The rotation is due mainly to the stellar components near the centre of the galaxy, and to dark matter at large radii.

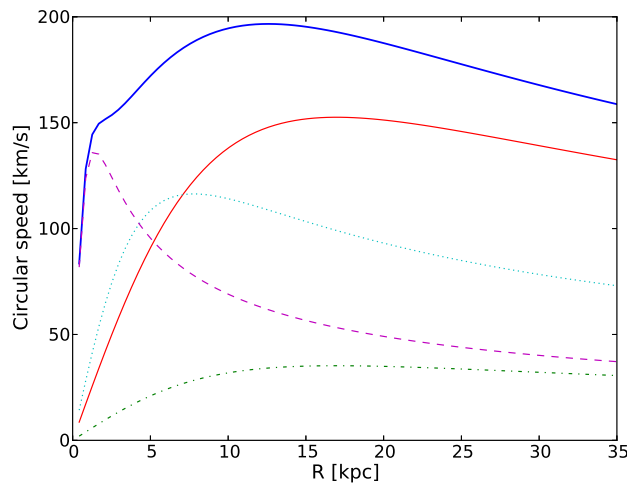


Figure 5.1: Initial rotation curve. Top solid (blue) thick line: total rotation curve. Dashed (purple) line: bulge. Dotted (green) line: stellar disc. Dash-dot (green) line: gas. Solid (red) line: dark matter halo

1.3 Resolution

The number of particles should ideally be the largest possible to have a good mass resolution, which allows the Jeans mass to be well resolved. We run simulations with 1 200 000 initial particles: a third are gas particles, a third are stellar particles and a third are dark matter particles. Table 5.2 shows the particle masses we have in the particular case of our galaxy model that will be detailed in 1. New stellar particles have a mass $m_{\text{new} *} = \frac{m_g}{N_{g \rightarrow *}}$ depending on the parameter $N_{g \rightarrow *}$, the number of stellar particles produced out of one gas particle. We typically chose $N_{g \rightarrow *} = 4$ in our simulations, following [Springel & Hernquist \(2003\)](#), as a compromise between a good time resolution for star formation and CPU cost.

The gravitational softening length ϵ depends on this number of particles: a too small value for a given number of particles introduces unphysical two-body relaxation in media that are collisionless (stellar components of galaxies and dark matter haloes), while a too large one decreases the spatial resolution by “blurring” density features and does not allow

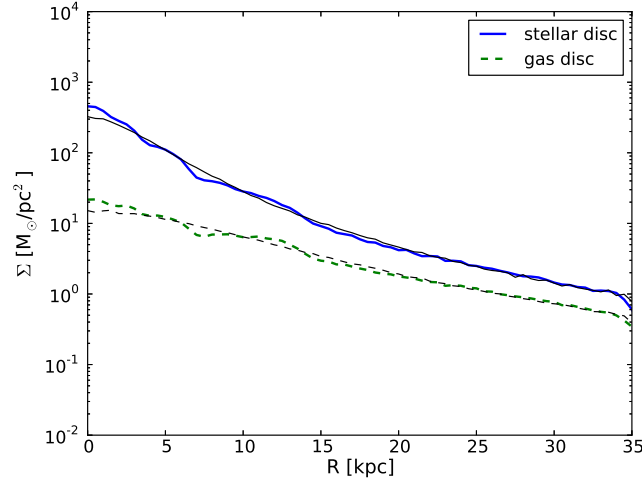


Figure 5.2: Initial surface densities. Dotted line: gas. Dashed line: stars.

ϵ	m_{DM}	m_{\star}	m_g
[pc]	[M_{\odot}]	[M_{\odot}]	[M_{\odot}]
100	$3.7 \cdot 10^5$	$1.4 \cdot 10^5$	$2.5 \cdot 10^4$

Table 5.2: Resolution: gravitational softening and particle masses.

the Jeans length to be gravitationally resolved. Gravitational softening lengths ϵ are usually taken as scaling with the mean inter-particle distance, therefore as the number of particles to the power $\frac{1}{3}$ for a 3-dimensional simulation. We take a softening length $\epsilon = 100$ pc for all particle types. This particular value is derived from the optimum found in the GalMer simulations (eg Di Matteo et al. 2007) which took ten times less particles for a softening of 280 pc. The GalMer simulations were isothermal, at 10^4 K, and since here the temperature reaches down to 100 K, we take a softening length that is a little inferior to the cubic root, while still allowing for an efficient computation on a few tens of computing cores.

1.4 Relaxation of initial conditions

If we start simulations directly from this point, the initial little departure from equilibrium due to the inexact analytic combination of spherical and disc components will give rise to an annulus instability: concentric annuli grow from the centre of the discs to their edges for a while, until the velocity dispersions have adjusted themselves. We thus further prepare the initial conditions by letting the galaxy evolve for 300 Myr with only gravitational forces included for any type of particles. This allows us to start the simulations with dynamically relaxed discs.

The initial surface densities of gas and stars are shown in Figure 5.2, and a snapshot of the gas is shown on Figure 5.3.

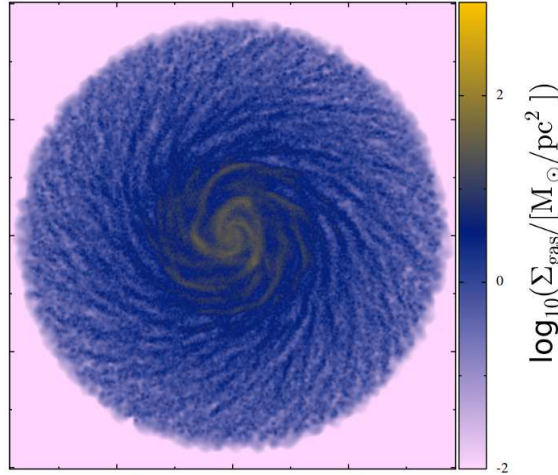


Figure 5.3: Initial density map of the gas disc. The box size is [40 kpc x 40 kpc]. Done with the visualisation software SPLASH (Price 2007).

2 Feedback efficiency variation in metal-cooling only simulations

As we have not so far implemented any gas chemical enrichment by stars, we assumed there is a metallicity gradient in the gas disc. We take a central metallicity $Z = [\text{Fe}/\text{H}]$ such that $Z(R=0) = Z_{\odot} + 0.5$ and assume the metallicity decreases of 1 dex per 10 kpc:

$$Z(R) = Z(R=0) - \frac{R[\text{kpc}]}{10} \quad (5.10)$$

where R is the cylindrical radius.

We first present a range of simulations in which we set some star formation parameters:

- The star formation efficiency per free-fall time c_{\star} in the Schmidt law $\frac{d\rho_{\star}}{dt} = -\frac{c_{\star}}{t_{\text{ff}}}\rho_g$ is set to $c_{\star} = 0.1$.
- The number density threshold for star formation n_{Hmin} is set to $n_{\text{Hmin}} = 10^{-1} \text{ cm}^3$.
- The number of stars spawned by gas particle $N_{g \rightarrow \star}$ is set to $N_{g \rightarrow \star} = 4$.

We set the initial temperature to 100 K throughout the gas disc and forbid the temperature from being lower during the simulation.

We first perform simulations with no molecular hydrogen, with varying feedback efficiencies α_{fb} , representing the fraction of the 10^{51} erg that is input to the surrounding gas for the explosion of one SNII. We have four different feedback efficiencies: either no feedback ($\alpha_{\text{fb}} = 0$), $\alpha_{\text{fb}} = 1\%$, $\alpha_{\text{fb}} = 10\%$ or $\alpha_{\text{fb}} = 40\%$.

2.1 Gas and stars discs

Surface density maps of the gas discs for these runs are shown in Figures 5.4 and 5.5 at three simulation times: 0.5 Gyr, 1 Gyr and 3 Gyr.

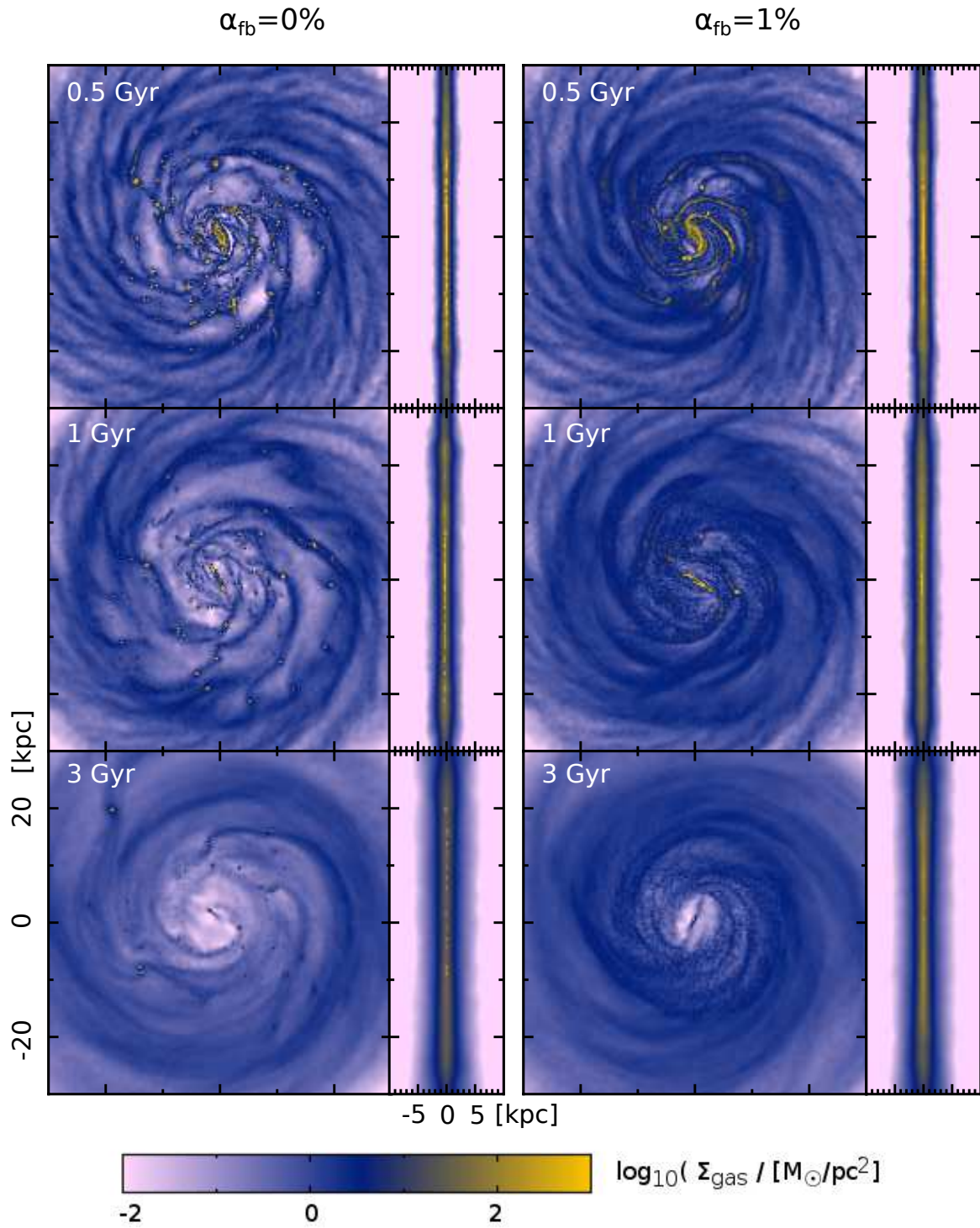


Figure 5.4: Projections of the gas density after 0.5 Gyr, 1 Gyr and 3 Gyr of evolution. Box sizes are [30 kpc x 30 kpc] for face-on views and [30 kpc x 20 kpc] for edge-on views. Each row corresponds to a feedback efficiency indicated on the top. The column integrated density scale is the same for all plots.

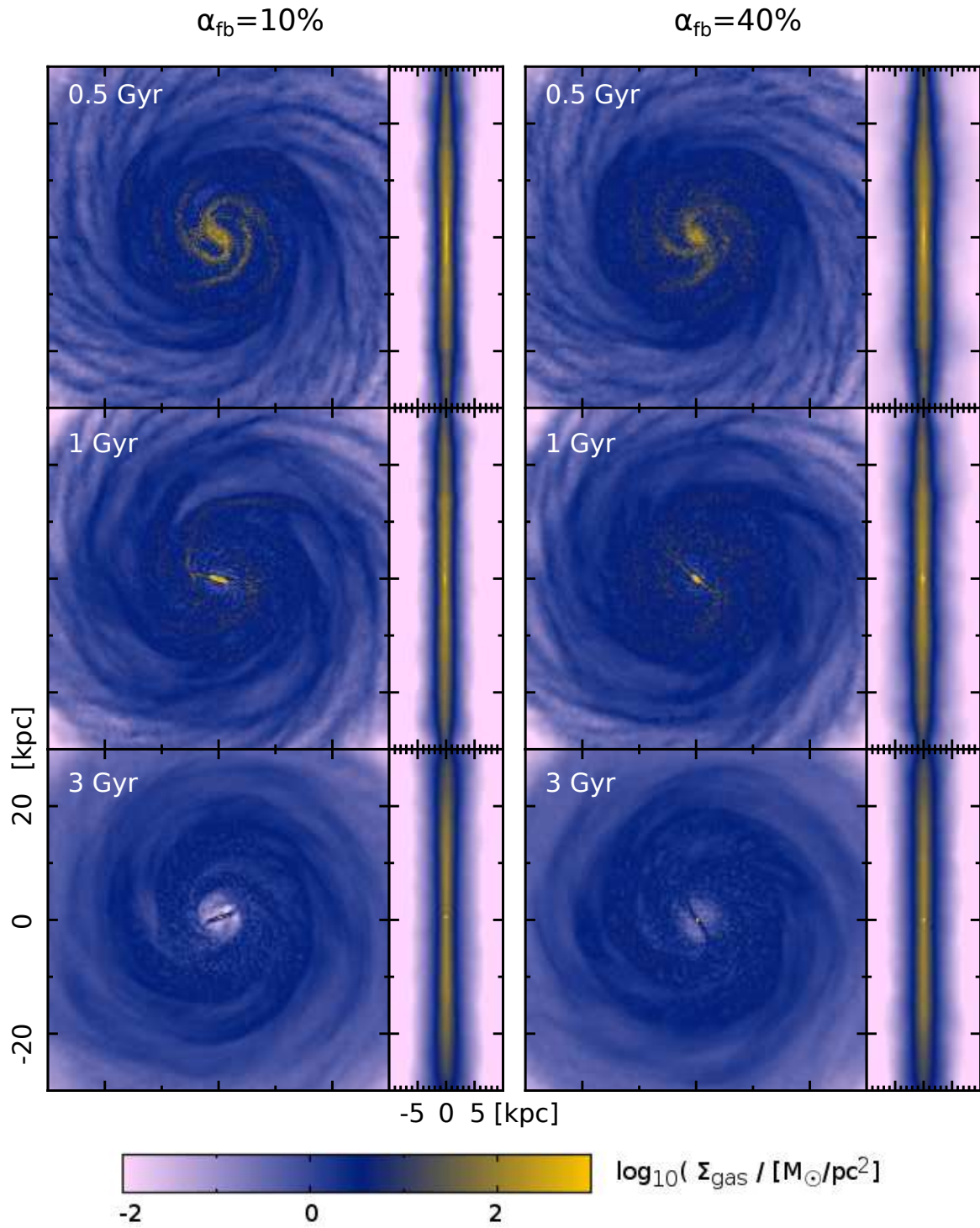


Figure 5.5: Projections of the gas density after 0.5 Gyr, 1 Gyr and 3 Gyr of evolution. Box sizes are [30 kpc x 30 kpc] for face-on views and [30 kpc x 20 kpc] for edge-on views. Each row corresponds to a feedback efficiency indicated on the top. The column integrated density scale is the same for all plots.

The gas can reach smaller values of local volume density when feedback is included, as star formation in dense regions inputs some energy in the gas and prevents it from getting denser. The consequences of changing the feedback efficiency are visible on the surface density maps:

- For the run without feedback, the central part of the galaxy exhibits a strong density contrast on the snapshots at 0.5 Gyr and 1 Gyr, many small clumps and thin spiralling filaments can be seen.
- For a feedback efficiency $\alpha_{\text{fb}} = 1\%$, only a few clumps can be seen. Spiral structures are also smoother.
- For $\alpha_{\text{fb}} = 10\%$ and $\alpha_{\text{fb}} = 40\%$, no clear clumps can be seen.

A central thin bar is formed in all the cases. After 3 Gyr, the bar is still clearly visible for the higher feedback efficiencies $\alpha_{\text{fb}} = 10\%$ and $\alpha_{\text{fb}} = 40\%$, but is less obvious otherwise, because the central parts have been depleted from gas by star formation. This bar is visible in young stars, as will be seen in next section. The stellar component of the simulation with $\alpha_{\text{fb}} = 1\%$ is shown on the top row of Figure 5.18.

Fourier analysis of the surface density It is possible to analyse quantitatively the patterns (bars, spiral arms) and their speed by Fourier analyses (e.g. Bournaud & Combes 2002). We included in the code a spatial Fourier analysis every 1 Myr. We decompose the surface density Σ the following way:

$$\Sigma(r, \theta) = \Sigma_0(r) + \sum_m [a_m(r) \cos(m\theta) + b_m(r) \sin(m\theta)] \quad (5.11)$$

where the a_m and b_m coefficients for radius bins are computed by:

$$a_m(r) = 2 \int_0^{2\pi} \mu(r, \theta) \cos(m\theta) d\theta \quad (5.12)$$

$$b_m(r) = 2 \int_0^{2\pi} \mu(r, \theta) \sin(m\theta) d\theta \quad (5.13)$$

We normalise the coefficients by $\Sigma(r)$, writing: $A_m(r) = \frac{a_m(r)}{\Sigma(r)}$ and $B_m(r) = \frac{b_m(r)}{\Sigma(r)}$ and we then compute $C_m(r) = \sqrt{A_m^2(r) + B_m^2(r)}$. The phase of the mode m is defined by $\phi_m(r) = \arctan\left(\frac{a_m(r)}{b_m(r)}\right)$. A time Fourier transform of $C_m(r)e^{i\phi_m(r)}$ gives the characteristic frequencies of the mode m at radius r .

We are especially interested in the phase of the $m = 2$ mode (bar or two-arms spiral patterns). We represent on Figure 5.6 the result of this time Fourier analysis for the case $\alpha_{\text{fb}} = 1\%$. The analysis is performed from a simulation time $t = 0.5$ Gyr to $t = 2.5$ Gyr, allowing the determination of the speed of the gaseous and stellar bars in this period.

2.2 Thermal state of the gas

Figure 5.7 shows the specific energy-number density histograms after 0.5 Gyr of evolution, a time at which gaseous discs are actively forming stars in all the simulations.

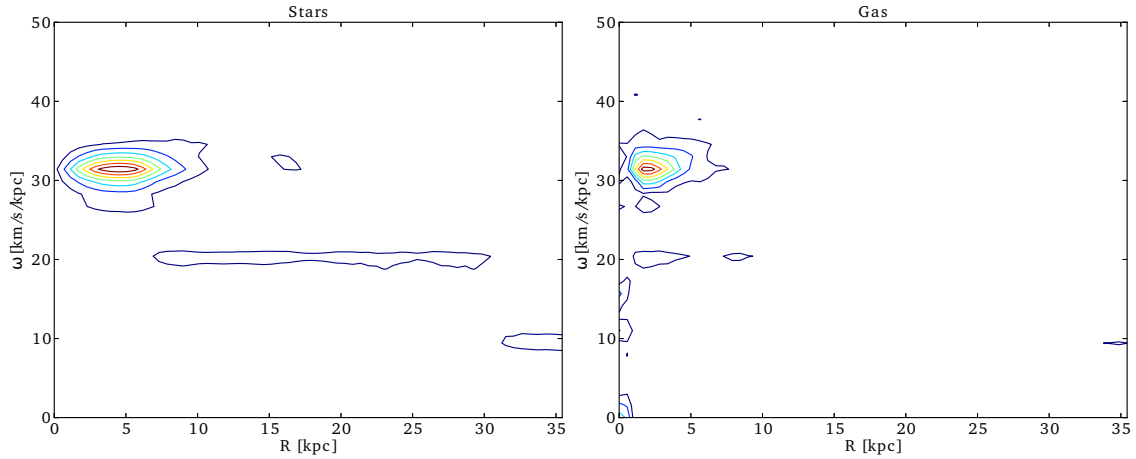


Figure 5.6: Results of the time Fourier analysis of the $m = 2$ component performed between $t = 0.5$ Gyr and $t = 2.5$ Gyr. The bar rotation speed is found to be $\omega_{\text{bar}} = 31$ km/s/kpc. Especially for the stellar component, a lagging pattern (spiral arms) can be seen at $\omega = 20$ km/s/kpc.

On the top and right of each plot, the marginal probability density functions (PDFs) of respectively hydrogen nuclei number density and temperature are shown. The fraction of gas at $T \simeq 10^4$ K increases with feedback, while the cold dense gas fraction decreases. On the density PDFs one can see that gas reaches smaller maximum densities for higher feedback efficiencies and there is an increasingly high fraction of diffuse gas. In the low feedback efficiency runs, a significant fraction of the dense gas has a temperature close to the minimum: this is the dense gas of the central parts, subject to metal-line cooling. The fraction decreases for higher feedback efficiencies, because of the dissipation of energy by feedback, making the densest gas of the simulations warmer. If the gas is heated by pressure forces, viscous shocks or feedback, its temperature does not reach temperatures much beyond 10^4 K because of the stronger H, He, and metals cooling it undergoes above.

The diagonal branches observed on the left of each plot account for gas that, away from the centre of the disc, is subject to very little cooling because of the metallicity gradient, and thus cools down adiabatically. For comparison, a simulation with cooling only above 10^4 K and a feedback efficiency of 10% has the temperature-density histogram of Figure 5.8. The densest gas lies at 10^4 K.

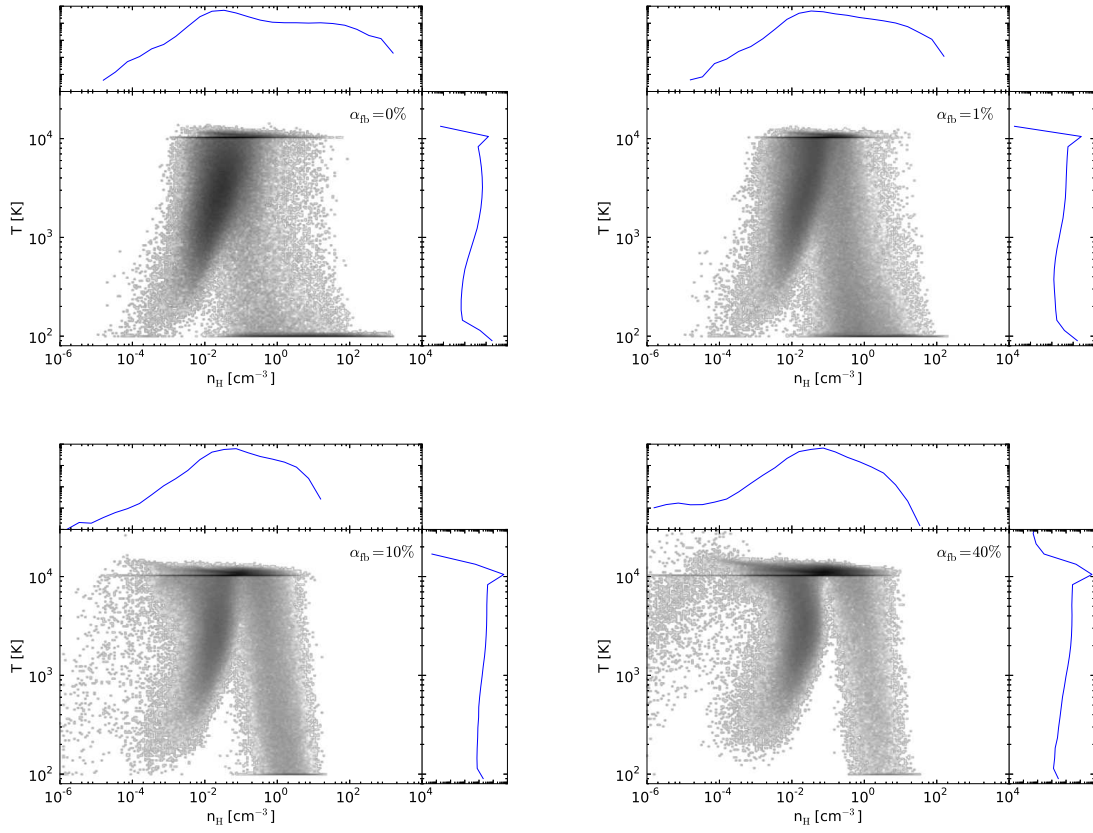


Figure 5.7: Temperature-density histograms of the gas after 0.5 Gyr of evolution for the different feedback efficiencies. The 2D histograms and marginal 1D histograms are all mass weighted and normalised to unity.

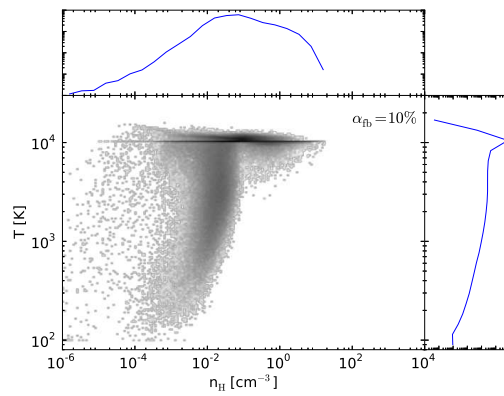


Figure 5.8: Temperature-density histograms of the gas after 0.5 Gyr of evolution for a run with $\alpha_{fb} = 10\%$ but no cooling below 10^4 K. The 2D histograms and marginal 1D histograms are mass weighted and normalised to unity.

3 Simulations including H_2

We now study the impact of the inclusion of H_2 on the gas physical state, star formation and structure of the discs. We take the same metallicity gradient, star formation parameters and temperature floor than the ones described in the beginning of last section.

The temperature floor we apply is more exactly a specific energy floor, corresponding to a temperature of 100 K for purely atomic gas, and going up to 186 K for gas with hydrogen present only in the molecular form. Gadget-2 uses the specific entropy to evolve the gas (notably to compute hydrodynamical forces). This specific entropy A is such that $A \propto \frac{T}{\mu}$, with T the temperature and μ the mean molecular weight. At a given simulation time, the specific entropies only are known, and we deduce the temperatures needed to calculate the adequate volume cooling rate with the method described in 3.7 of Chapter 4.

3.1 H_2 fraction

We first set the feedback efficiency to $\alpha_{\text{fb}} = 1\%$ and tune the χ factor in the H_2 fraction so that we find a global H_2 fraction that is consistent with observations while having enough molecular hydrogen fraction to study its effects. Our metallicity gradient implies that H_2 will tend to be less present in the outer parts of the galaxy where the metallicity and dust abundance are low and the gas is less shielded from Lyman-Werner radiation. However, this is compensated by the lower star formation rate in these regions, which decreases the ambient Lyman-Werner luminosity. We plot the evolution of the total mass fraction of H_2 in Figure 5.9 for four different UV flux scaling factors.

The global mass fraction first decreases with time because new stars are formed and contribute to the dissociating radiation field and becomes stable when the SFR becomes almost null (see the solid line of Figure 5.15 for the evolution of the gas mass). Figure 5.10 shows the surface density of H_2 and atomic hydrogen gas HI after 0.5 Gyr of evolution for the case $\chi \times 50$ that we choose. Such a surface density profile is similar to some observed profiles of local galaxies described in [Young & Scoville \(1991\)](#), and more recently in [Bigiel et al. \(2008\)](#).

3.2 Gas physical state

Gas disc Figure 5.11 shows the aspect of the disc for $\alpha_{\text{fb}} = 1\%$ at the same simulation epochs than in Figure 5.4, whose second column is the simulation for the same feedback efficiency but without H_2 .

Cooling by metals in the purely HI simulation or mainly by H_2 in the now H_2 dominated central part make this region similar in both simulations. The difference is in the outer parts of the galaxy for which metal-line cooling is poorly efficient because of our assumed metallicity gradient. In this case, the gas remains diffuse with no other cooling processes, but

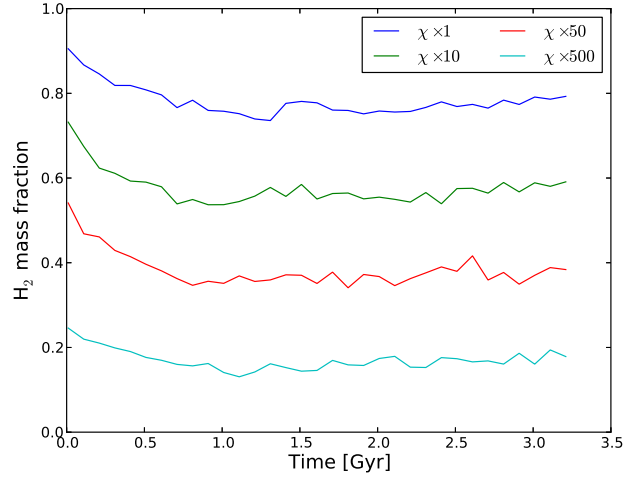


Figure 5.9: Global H_2 mass fraction versus time for $\alpha_{\text{fb}} = 1\%$. The UV flux increases from top to bottom.

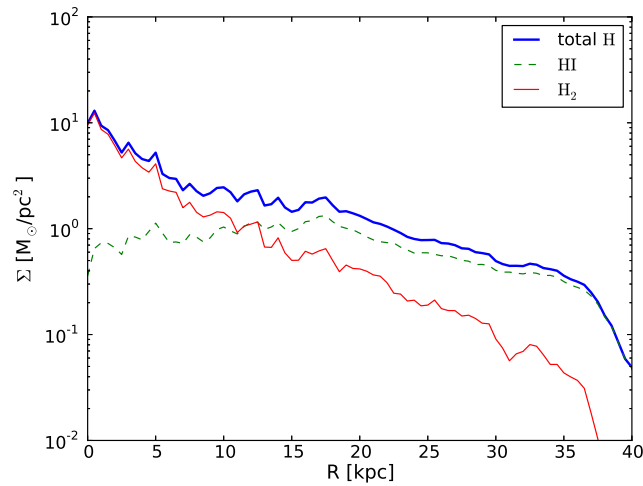


Figure 5.10: Radial distribution of the surface density of H_2 , atomic gas HI and total hydrogen gas after 0.5 Gyr for $\alpha_{\text{fb}} = 1\%$ and the selected UV scaling factor.

the inclusion of H_2 allows the gas to be clumpier: we see density features that were absent in the purely atomic simulation. The surface density of H_2 is also plotted. It indeed follows the density features of the gas: the clumps and filamentary structures can be seen in H_2 gas. The HI gas has a smoother surface density and extends further away from the disc plane. The central parts are mostly depleted from HI.

Thermal state The temperature-number density histograms of Figure 5.12 and the marginal PDFs show higher fractions of gas in the cold dense phase than for the corresponding

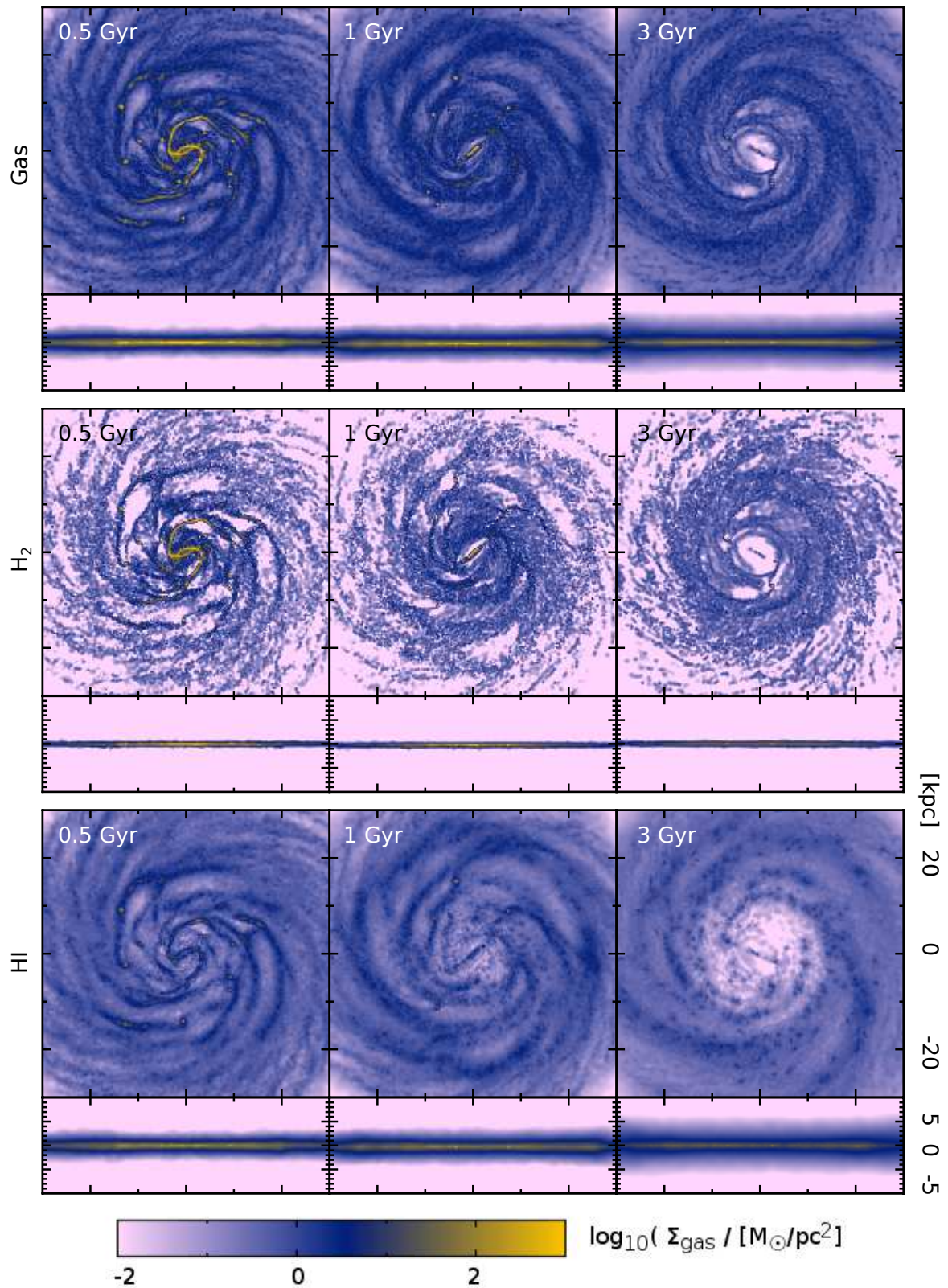


Figure 5.11: Projections of the gas density (top row), H_2 density (middle row) and HI density (bottom row) after 0.5 Gyr, 1 Gyr and 3 Gyr of evolution. Box sizes are [30 kpc x 30 kpc] for face-on views and [30 kpc x 10 kpc] for edge-on views. The column integrated density scale is the same for all plots.

feedback efficiencies without molecular hydrogen. There is no clear diagonal branch because there is some efficient cooling in the whole disc. The presence of two mass concentrations at low temperatures is due to our adopted threshold in specific energy, which correspond to a temperature of 100 K for gas that is atomic, and to a temperature ~ 200 K for gas that is fully molecular. The densest gas is mostly in the molecular form, therefore concentrating at this second temperature. We also see, as in the simulations without any molecular hydrogen, a concentration of gas at a temperature of about 10^4 K.

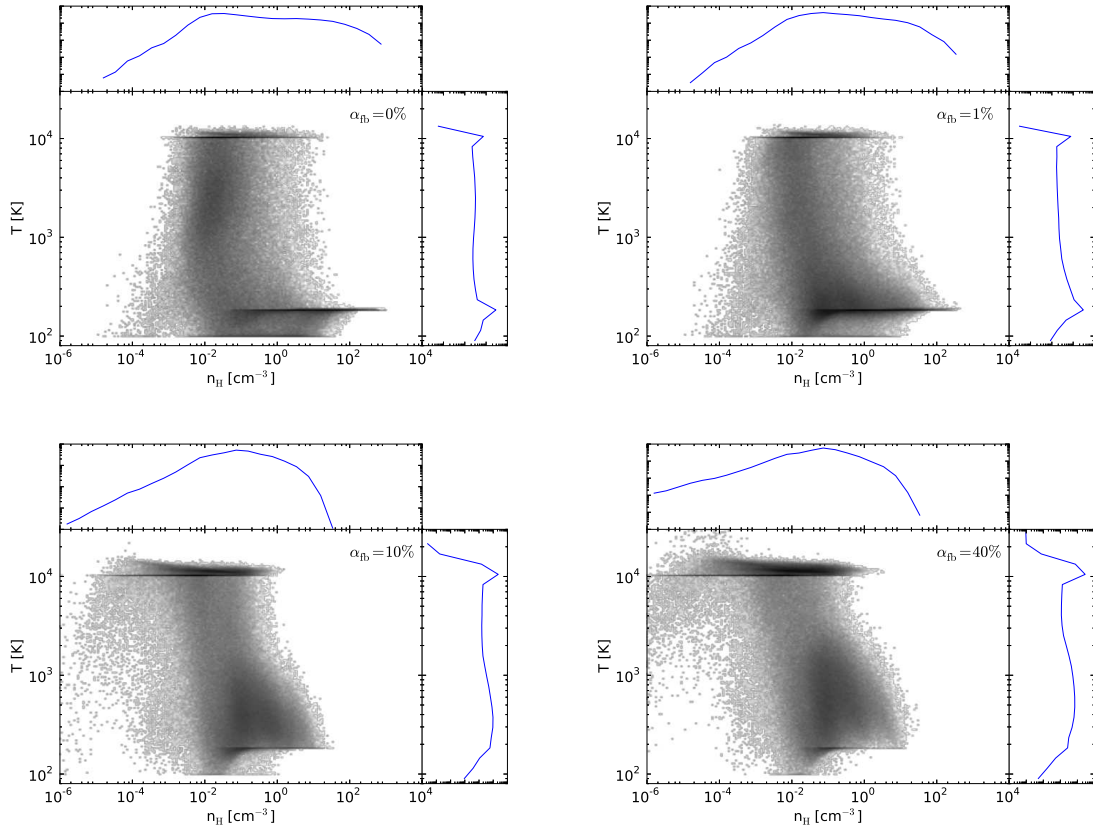


Figure 5.12: Temperature-density histograms of the gas in simulation with H_2 after 0.5 Gyr of evolution for the different feedback efficiencies. The 2D histograms and marginal 1D histograms are all mass weighted and normalised to unity.

Gas phases We separate the gas in two ranges of temperatures, below and above 1000 K. We study the evolution of the fractions of cold and warm gas (gas lying below or above this threshold) depending on the feedback efficiency, and with or without the inclusion of cooling by molecular hydrogen. The majority of star formation happens in the first Gyrs in all the simulations (especially when the feedback efficiency is low and stars form quickly), so we focus on this period and plot the cold gas fraction as a function of time on Figure 5.13 for two feedback efficiencies. All the gas is initially in the cold phase. For a given feedback efficiency,

the cold gas phase represents a much higher fraction of the gas if H_2 cooling is taken into account. Without H_2 , stars are formed from warmer and more diffuse gas, reducing the star formation efficiency. Feedback decreases the fraction of cold gas: the kinetic energy given to particles in dense star forming regions is transformed into thermal energy by pressure forces and viscosity, all the more as the feedback efficiency is high.

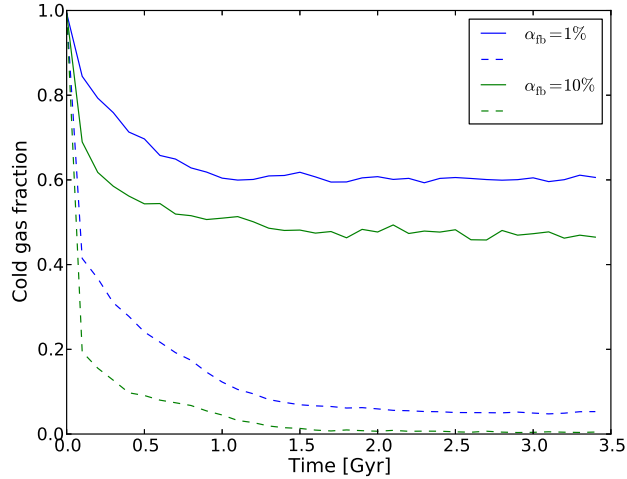


Figure 5.13: Fraction of cold gas as a function of time for two different feedback efficiencies $\alpha_{fb} = 1\%$ and $\alpha_{fb} = 10\%$. Solid lines: with H_2 . Dashed lines: without H_2 .

Volume density vs radius As we are especially interested in studying the state of the gas as a function of galactocentric radius, we plot the histograms of gas density versus radius in Figure 5.14 for the atomic and molecular simulations, after 0.5 Gyr of evolution. The gas exhibits density peaks at larger radii and has a mean higher density with the inclusion of H_2 , with gas denser than the star formation threshold even at large radii. The effect is especially visible for low feedback efficiencies, but is also visible for high feedback runs: a small fraction of the gas has densities higher than the threshold for star formation even at large radii.

4 Results on star formation

4.1 Gas mass depletion and total SFR

The effect of H_2 cooling on the star formation efficiency is visible in Figure 5.15 and Figure 5.16.

We plot in Figure 5.15 the time evolution of the total mass of gas present in the simulations. All the gas is originally in the disc but can leave it under the effect of gravitational heating or stellar feedback. The characteristic time of consumption of the gas increases with feedback efficiency because of the moderating effect of feedback on gas density, regulating

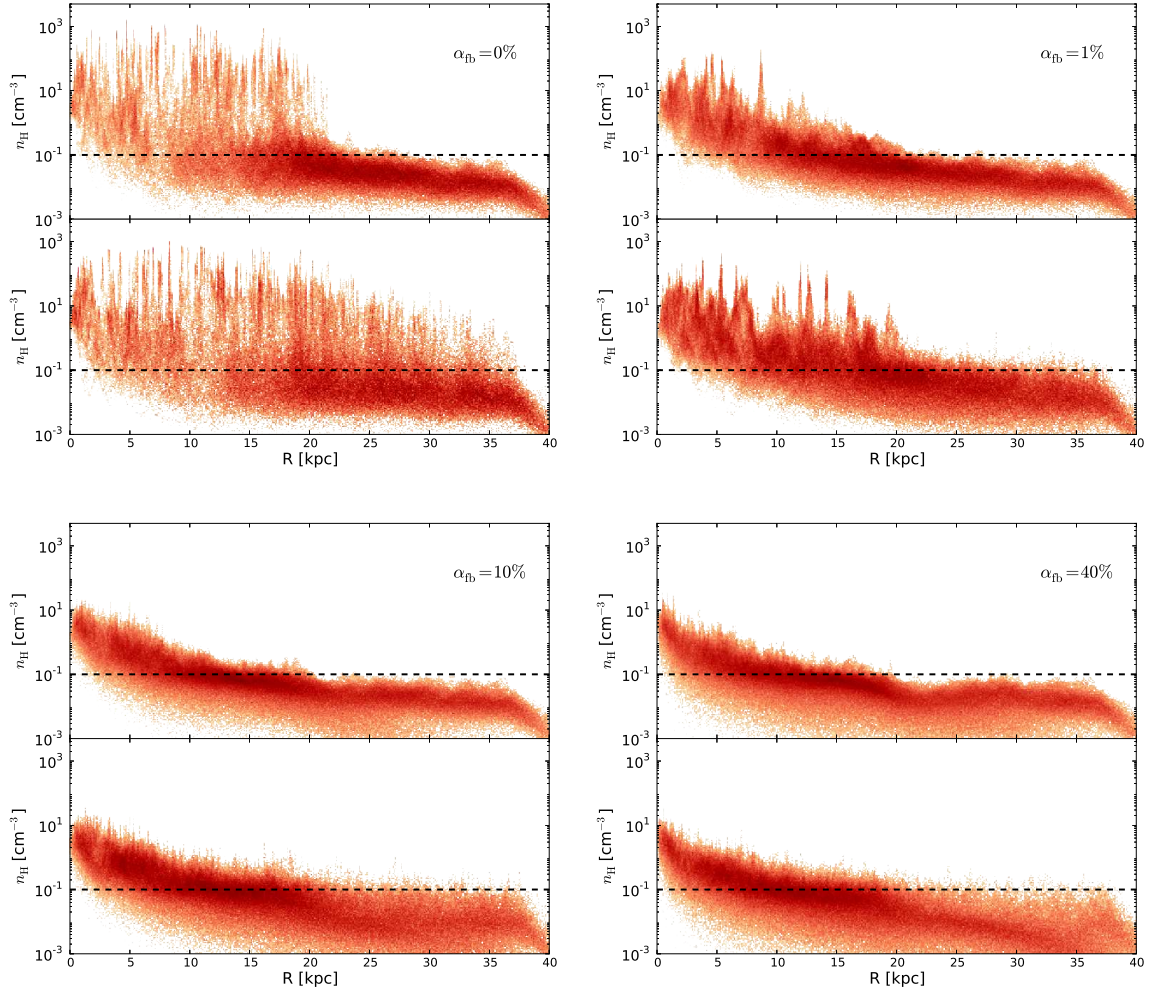


Figure 5.14: Hydrogen nuclei number density-galactocentric radius histograms after 0.5 Gyr of evolution. For each plot, the top subplot is a run with no H_2 and the bottom plot a run with H_2 . Horizontal black dashed line: threshold density for star formation.

star formation, and the curves have increasing horizontal asymptotes y -values. This is due to gas expelled from the disc, and also to the inability of the gas to reach the star formation threshold. The gas in the outer parts of the disc remains diffuse with almost no star formation in all cases, as the lower abundance of metals does not allow the gas to cool down enough to form stars. The depletion time of the gas decreases when molecular hydrogen cooling is included for all the considered feedback efficiencies. The total SFR is also shown.

4.2 SFR as a function of radius

Having inserted the formation time of stars in our simulation outputs, we can track star formation spatially. Our outputs are temporally spaced by 10 Myr. We define the SFR as being the mass of stars formed during 10 Myr divided by this time, which is similar to the star

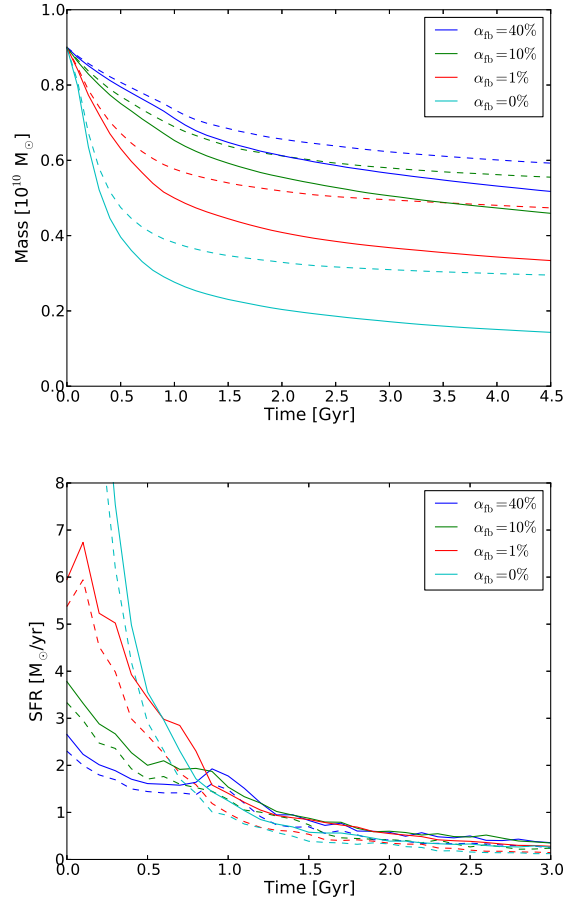


Figure 5.15: Top: evolution of the gaseous mass of the galaxy. Bottom: evolution of the corresponding SFRs (defined as the derivative of the left curves). For both plots, solid lines are for runs with H_2 and dashed lines for runs without H_2 .

formation rates obtained from observations in H_{α} . We plot the cumulative SFR averaged on the first Gyr as a function of radius for these two simulations and other feedback efficiencies in Figure 5.16, and we see that about the same amount of star formation occurs in the central parts, but molecular hydrogen starts playing a role at large radii. The difference occurs at a larger radius for the simulation with no feedback, which can be explained by the already high clumping in central parts of the disc, making star formation very efficient even without H_2 .

4.3 Stellar discs

Figure 5.17 shows the projected density of stars formed since the beginning of the simulation for $\alpha_{fb} = 1\%$: the disc of new stars is more extended if we include H_2 . There is a few stellar clumps, and also a very clear stellar bar that is maintained in the stellar component after a few Gyrs in both cases. Clumps of young stars can be seen on the density maps:

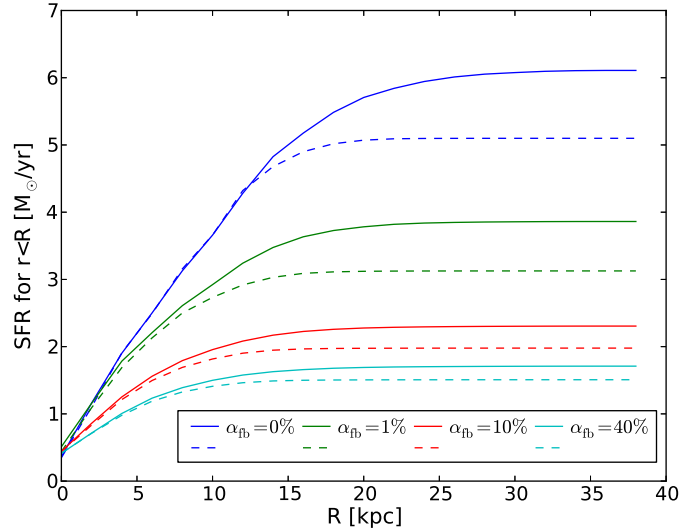


Figure 5.16: Cumulative star formation rate as a function of galactocentric radius, averaged on the first Gyr. Solid lines: run with H_2 . Dashed lines: run without H_2

they follow the gas clumps. These stellar clumps gradually lose energy and are eventually absorbed by the central bar. After 3 Gyr of evolution, a peanut-shaped instability of the bar can be seen on edge-on views of young stars in both cases.

The new stars are only a small mass fraction of the total stars (at most 16% if all the gas were turned into stars). On Figure 5.18, the corresponding total stellar components are shown: old disc and bulge stars and new stars. They are similar in both runs.

4.4 Kennicutt-Schmidt diagrams

We further study the star formation by drawing Kennicutt-Schmidt (KS) diagrams representing the surface density of SFR as a function of the gas surface density. As we are limited in mass resolution for star formation (stellar particles of a fixed mass of $\sim 10^4 M_\odot$ are created stochastically, completely differently from some smooth star formation), in order to have a significant amount of data to study, we add data points corresponding to 50 snapshots, from $t=200$ Myr to $t=700$ Myr.

We use a polar grid with a given number n_R of bins in cylindrical radius R and a given number n_θ of bins in azimuthal angle θ ($n_R=40$ and $n_\theta=20$ for the results presented here). Using this kind of grid allows for a more uniform signal/noise repartition than with an orthogonal grid, and optimizes the number of new stars per cell.

On Figures 5.19 and 5.20, we have plotted KS diagrams for simulations without feedback, and with different feedback efficiencies. These can be compared with [Agertz et al. \(2012\)](#) plots of azimuthally averaged KS diagrams of disc galaxies for different feedback intensities. Very similarly, we observe a global diminution of the SFR surface density when we increase the

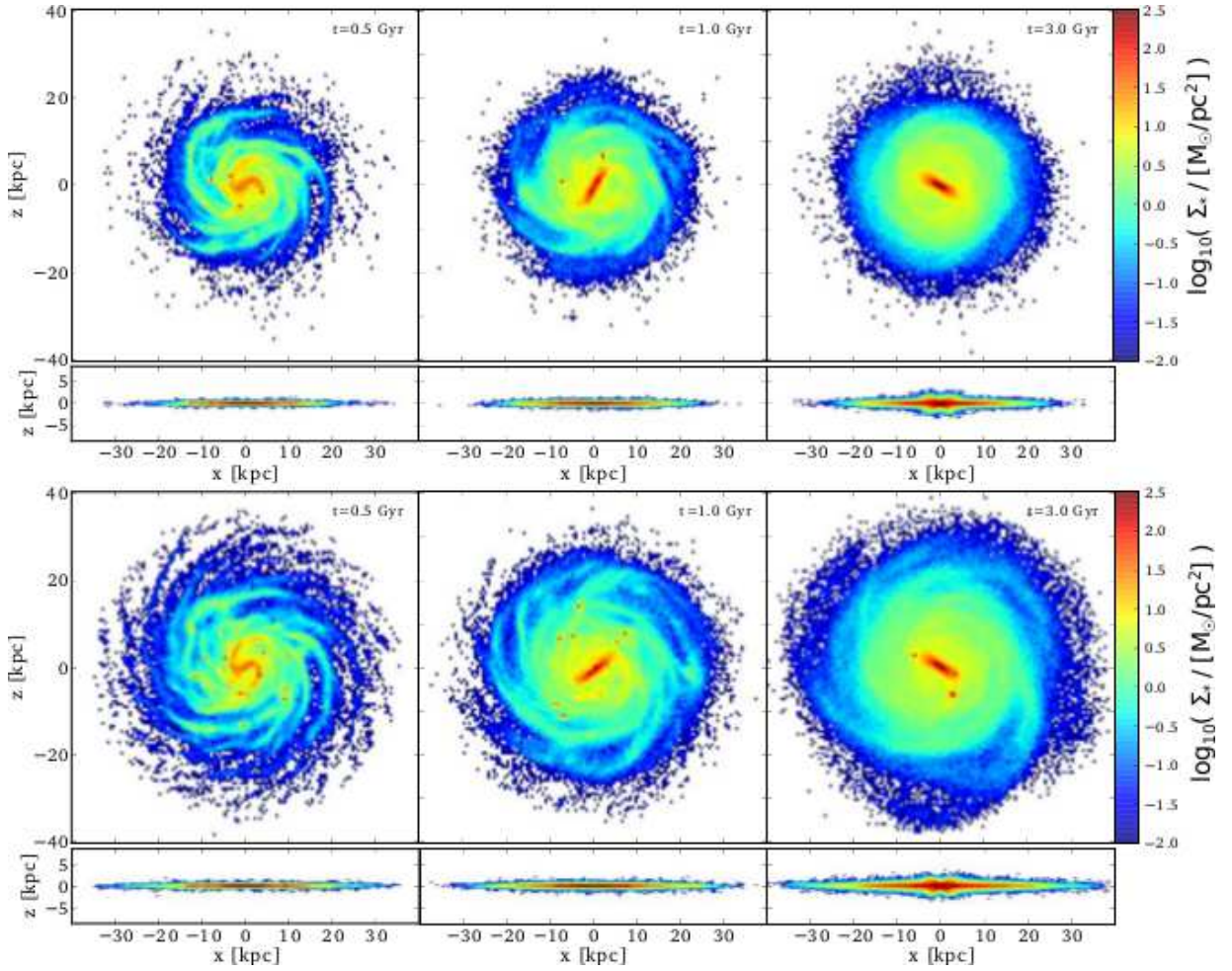


Figure 5.17: Projection of the density of stars formed during the simulations after 0.5 Gyr, 1 Gyr and 3 Gyr of evolution. Top row: feedback efficiency $\alpha_{\text{fb}} = 1\%$ and no H_2 . Bottom row: feedback efficiency $\alpha_{\text{fb}} = 1\%$ and H_2 .

feedback strength. The figure quantifies how, on average, for the same gas surface densities, the SFR is lower with higher feedback. The feedback makes the gas more diffuse and destroys clumps. Two cells containing the same amount of gas but different fractions of diffuse gas (cells are larger than the clumps size), will have different star formation efficiency. This also explains the smaller scatter in the simulations with feedback: as the gas is more homogeneous, the relation between surface densities of SFR and gas is better determined.

In Figures 5.19 and 5.20, lines of constant gas depletion time are indicated. The gas depletion time is defined as $t_{\text{dep}} = \frac{\Sigma_{\text{Gas}}}{\Sigma_{\text{SFR}}}$. It can be seen that the high SFR and gas surface density regions of the galaxies have a depletion time as low as a few hundreds of Myrs in the simulations with no or little feedback, while the low SFR and density regions have depletion times up to 10 Gyr. The outer parts of the disc with a low surface density form stars much less efficiently than the central parts.

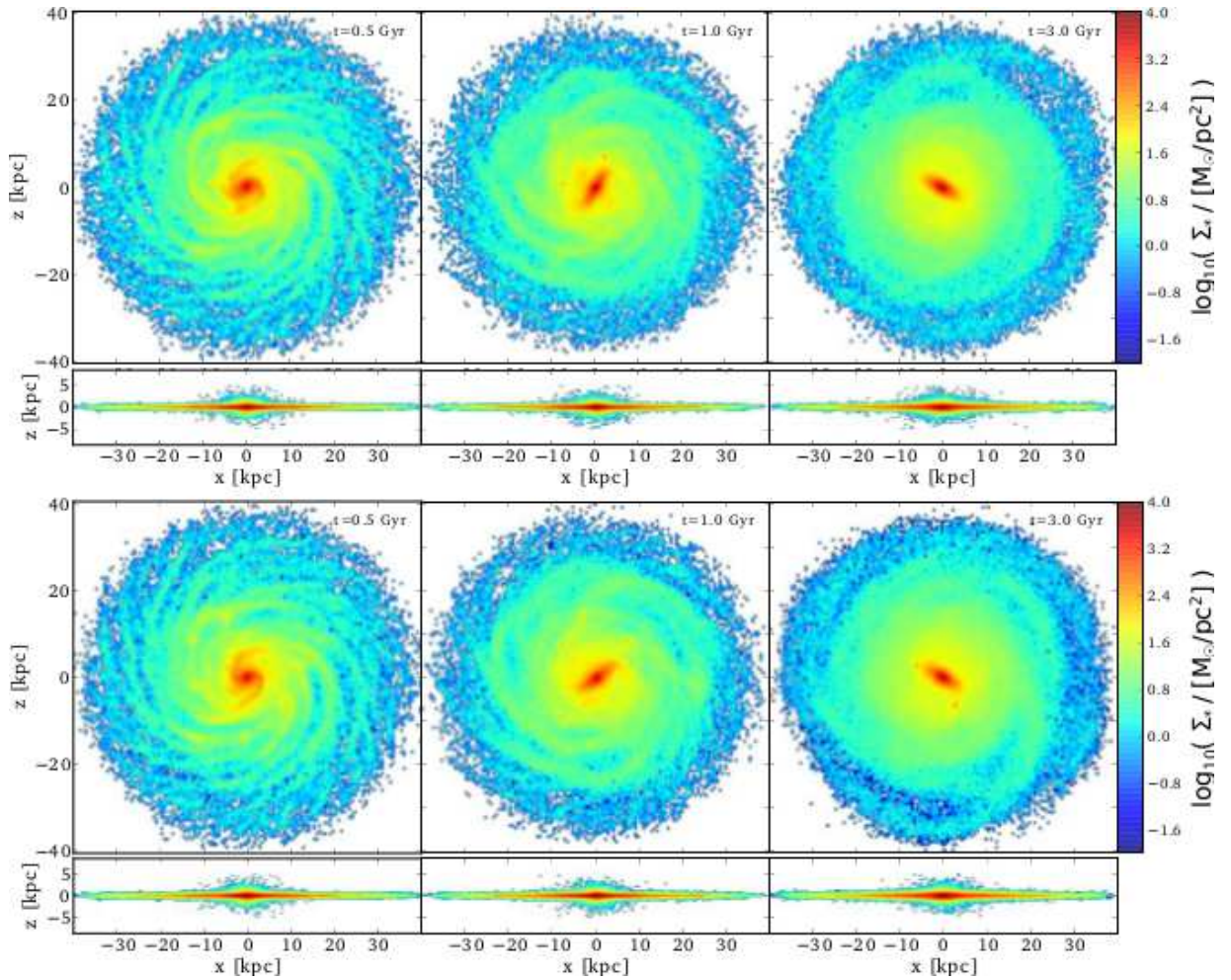


Figure 5.18: Projection of the density of all the stars after 0.5 Gyr, 1 Gyr and 3 Gyr of evolution. Top row: feedback efficiency $\alpha_{\text{fb}} = 1\%$ and no H_2 . Bottom row: feedback efficiency $\alpha_{\text{fb}} = 1\%$ and H_2 .

We also see a difference for low surface densities between atomic and molecular simulations. The SFR is varying more linearly with molecular gas than with atomic gas. And the low surface density regions form stars more efficiently with molecular gas. This is explained by the fact that H_2 cooling allows the gas to be locally denser. It especially allows it to be more concentrated in the disc plane as can be checked in the edge-on projections. Then the gas is denser in volumic density, and forms stars more efficiently, at a given surface density.

For simulations including H_2 , the SFR is shown separately as a function of atomic and molecular components, on the bottom of Figures 5.19 and 5.20. The atomic hydrogen surface density is confined to low values for our galaxies and the SFR-HI diagrams show a large scatter because HI is too diffuse to track the star forming gas. The fact that H_2 is a better tracer of star formation is also found in observations of nearby galaxies (e.g. Bigiel et al. 2008).

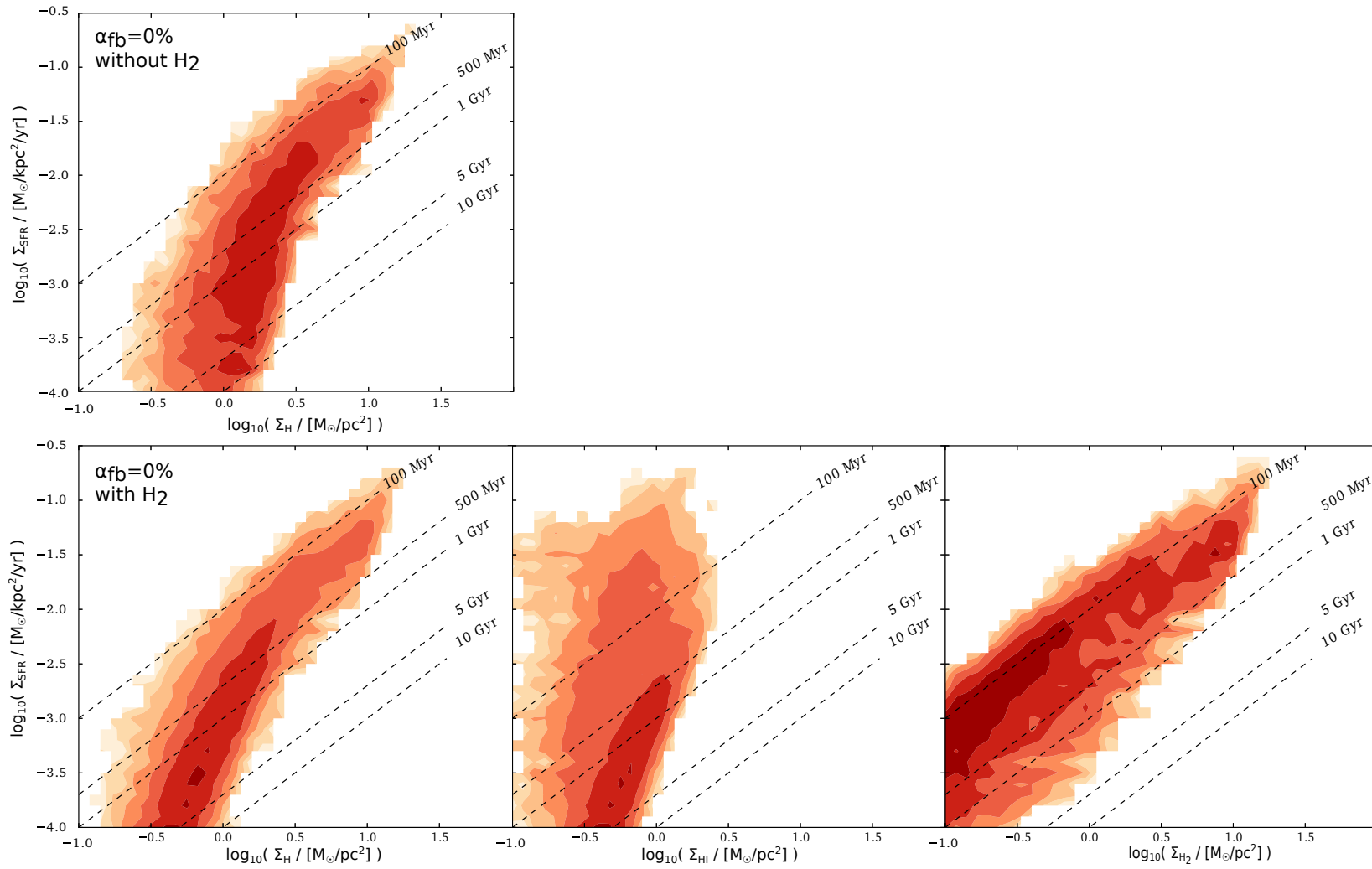


Figure 5.19: K-S diagrams for runs without feedback. Top row: simulation without H_2 . Bottom row: simulation with H_2 . Left: SFR vs total hydrogen gas surface density. Middle: SFR vs the HI only surface density. Right: SFR vs the H_2 surface density.

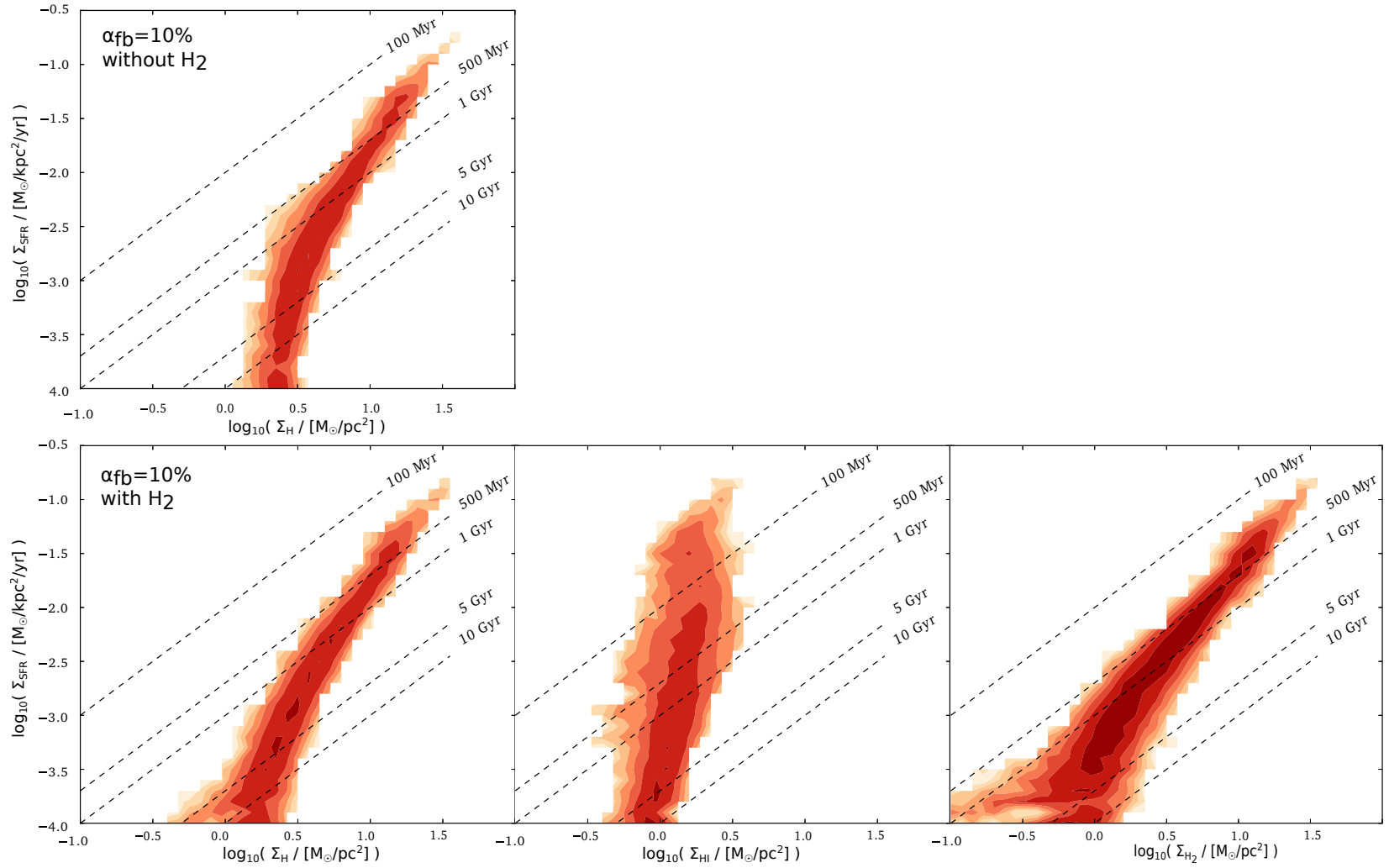


Figure 5.20: K-S diagrams for runs with a feedback efficiency $\alpha_{\text{fb}} = 10\%$. Top row: simulation without H_2 . Bottom row: simulation with H_2 . Left: SFR vs total hydrogen gas surface density. Middle: SFR vs the HI only surface density. Right: SFR vs the H_2 surface density.

4.5 Gas density profile variation

The galaxies we have considered have a rather low gas surface density. We also run simulations with smaller characteristic radii, and therefore higher surface densities. Figure 5.21 displays the surface density for a Miyamoto-Nagai gas radius r_g of 3.6 kpc. The transition radius between H_2 dominated and HI dominated regions, the radius at which $\Sigma_{\text{H}_2} = \Sigma_{\text{HI}}$, has then a value similar to the average observed by Bigiel & Blitz (2012) (their average value for nearby spiral galaxies observations is $14 \text{ M}_\odot/\text{pc}^2$). Previous galaxies belong to the lower surface density group observed by Bigiel & Blitz (2012).

The effect of H_2 cooling is reduced in these galaxies with higher surface density, since a larger fraction of the gas belong to the central regions, with much more efficient star formation than the outer parts. H_2 cooling is more important when there is more gas in the metal poor outer regions.

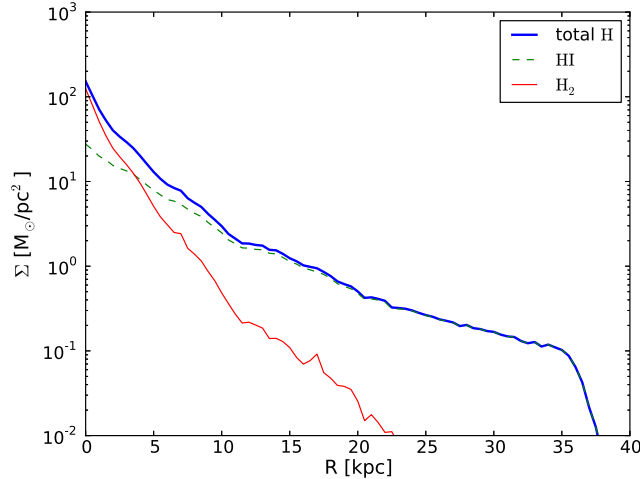


Figure 5.21: Radial distribution of the surface density of H_2 , atomic gas HI and total hydrogen gas after 100 Myr for $\alpha_{\text{fb}} = 40\%$ and a $\chi \times 500$ UV scaling factor.

5 Vertical structure of the disc

The inclusion of molecular hydrogen has a significant impact on the vertical structure of the disc, firstly because the cold and dense gas concentrates in the disc middle plane, and secondly because of the impact of gas clumping on the distribution of feedback energy.

(Christensen et al. 2012b,a) include non-equilibrium formation of H_2 , self-shielding and dust shielding of both HI and H_2 in galaxies extracted from cosmological simulations and explore the influence of including H_2 formation, for a fixed feedback efficiency. Similarly to their results, we find that the introduction of H_2 makes the outer parts of discs denser.

H_2 cooling also enables the gas to be more efficiently expelled from the plane, since the

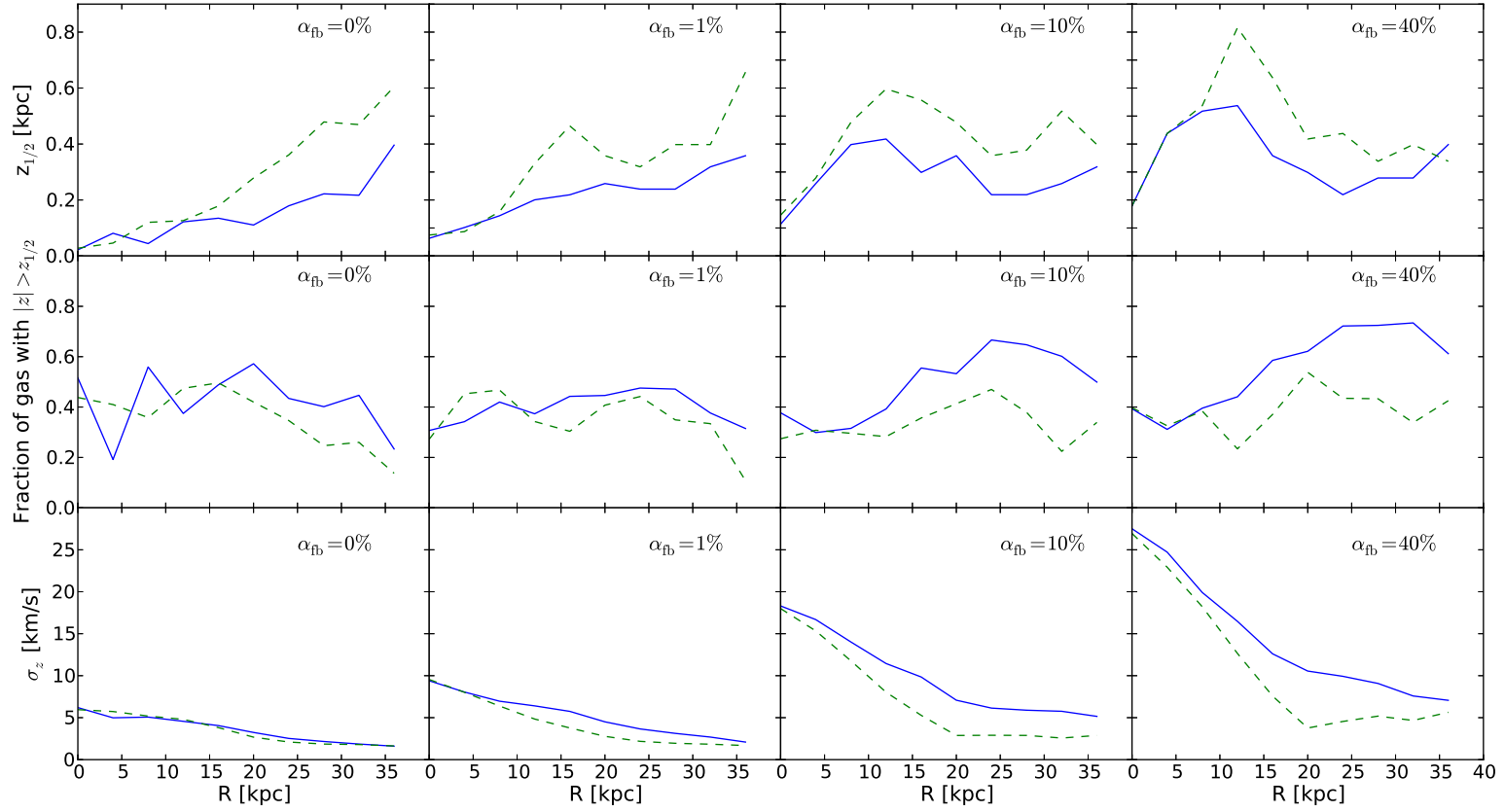


Figure 5.22: Vertical structure of the gas. First row: characteristic gas height $z_{1/2}$ as a function of galactocentric radius after 0.5 Gyr of evolution. Second row: fraction of gas beyond the characteristic height. Third row: vertical velocity dispersion. Solid lines: runs with H_2 . Dashed lines: runs without H_2

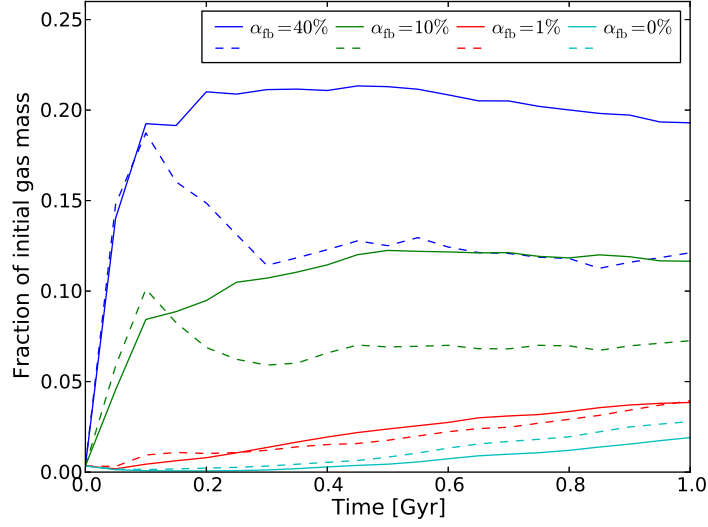


Figure 5.23: Fraction of gas beyond 1 kpc from the disc plane. Solid lines are runs with H_2 and dashed ones are runs without H_2 . Blue lines: no feedback. Green lines: $\alpha_{\text{fb}} = 10\%$, Red lines: $\alpha_{\text{fb}} = 40\%$

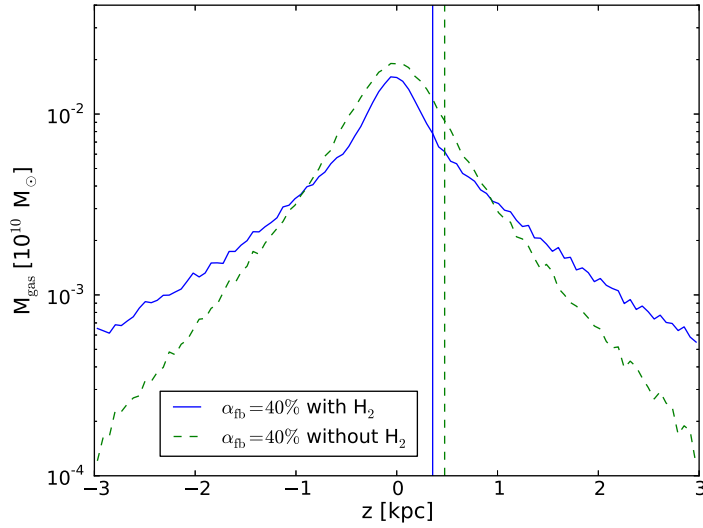


Figure 5.24: Vertical mass profile of the disc for radii $R > 15$ kpc for runs with $\alpha_{\text{fb}} = 40\%$. Solid line: run with H_2 . Dashed line: run without H_2 . The two vertical lines mark the characteristic vertical heights $z_{1/2}$.

feedback has a stronger effect in dense regions: in our feedback scheme, particles get velocity kicks weighted by the SPH kernel, so that the kicks are larger for particles closer to the new stellar particles. We have performed simulations with various feedback efficiencies, helping to

check this effect. Figure 5.23 shows the fraction of gas that is expelled further than 1 kpc from the disc (or radially further than 60 kpc from the centre of the galaxy): without feedback, the gas is only gravitationally heated and the effect of denser gas and higher clumping factor due to H_2 makes the fraction of gas leaving the disc smaller than for a purely atomic hydrogen gas. However, with feedback, there is a higher fraction of gas outside the disc when H_2 is included. This is because the higher concentration of the gas makes the feedback more efficient. In our simulations, the effect is especially striking in the outer parts of discs when H_2 formation is taken into account, as the vertical restoring force is lower there.

We checked that the vertical density distribution is consistent with both a more concentrated disc and a higher fraction of gas leaving the disc. Figure 5.24 shows the vertical mass profile of the gas at large radii for $\alpha_{\text{fb}} = 40\%$: the gas is more concentrated in the disc plane, but the distribution has higher density “tails” when more efficient feedback in denser regions allows the gas to be expelled from the disc. Figure 5.24 shows the characteristic height $z_{1/2}$ of the gas, the distance from the disc plane for which the density equals half of the central density, as a function of radius for the various simulations. Especially at large radii, the characteristic height is lower for simulations with H_2 for all feedbacks as H_2 concentrates the gas in the middle plane. The fraction of gas beyond this height however increases with the feedback efficiency at large radii when H_2 is taken into account, as gas is then efficiently expelled by feedback. Without feedback, some difference remains, probably due to gravitational heating produced by a higher clumping. We see indeed a slight difference in vertical velocity dispersion.

In our simulations, the H_2 gas disc remains very thin, as can be seen on Figure 5.11. The thick discs that are obtained are composed of atomic hydrogen, because the density is too low for H_2 shielding to be efficient. Some observations however indicate the presence of thick H_2 discs, for example in M51 (Pety et al. 2013). Our result on the thinness of the molecular hydrogen disc could change in simulations of higher resolution in which clumps could be allowed to form further away from the disc plane.

6 Variations of parameters or baryonic physics methods

In this last section, we present some variations around the former simulations. Simulations are sensitive to the adopted models and algorithms.

6.1 Resolution

We ran simulations with twice as many and twice as few particles (changing the number of all particles: gas, stars and dark matter) for a feedback efficiency $\alpha_{\text{fb}} = 10\%$. The softening length is usually taken as:

$$\epsilon \propto N^{-1/3} \tag{5.14}$$

with N the total number of particles. This makes it change according to the change in mean inter-particle distance. We thus used $\epsilon = 130$ pc for the low-resolution run and $\epsilon = 80$ pc for the high-resolution run. We keep all the star formation parameters constant.

We represent on Figure 5.25 the gas mass depletion and SFR for the different runs. More stars are formed when we increase the resolution. We have not adapted the star formation efficiency per free-fall time c_* , which maximises the differences between the different runs.

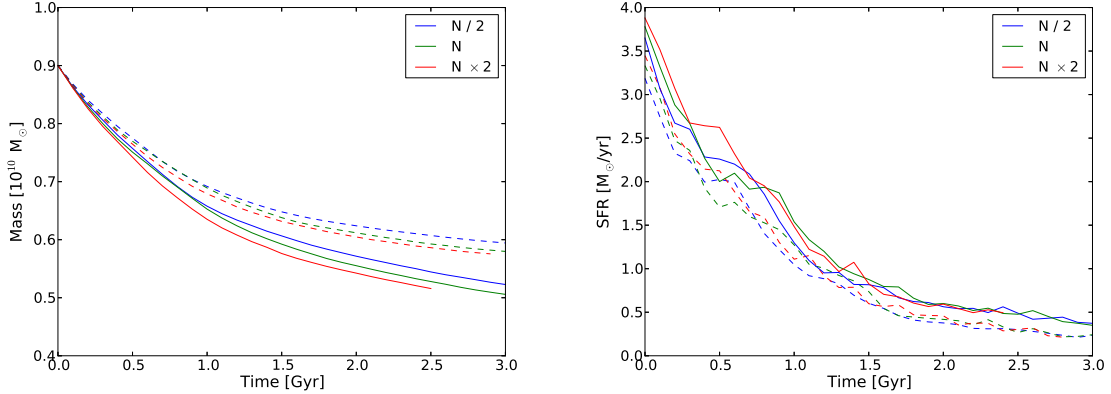


Figure 5.25: Left: evolution of the gaseous mass of the galaxy for $\alpha_{\text{fb}} = 10\%$. Right: evolution of the corresponding SFRs (defined as the derivative of the left curves). For both plots, solid lines are for runs with H_2 and dashed lines for runs without H_2 .

We plot on Figure 5.26 the global H_2 mass fraction for these simulations. The parameters of the H_2 fraction recipe are the same for all simulations. We see the fraction increases with decreasing resolution. This can be partly due to the slightly reduced SFR when resolution decreases, and also to the estimation of the column density. For high resolution runs having lower smoothing lengths, this column density, inversely proportional to the gradient of the density computed, is smaller than for low resolution runs. As H_2 is less shielded, its fraction is reduced.

The number density PDFs for runs either without any H_2 or with H_2 , keeping the same parameters in the H_2 fraction recipe as in our fiducial simulation, is shown on Figure 5.27. They are similar for all the resolutions.

6.2 Threshold density for star formation

The threshold density for star formation has a strong impact on the density distribution of the gas. If this threshold is augmented, gas reaches higher densities than if it were allowed to be converted into stars sooner, and the obtained ISM can be much more heterogeneous. While we do not have a very large particle number and may be subject to resolution artefacts, we perform simulations with a threshold density 100 times higher than our fiducial one: we set $n_{\text{Hmin}} = 10 \text{ cm}^{-3}$ and obtain the surface density maps such as the ones shown on Figure 5.28.

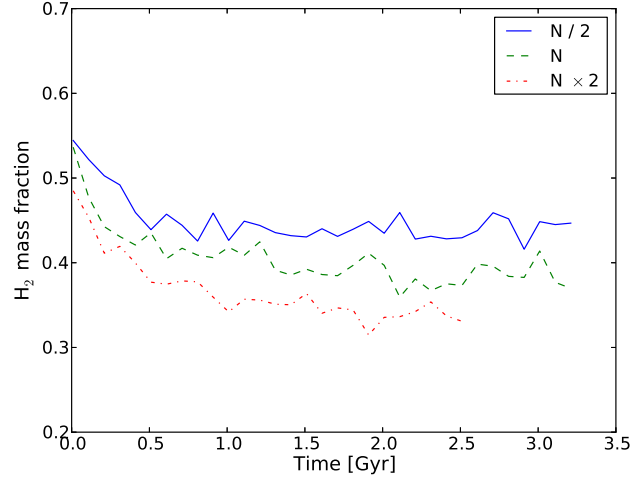


Figure 5.26: Global H_2 mass fraction versus time for $\alpha_{\text{fb}} = 10\%$ and different resolutions.

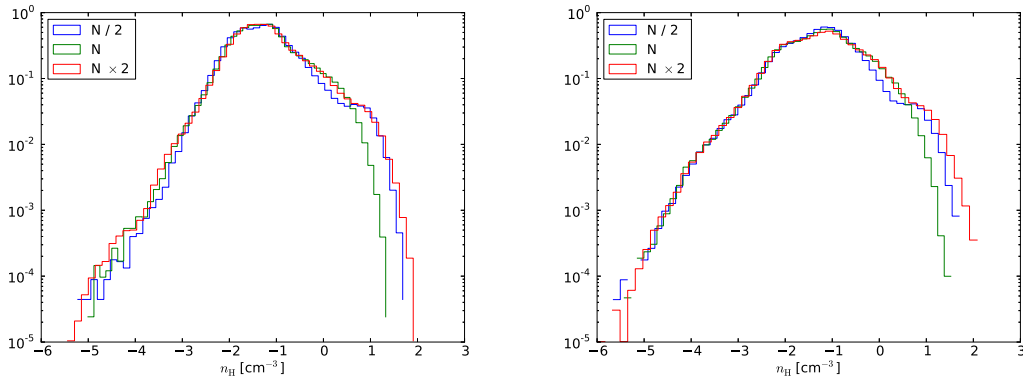


Figure 5.27: Hydrogen nuclei number density PDFs (mass-weighted and normalised to unity). Left: runs with no H_2 . Right: runs with H_2 .

The gas is indeed very contrasted in density, as can also be seen on Figure 5.29.

We observe that, after a few Gyrs, more of the total gas is depleted for the case without feedback or with a low feedback efficiency $\alpha_{\text{fb}} = 1\%$ than with our fiducial threshold $n_{\text{Hmin}} = 10^{-1} \text{ cm}^{-3}$ (see Figure 5.30 compared to Figure 5.15). This is due to the higher clumping efficiency and also possibly to the lower effect of stellar feedback in very dense regions for the case $\alpha_{\text{fb}} = 1\%$. However, the depletion is lower for the two high feedback efficiency cases, because the gas reaches densities high enough for star formation more difficultly, and is strong enough to lower the density below the star formation threshold. The SFRs on the right panel of Figure 5.30 exhibit peaks hundreds of Myrs after the beginning of the simulations, contrarily to what was observed for a lower threshold for star formation (see figure 5.15). This can be explained by the time needed to reach densities higher than the threshold so as to form stars. The SFR peaks happen all the later as the feedback efficiency

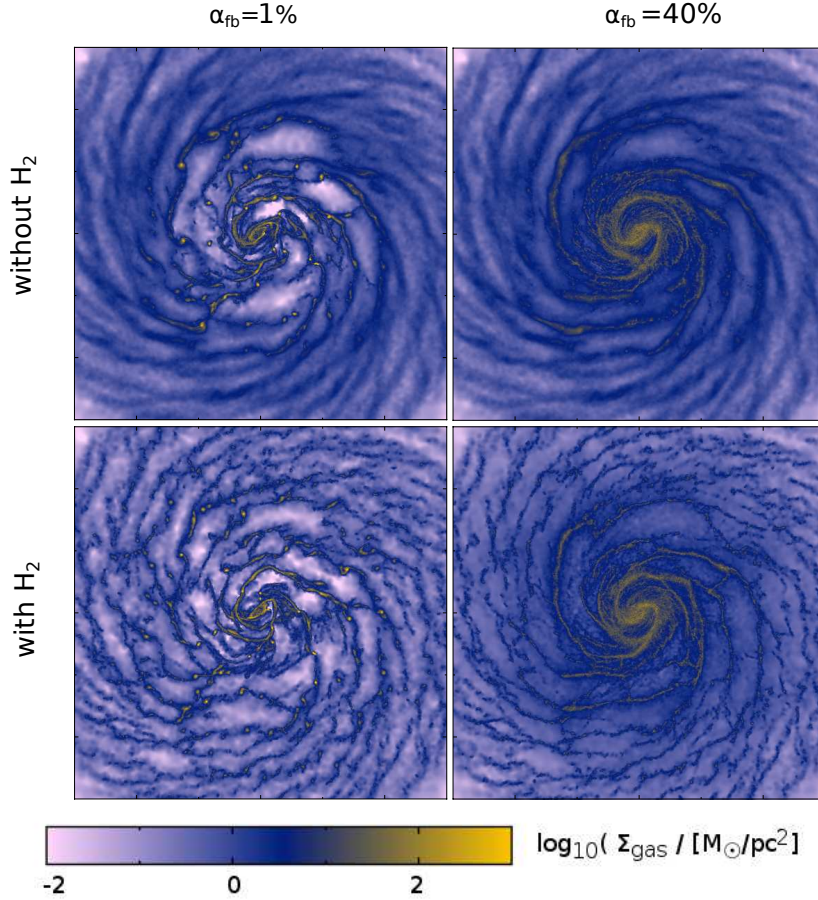


Figure 5.28: Projections of the gas density at $t=0.5$ Gyr for runs with $n_{\text{Hmin}} = 10 \text{ cm}^{-3}$. Box sizes are [30 kpc x 30 kpc].

is higher, because in high feedback cases, the little initial amount of star formation prevents the gas more efficiently from clumping.

6.3 Recipe for feedback

As we mentioned in 6 of Chapter 4, we tried several techniques to input energy from SNII explosions to the surrounding gas of new stellar particles.

We compare the results of our simulation with a kinetic feedback of efficiency $\alpha_{\text{fb}} = 10\%$ and molecular hydrogen to two simulations with the same feedback efficiency and the same parameters for the computation of the molecular hydrogen fraction but other feedback methods.

A simulation is run with gas particles dynamically decoupled for at most 10 Myr once they are given a velocity kick. They can be re-coupled either once this time has passed or once their density has become lower than 10^{-1} cm^3 (following [Springel & Hernquist \(2003\)](#)). A snapshot is shown on the middle panel of Figure 5.31.

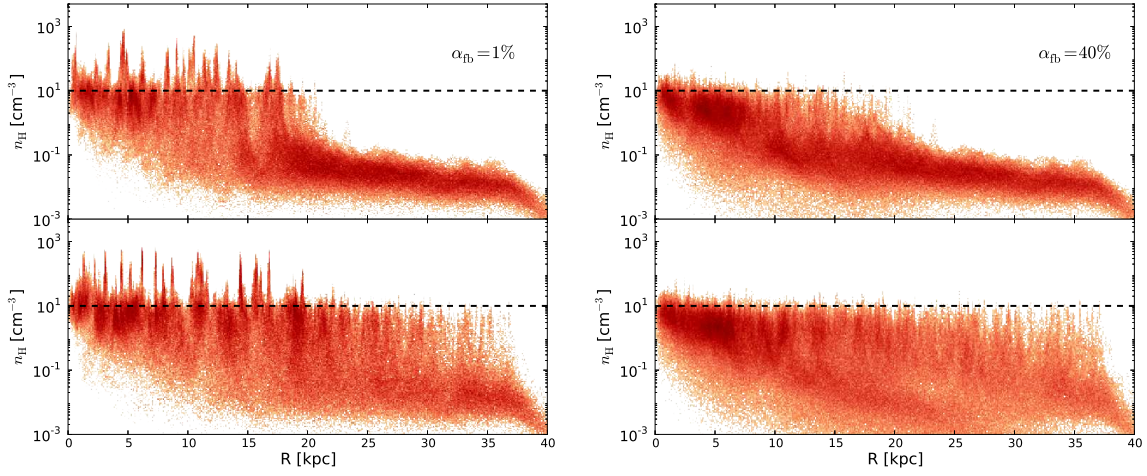


Figure 5.29: Hydrogen nuclei number density-galactocentric radius histograms after 0.5 Gyr of evolution. For each plot, the top subplot is a run with no H_2 and the bottom plot a run with H_2 . Horizontal black dashed line: threshold density for star formation.

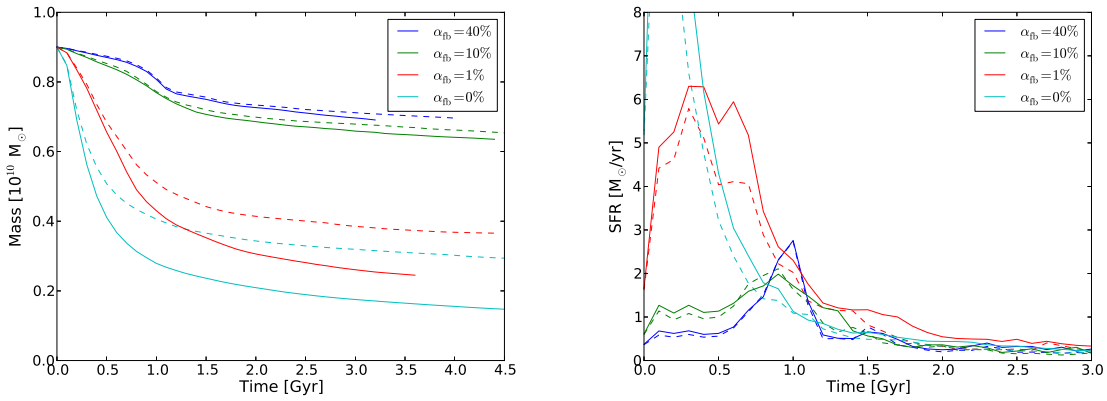


Figure 5.30: Left: evolution of the gaseous mass of the galaxy. Right: evolution of the corresponding SFRs (defined as the derivative of the left curves). For both plots, solid lines are for runs with H_2 and dashed lines for runs without H_2 .

Another simulation is run with a thermal feedback with cooling stopped for 30 M_{yr} each time a particle is affected by feedback. A snapshot is shown on the right panel of Figure 5.31.

The gas mass depletion and SFRs are shown on Figure 5.32. The star formation is sensitive to the adopted method. Both the decoupling case and thermal case are more efficient at preventing clumping leading to star formation than our fiducial scheme.

We also notice that our scheme, while impacting the star formation if the feedback efficiency is modified, keeps the gas dynamically cooler than other schemes. The gas disc we obtain for these other methods are more similar to the stellar discs we have shown. In the decoupling case, many gas particles are decoupled from hydrodynamics and therefore do not

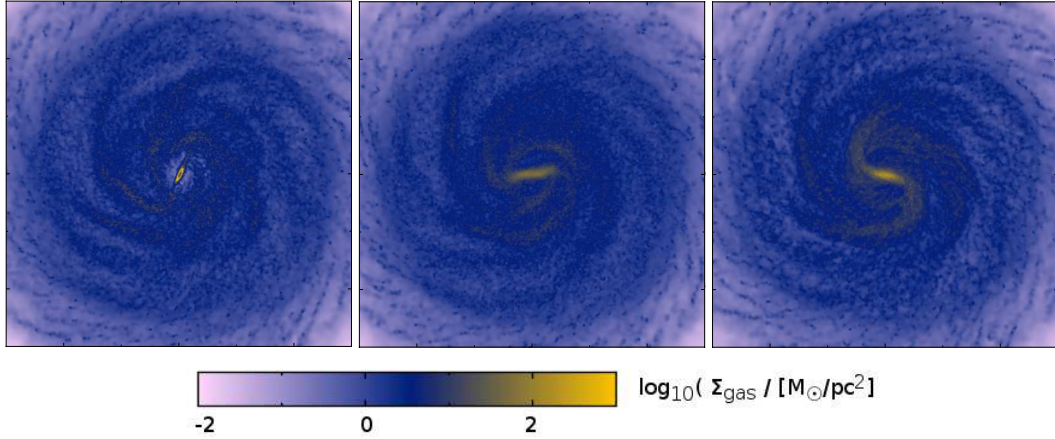


Figure 5.31: Projections of the gas density at $t=1$ Gyr for runs with $\alpha_{\text{fb}} = 10\%$. Left: simple kinetic feedback. Middle: kinetic feedback with decoupled particles. Right: Thermal feedback. Box sizes are $[30 \text{ kpc} \times 30 \text{ kpc}]$.

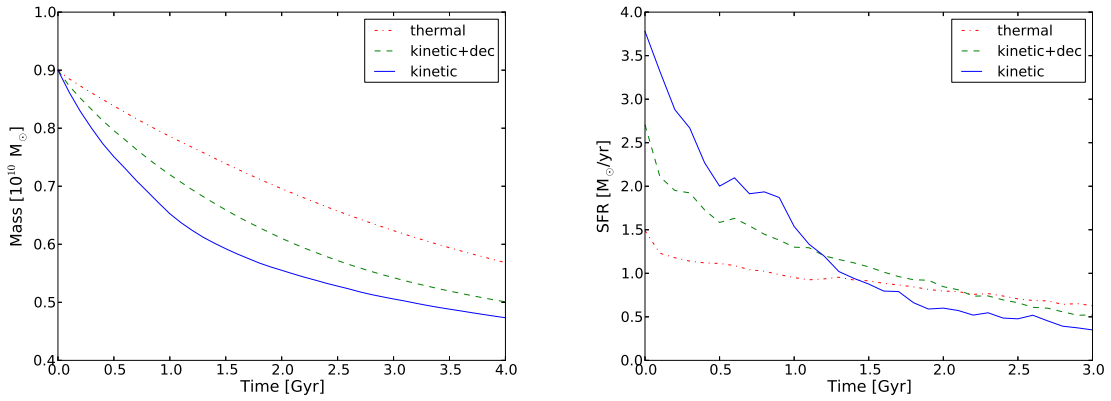


Figure 5.32: Left: evolution of the gaseous mass of the galaxy. Right: evolution of the corresponding SFRs (defined as the derivative of the left curves). For both plots, solid lines are for runs with H_2 and dashed lines for runs without H_2 .

experience hydrodynamical forces and viscosity while in the thermal feedback case, particles affected by feedback have a high pressure for a while. The temperature-density diagram on Figure 5.33 shows the dense gas is partly in a hot phase, above 10^4 K , while in our fiducial kinetic feedback scheme, dense gas was mostly cold (see the bottom-left panel of Figure 5.7). This hot gas is the gas affected by feedback and that has its cooling stopped. The high pressure reduces the clumping of the gas, hence the smoother aspect.

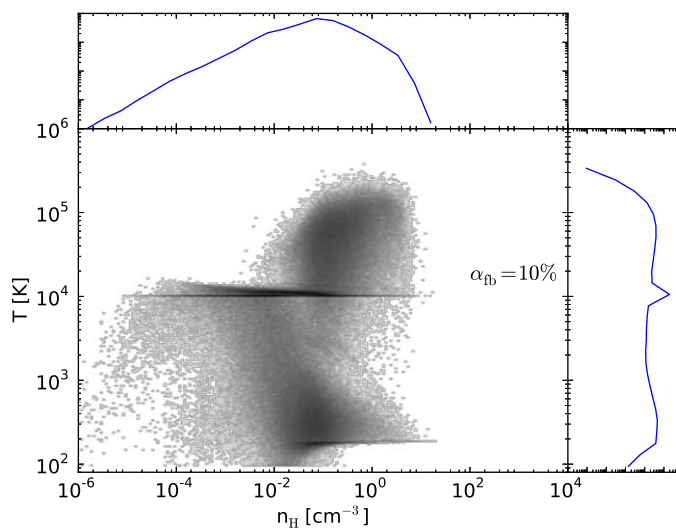


Figure 5.33: Temperature-density histogram of the gas in simulation with H_2 after 0.5 Gyr of evolution for the different feedback efficiencies. The 2D histograms and marginal 1D histograms are mass weighted and normalised to unity.

Chapter 6

Conclusion and perspectives

To explore the influence of baryonic physics on the evolution of spiral discs, we have implemented some models and algorithms for cooling, determination of the molecular hydrogen fraction, star formation and SNII feedback in Gadget-2.

The cooling functions we use include cooling by metals, for temperatures as low as 100 K, and cooling by H_2 due to collisions with H, He and other H_2 molecules. The determination of the H_2 density is inspired by the work of [Krumholz et al. \(2008, 2009b\)](#); [McKee & Krumholz \(2010\)](#), using the stellar UV flux from young stars. Star formation is done with a stochastic method, and our fiducial feedback from SNII is done by imposing velocity kicks to particles surrounding newly formed stellar particles. The exact models chosen for baryonic physics is found to have a significant impact on the physical state of the gas and star formation.

The efficiency of the kinetic feedback was varied in simulations including cooling by atomic/ionised gas and/or molecular hydrogen. We find that including molecular hydrogen allows some slow star formation to occur in the low metallicity outer parts of galaxies for all feedback efficiencies. Correlating SFR and gas surface density, it is found that molecular gas is a much better tracer of star formation than atomic gas, as is also observed in nearby galaxies.

Molecular hydrogen influences the vertical structure of the discs, especially when there is some strong stellar feedback: H_2 makes the gas more concentrated in the middle layer of the disc plane, but the gas is also more susceptible of being ejected far from the disc, due to the higher efficiency of feedback in high density regions. This gives rise to thick gas discs.

If gas is accreted by the outer discs, molecular hydrogen may help store some cold gas with a low star formation efficiency. It is thus interesting to perform simulations with either some gas accretion, or isolated disc simulations with a varying fraction of gas in the external disc. We are currently pursuing this second possibility. We change the fraction of gas in the outer disc and study the possible impact on the structure of the disc and star formation. The gas fraction with respect to dark matter can indeed be modified while keeping the same rotation curve, using the degeneracy between gas and dark matter that allows for a high fraction of

unobservable cold gas, possibly cooled by molecular hydrogen, at large radii (Hoekstra et al. 2001). Revaz et al. (2009b) studied the effect of additional dark baryons to the morphology and dynamics of discs but without detailed cooling and without stellar feedback. It is also possible to study the impact of the variation in the gas fraction on the dynamical state of the discs, especially on resonances using a spectral analysis of trajectories based on Binney & Spergel (1982).

Appendix A

Influence of baryonic physics in galaxy models: a semi-analytic treatment of the molecular component

Some of the results presented in Chapter 4 have been submitted to A&A, <http://arxiv.org/abs/1212.4433>.

Abstract

Recent work in galaxy formation has enlightened the important role of baryon physics, to solve the main problems encountered by the standard theory at the galactic scale, such as the galaxy stellar mass functions, or the missing satellites problem. The present work aims at investigating in particular the role of the cold and dense molecular phase, which could play a role of gas reservoir in the outer galaxy discs, with low star formation efficiency. Through TreeSPH simulations, implementing the cooling to low temperatures, and the inclusion of the molecular hydrogen component, several feedback efficiencies are studied, and results on the gas morphology and star formation are obtained. It is shown that molecular hydrogen allows some slow star formation to occur in the outer parts of the discs. This dense and quiescent phase might be a way to store a significant fraction of dark baryons, in a relatively long time-scale, in the complete baryonic cycle, connecting the galaxy discs to hot gaseous haloes and to the cosmic filaments.

Appendix B

Graph of the functions of the code

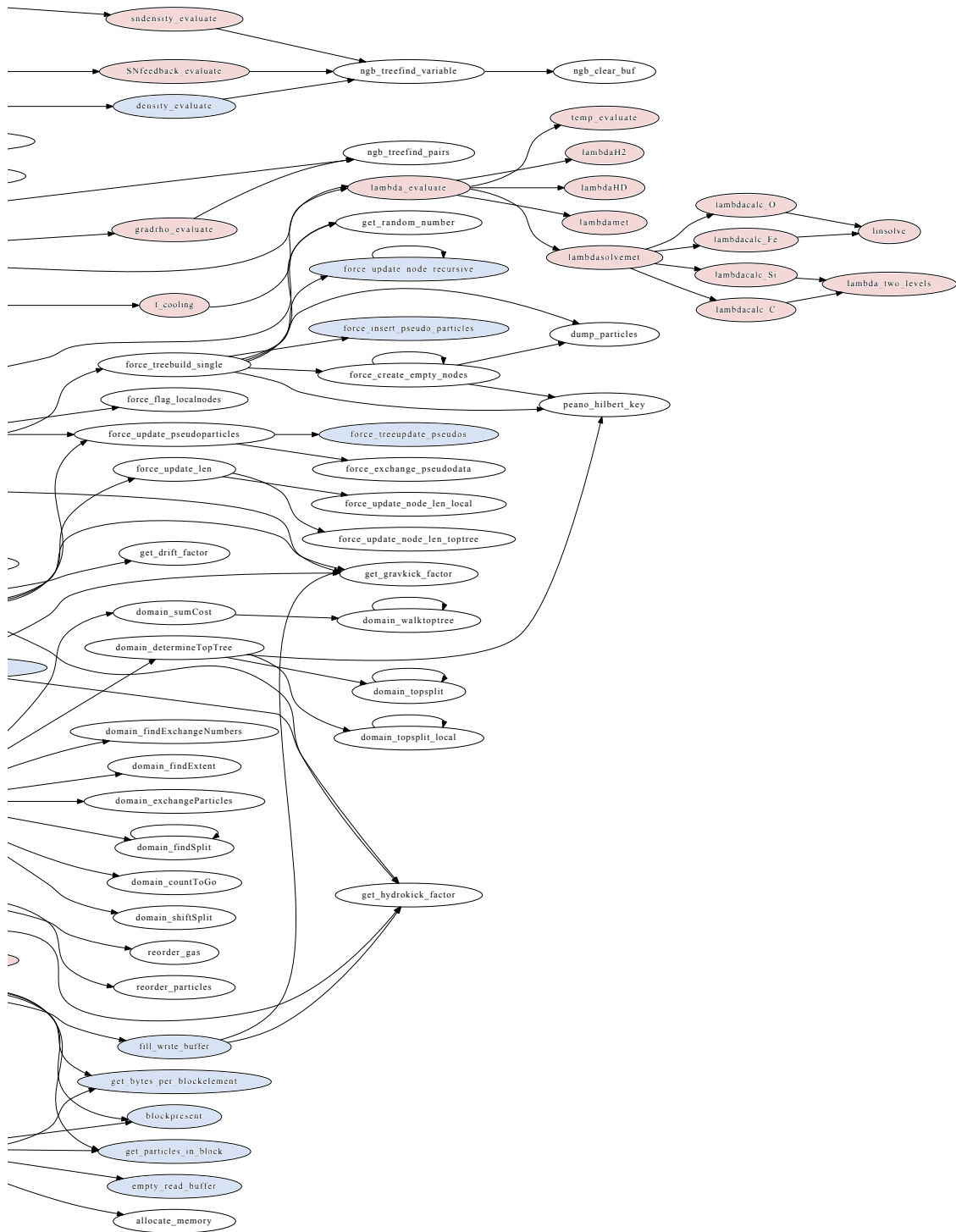


Figure B.2: Right part of the graph of functions of Gadgets-2 and their calls. Added functions are coloured in red, while modified functions are coloured in blue. A few functions have been taken off for simplicity. Graph generated with the free software egypt by Andreas Gustafsson (<http://www.gson.org/egypt/egypt.html>).

Bibliography

- Abel, T. 2011, MNRAS, 413, 271
- Abel, T., Hahn, O., & Kaehler, R. 2012, MNRAS, 427, 61
- Abgrall, H., Roueff, E., & Viala, Y. 1982, A&AS, 50, 505
- Agertz, O., Kravtsov, A. V., Leitner, S. N., & Gnedin, N. Y. 2012, ArXiv e-prints
- Agertz, O., Moore, B., Stadel, J., et al. 2007, MNRAS, 380, 963
- Baldry, I. K., Balogh, M. L., Bower, R. G., et al. 2006, MNRAS, 373, 469
- Baldry, I. K., Glazebrook, K., Brinkmann, J., et al. 2004, ApJ, 600, 681
- Balsara, D. S. 1995, Journal of Computational Physics, 121, 357
- Barnes, J. & Hut, P. 1986, Nature, 324, 446
- Bate, M. R. & Burkert, A. 1997, MNRAS, 288, 1060
- Bell, A. R. 1978, MNRAS, 182, 147
- Bergin, E. A., Hartmann, L. W., Raymond, J. C., & Ballesteros-Paredes, J. 2004, ApJ, 612, 921
- Bigiel, F. & Blitz, L. 2012, ApJ, 756, 183
- Bigiel, F., Leroy, A., Walter, F., et al. 2008, AJ, 136, 2846
- Binney, J. & Spergel, D. 1982, ApJ, 252, 308
- Binney, J. & Tremaine, S. 2008, Galactic Dynamics: Second Edition (Princeton University Press)
- Blandford, R. D. & Ostriker, J. P. 1978, ApJ, 221, L29
- Bonnell, I. A., Dobbs, C. L., & Smith, R. J. 2013, MNRAS, 430, 1790
- Bosma, A. 1978, PhD thesis, PhD Thesis, Groningen Univ., (1978)

- Bournaud, F. & Combes, F. 2002, *A&A*, 392, 83
- Bournaud, F., Combes, F., & Semelin, B. 2005, *MNRAS*, 364, L18
- Bournaud, F., Elmegreen, B. G., Teyssier, R., Block, D. L., & Puerari, I. 2010, *MNRAS*, 409, 1088
- Brahic, A. 1977, *A&A*, 54, 895
- Buta, R. & Combes, F. 1996, *Fund. Cosmic Phys.*, 17, 95
- Buta, R. J., Sheth, K., Regan, M., et al. 2010, *ApJS*, 190, 147
- Christensen, C., Governato, F., Quinn, T., et al. 2012a, *ArXiv e-prints*
- Christensen, C., Quinn, T., Governato, F., et al. 2012b, *MNRAS*, 425, 3058
- Combes, F., Debbasch, F., Friedli, D., & Pfenniger, D. 1990, *A&A*, 233, 82
- Combes, F. & Gerin, M. 1985, *A&A*, 150, 327
- Coppola, C. M., Lodi, L., & Tennyson, J. 2011, *MNRAS*, 415, 487
- Couchman, H. M. P. 1991, *ApJ*, 368, L23
- Cox, D. P. 2005, *ARA&A*, 43, 337
- Dalgarno, A. & McCray, R. A. 1972, *ARA&A*, 10, 375
- Davé, R., Cen, R., Ostriker, J. P., et al. 2001, *ApJ*, 552, 473
- de Jong, R. S. 1996, *A&A*, 313, 45
- de Vaucouleurs, G. 1948, *Annales d'Astrophysique*, 11, 247
- de Vaucouleurs, G. 1974, in *IAU Symposium, Vol. 58, The Formation and Dynamics of Galaxies*, ed. J. R. Shakeshaft, 1–52
- de Vaucouleurs, G., de Vaucouleurs, A., Corwin, Jr., H. G., et al. 1991, *Third Reference Catalogue of Bright Galaxies. Volume I: Explanations and references. Volume II: Data for galaxies between 0^h and 12^h . Volume III: Data for galaxies between 12^h and 24^h .*
- Dehnen, W. 2002, *Journal of Computational Physics*, 179, 27
- Di Matteo, P., Combes, F., Melchior, A.-L., & Semelin, B. 2007, *A&A*, 468, 61
- Di Matteo, T., Springel, V., & Hernquist, L. 2005, *Nature*, 433, 604
- Dickman, R. L., Snell, R. L., & Schloerb, F. P. 1986, *ApJ*, 309, 326
- Dobbs, C. L. & Bonnell, I. A. 2008, *MNRAS*, 385, 1893

- Draine, B. T. 2011, *Physics of the Interstellar and Intergalactic Medium*
- Draine, B. T. & Bertoldi, F. 1996, *ApJ*, 468, 269
- Einstein, A. 1916, *Annalen der Physik*, 354, 769
- Emsellem, E., Cappellari, M., Krajnović, D., et al. 2007, *MNRAS*, 379, 401
- Eskridge, P. B., Frogel, J. A., Pogge, R. W., et al. 2000, *AJ*, 119, 536
- Fabbiano, G. 1989, *ARA&A*, 27, 87
- Faber, S. M. & Jackson, R. E. 1976, *ApJ*, 204, 668
- Famaey, B. & McGaugh, S. S. 2012, *Living Reviews in Relativity*, 15, 10
- Ferland, G. J., Korista, K. T., Verner, D. A., et al. 1998, *PASP*, 110, 761
- Fukugita, M., Hogan, C. J., & Peebles, P. J. E. 1998, *ApJ*, 503, 518
- Fukugita, M. & Peebles, P. J. E. 2004, *ApJ*, 616, 643
- Galli, D. & Palla, F. 1998, *A&A*, 335, 403
- Gerola, H. & Seiden, P. E. 1978, *ApJ*, 223, 129
- Gerritsen, J. P. E. 1997, PhD thesis, , Groningen University, the Netherlands, (1997)
- Gingold, R. A. & Monaghan, J. J. 1977, *MNRAS*, 181, 375
- Glover, S. C. O. & Abel, T. 2008, *MNRAS*, 388, 1627
- Gnat, O. & Sternberg, A. 2007, *ApJS*, 168, 213
- Gnedin, N. Y. 1995, *ApJS*, 97, 231
- Gnedin, N. Y., Tassis, K., & Kravtsov, A. V. 2009, *ApJ*, 697, 55
- Goldreich, P. & Lynden-Bell, D. 1965, *MNRAS*, 130, 125
- Gould, R. J. & Salpeter, E. E. 1963, *ApJ*, 138, 393
- Hernquist, L. 1993, *ApJ*, 404, 717
- Hernquist, L. & Katz, N. 1989, *ApJS*, 70, 419
- Hockney, R. W. & Eastwood, J. W. 1981, *Computer Simulation Using Particles*
- Hoekstra, H., van Albada, T. S., & Sancisi, R. 2001, *MNRAS*, 323, 453
- Hollenbach, D. & McKee, C. F. 1979, *ApJS*, 41, 555

- Hollenbach, D. & McKee, C. F. 1989, *ApJ*, 342, 306
- Hollenbach, D. & Salpeter, E. E. 1971, *ApJ*, 163, 155
- Hollenbach, D. J. & Tielens, A. G. G. M. 1999, *Reviews of Modern Physics*, 71, 173
- Holmberg, E. 1941, *ApJ*, 94, 385
- Hopkins, P. F. 2013, *MNRAS*, 428, 2840
- Hopkins, P. F., Quataert, E., & Murray, N. 2011, *MNRAS*, 417, 950
- Hubble, E. 1929, *Proceedings of the National Academy of Science*, 15, 168
- Hubble, E. P. 1926, *ApJ*, 64, 321
- Huber, K. & Herzberg, G. 1979, *Molecular spectra and molecular structure, Molecular Spectra and Molecular Structure No. vol. 4* (Van Nostrand)
- Iannuzzi, F. & Dolag, K. 2011, *MNRAS*, 417, 2846
- Jeans, J. H. 1902, *Royal Society of London Philosophical Transactions Series A*, 199, 1
- Jog, C. J. & Solomon, P. M. 1984, *ApJ*, 276, 114
- Jungwiert, B., Combes, F., & Palouš, J. 2001, *A&A*, 376, 85
- Katz, N. 1992, *ApJ*, 391, 502
- Katz, N., Weinberg, D. H., & Hernquist, L. 1996, *ApJS*, 105, 19
- Kauffmann, G., White, S. D. M., Heckman, T. M., et al. 2004, *MNRAS*, 353, 713
- Kennicutt, Jr., R. C. 1998, *ARA&A*, 36, 189
- Kereš, D., Vogelsberger, M., Sijacki, D., Springel, V., & Hernquist, L. 2012, *MNRAS*, 425, 2027
- Knebe, A., Green, A., & Binney, J. 2001, *MNRAS*, 325, 845
- Komatsu, E., Smith, K. M., Dunkley, J., et al. 2011, *ApJS*, 192, 18
- Kormendy, J. & Bender, R. 1996, *ApJ*, 464, L119
- Kormendy, J. & Kennicutt, Jr., R. C. 2004, *ARA&A*, 42, 603
- Kravtsov, A. V., Klypin, A. A., & Khokhlov, A. M. 1997, *ApJS*, 111, 73
- Kroupa, P. 2002, *Science*, 295, 82
- Krumholz, M. R., McKee, C. F., & Tumlinson, J. 2008, *ApJ*, 689, 865

- Krumholz, M. R., McKee, C. F., & Tumlinson, J. 2009a, *ApJ*, 693, 216
- Krumholz, M. R., McKee, C. F., & Tumlinson, J. 2009b, *ApJ*, 693, 216
- Lehner, N., Savage, B. D., Richter, P., et al. 2007, *ApJ*, 658, 680
- Levinson, F. H. & Roberts, Jr., W. W. 1981, *ApJ*, 245, 465
- Lin, C. C. & Shu, F. H. 1964, *ApJ*, 140, 646
- Lindblad, B. 1963, *Stockholms Observatoriums Annaler*, 22, 5
- Lipovka, A., Núñez-López, R., & Avila-Reese, V. 2005, *MNRAS*, 361, 850
- Lucy, L. B. 1977, *AJ*, 82, 1013
- Lynden-Bell, D. & Kalnajs, A. J. 1972, *MNRAS*, 157, 1
- Maio, U., Dolag, K., Ciardi, B., & Tornatore, L. 2007, *MNRAS*, 379, 963
- Makino, J. & Funato, Y. 1993, *PASJ*, 45, 279
- McGaugh, S. S. 2005, *ApJ*, 632, 859
- McGaugh, S. S. 2011, *Physical Review Letters*, 106, 121303
- McGaugh, S. S. & de Blok, W. J. G. 1997, *ApJ*, 481, 689
- McGaugh, S. S., Schombert, J. M., Bothun, G. D., & de Blok, W. J. G. 2000, *ApJ*, 533, L99
- McKee, C. F. & Krumholz, M. R. 2010, *ApJ*, 709, 308
- McKee, C. F. & Ostriker, E. C. 2007, *ARA&A*, 45, 565
- McKee, C. F. & Ostriker, J. P. 1977, *ApJ*, 218, 148
- Mihos, J. C. & Hernquist, L. 1994, *ApJ*, 437, 611
- Milgrom, M. 1983a, *ApJ*, 270, 371
- Milgrom, M. 1983b, *ApJ*, 270, 384
- Milgrom, M. 1983c, *ApJ*, 270, 365
- Miyamoto, M. & Nagai, R. 1975, *PASJ*, 27, 533
- Mo, H., van den Bosch, F. C., & White, S. 2010, *Galaxy Formation and Evolution*
- Monaghan, J. J. 1992, *ARA&A*, 30, 543
- Monaghan, J. J. 1997, *Journal of Computational Physics*, 136, 298

- Monaghan, J. J. & Lattanzio, J. C. 1985, *A&A*, 149, 135
- Navarro, J. F., Frenk, C. S., & White, S. D. M. 1997, *ApJ*, 490, 493
- Navarro, J. F. & White, S. D. M. 1993, *MNRAS*, 265, 271
- Navarro, J. F. & White, S. D. M. 1994, *MNRAS*, 267, 401
- O'Shea, B. W., Bryan, G., Bordner, J., et al. 2004, *ArXiv Astrophysics e-prints*
- Parmar, P. S., Lacy, J. H., & Achtermann, J. M. 1991, *ApJ*, 372, L25
- Peacock, J. A., Cole, S., Norberg, P., et al. 2001, *Nature*, 410, 169
- Pen, U.-L. 1998, *ApJS*, 115, 19
- Perlmutter, S., Aldering, G., della Valle, M., et al. 1998, *Nature*, 391, 51
- Pety, J., Schinnerer, E., Leroy, A. K., et al. 2013, *ArXiv e-prints*
- Pfenniger, D. & Combes, F. 1994, *A&A*, 285, 94
- Pfenniger, D., Combes, F., & Martinet, L. 1994, *A&A*, 285, 79
- Planck Collaboration, Ade, P. A. R., Aghanim, N., et al. 2013, *ArXiv e-prints*
- Power, C., Navarro, J. F., Jenkins, A., et al. 2003, *MNRAS*, 338, 14
- Price, D. J. 2007, *PASA*, 24, 159
- Price, D. J. 2008, *Journal of Computational Physics*, 227, 10040
- Rachford, B. L., Snow, T. P., Tumlinson, J., et al. 2002, *ApJ*, 577, 221
- Read, J. I., Hayfield, T., & Agertz, O. 2010, *MNRAS*, 405, 1513
- Regan, M. W., Thornley, M. D., Helfer, T. T., et al. 2001, *ApJ*, 561, 218
- Revaz, Y., Jablonka, P., Sawala, T., et al. 2009a, *A&A*, 501, 189
- Revaz, Y., Pfenniger, D., Combes, F., & Bournaud, F. 2009b, *A&A*, 501, 171
- Riess, A. G., Filippenko, A. V., Challis, P., et al. 1998, *AJ*, 116, 1009
- Ritchie, B. W. & Thomas, P. A. 2001, *MNRAS*, 323, 743
- Roberts, M. S. & Haynes, M. P. 1994, *ARA&A*, 32, 115
- Rubin, V. C., Ford, W. K. J., & Thonnard, N. 1980, *ApJ*, 238, 471
- Rubin, V. C., Thonnard, N., & Ford, Jr., W. K. 1978, *ApJ*, 225, L107

- Salpeter, E. E. 1955, *ApJ*, 121, 161
- Santoro, F. & Shull, J. M. 2006, *ApJ*, 643, 26
- Scalo, J. M. 1986, *Fund. Cosmic Phys.*, 11, 1
- Schaye, J. 2004, *ApJ*, 609, 667
- Schaye, J. & Dalla Vecchia, C. 2008, *MNRAS*, 383, 1210
- Schmidt, M. 1959, *ApJ*, 129, 243
- Schure, K. M., Kosenko, D., Kaastra, J. S., Keppens, R., & Vink, J. 2009, *A&A*, 508, 751
- Sellwood, J. A. 2013, ArXiv e-prints
- Sellwood, J. A. & Sparke, L. S. 1988, *MNRAS*, 231, 25P
- Semelin, B. & Combes, F. 2002, *A&A*, 388, 826
- Semelin, B. & Combes, F. 2005, *A&A*, 441, 55
- Sersic, J. L. 1968, *Atlas de galaxias australes*
- Shull, J. M. & Beckwith, S. 1982, *ARA&A*, 20, 163
- Solomon, P. M., Downes, D., Radford, S. J. E., & Barrett, J. W. 1997, *ApJ*, 478, 144
- Spitzer, Jr., L., Cochran, W. D., & Hirshfeld, A. 1974, *ApJS*, 28, 373
- Springel, V. 2005, *MNRAS*, 364, 1105
- Springel, V. 2009, <http://video.ias.edu/PiTP2009>
- Springel, V. 2010a, *MNRAS*, 401, 791
- Springel, V. 2010b, *ARA&A*, 48, 391
- Springel, V. & Hernquist, L. 2002, *MNRAS*, 333, 649
- Springel, V. & Hernquist, L. 2003, *MNRAS*, 339, 289
- Springel, V., Wang, J., Vogelsberger, M., et al. 2008, *MNRAS*, 391, 1685
- Springel, V., White, S. D. M., Jenkins, A., et al. 2005, *Nature*, 435, 629
- Steinmetz, M. 1996, *MNRAS*, 278, 1005
- Stinson, G., Seth, A., Katz, N., et al. 2006, *MNRAS*, 373, 1074
- Sutherland, R. S. & Dopita, M. A. 1993, *ApJS*, 88, 253

- Teyssier, R. 2002, *A&A*, 385, 337
- Teyssier, R., Chapon, D., & Bournaud, F. 2010, *ApJ*, 720, L149
- Thacker, R. J. & Couchman, H. M. P. 2000, *ApJ*, 545, 728
- Toomre, A. 1964, *ApJ*, 139, 1217
- Toomre, A. 1981, in *Structure and Evolution of Normal Galaxies*, ed. S. M. Fall & D. Lynden-Bell, 111–136
- Toomre, A. & Toomre, J. 1972, *ApJ*, 178, 623
- Tully, R. B. & Fisher, J. R. 1977, *A&A*, 54, 661
- Ungerechts, H., Umbanhowar, P., & Thaddeus, P. 2000, *ApJ*, 537, 221
- Wadsley, J. W., Stadel, J., & Quinn, T. 2004, *New A*, 9, 137
- Wadsley, J. W., Veeravalli, G., & Couchman, H. M. P. 2008, *MNRAS*, 387, 427
- Warren, M. S. & Salmon, J. K. 1995, *Computer Physics Communications*, 87, 266
- Wiersma, R. P. C., Schaye, J., Theuns, T., Dalla Vecchia, C., & Tornatore, L. 2009, *MNRAS*, 399, 574
- Wolcott-Green, J., Haiman, Z., & Bryan, G. L. 2011, *MNRAS*, 418, 838
- Yoshikawa, K., Yoshida, N., & Umemura, M. 2013, *ApJ*, 762, 116
- Young, J. S. & Scoville, N. Z. 1991, *ARA&A*, 29, 581